Fakultät für Chemie

Lehrstuhl für Theoretische Chemie

Theory and computational studies of the photoinduced dynamics and time-resolved spectroscopy of molecular aggregates

Leah Sharp

Vollständiger Abdruck der von der Fakultät für Chemie
der Technischen Universität München zur Erlangung des akademischen Grades eines
Doktors der Naturwissenschaften
genehmigten Dissertation.

Vorsitzender: Univ.-Prof. Dr. Tom Nilges

Prüfer der Dissertation:

1. Univ.-Prof. Dr. Wolfgang Domcke
2. Univ.-Prof. Dr. Martin Zacharias

Die Dissertation wurde am 26. Juni 2013 bei der Technischen Universität München eingereicht und durch die Fakultät für Chemie am 15. Juli 2013 angenommen.

Contents

Acknowledgements

A work of this nature is never produced completely independently. Rather, it is the collective effort of many individuals, without whose support, encouragement, and insights this creation would never have materialized. I am especially grateful to Prof. Wolfgang Domcke for first accepting me into his research group, and then for his continuous support throughout this endeavor. Conversations with Dassia Egorova have been invaluable, as has her guidance. Maxim Gelin, was a pleasure to work and to travel with, exploring new ideas and new cultures. I am greatful to everyone in the Domcke Group, all of whom assisted in myriad ways, both large and small: Christoph, Sergey, Ian, Padma, Marianne, Michael, Andreas, Daniel, Andriy, Deniz, Sai, Raffaele, Bartosz, Jingrui, Venky, Vassil, Dorit, Oscar, Clemens, Claudia, Mehdi, Rainer, Axel, Zhenggang, Kiran, Mishra, Olivier, and of course Ruth, who made everything happen.

Even when far away, there are people whose friendship can withstand time and space. I am thankful for Stacey, Alli, Kara, and Rebecca, whose phone calls and visits kept me grounded. I would especially like to thank my parents, for not freaking out when I decided to move across the continent and an ocean with my boyfriend; their love and encouragement sustained me during this adventure. Specifically to my mother, who was not only an inspiration, but her mandate that I finish my studies before starting a family has been ingrained in my psyche, I offer my appreciation.

Nearby I found myself surrounded by wonderful people, whose friendships return with me to the States. Thank you, Toni, for being the organizer, from Alpine trips to Biergarten picnics, it was always good times. Brent and Basil, thank you for the respite, any day, any time, any place, as long as there was beer involved. Yara and Caro, thank you for teaching me Boarisch – and making it fun in the process. Most importantly, I would like to thank Ian, without whose constant support and encouragement none of this would have happened.

I would like to acknowledge the support of the International Max Planck Research School for Advanced Photon Science, with Tobias and Matthias as our fearless leaders. While my colleagues are numerous, I would be remiss if I did not attempt to acknowledge a few of them here: Antonia, Sergey (and Arsenia), Peter, Andreas, Matthias, Alex, Daniel, Patrick, Wolfram, Michael, Shao-Wei, Sandro, Christoph, Raphael, Johannes, and especially, Monika.

Chapter 1

Introduction

The molecular dimer is a basic model system for the theoretical description of myriad systems. Applications of the molecular dimer range from quantum information [1–3], to Bose-Einstein condensates [4–6], and to molecular aggregates [7–9]. It is a simple, albeit prolific, system for the study of complicated electronic-vibrational interactions [8, 10–13]. Early studies of dimers of chromophores and molecular aggregates include work by Förster [14] and Dexter [15] based on an incoherent rate equation approach. One fascinating role of molecular aggregates is in photosynthetic light-harvesting complexes. Photosynthesis, with a quantum yield exceeding 95%, is an extremely efficient mechanism for the absorption and transfer of solar energy and its conversion to chemical energy [16]. Complexes of molecular aggregates are used to streamline the transfer of energy from light-harvesting antenna systems, which efficiently capture sunlight, to the reaction center, in which energy is converted for later use in biochemical processes [17].

A significant effort is currently underway to fully understand the quantum mechanical mechanisms underlying the efficient transfer of energy during pho-

tosynthesis through pigment-protein complexes. The pigments capture sunlight which is then efficiently transferred to the reaction center. Variations in the protein scaffold surrounding each pigment effectively vary the absorption maximum of each molecule, thereby increasing efficiency, while the protein itself acts as an energy sink. Studies have shown that the pigments form a system of electronically coupled excitons [18], in which the excitation simultaneously extends over several bacteriochlorophyll (BChl) molecules. Thus, the excitation probes several pathways concurrently and selects the most efficient path to the lowest energy state, which may account for their remarkable efficiency.

The most extensively studied photosynthetic systems are those for which the atomic structure has been determined by X-ray crystallography: the peripheral light-harvesting complexes of photosynthetic purple bacteria [19, 20] and green plants [21], as well as the Fenna-Matthews-Olson (FMO) pigment-protein complex of green sulphur bacteria [22].

First insight into the energy transfer dynamics of the FMO complex was attained from nonlinear ultrafast spectroscopy. Various nonlinear techniques such as hole burning [23–25], one- and two-color pump probe [26–32], and accumulated photon-echo (PE) spectroscopy [33] have revealed a number of time scales ranging from 70-100 fs to about 20 ps.

Recently, two-dimensional (2D) electronic PE spectra of the *Chlorobium* (*Cb.*) *tepidum* FMO complex were recorded [34, 35]. In contrast to the previous findings and assumptions, these new experimental results indicate strongly coherent energy-transfer dynamics [35]. The coherent oscillations in the spectroscopic signals were shown to survive on a relatively long time scale of about 700 fs. They were interpreted to be a manifestation of electronic coherences which arise due to the coupling between the excited states of different pigments [34, 35].

The first theoretical models of the FMO complex aimed to reproduce the linear absorption spectrum and the kinetics of the pump-probe spectra [31, 36, 37]. In these models, the seven pigments of one FMO monomer were treated as seven two-level systems with electronically coupled excited states. The effect of vibrations and the protein environment was taken into account by considering the coupling of the electronic degrees of freedom to a phonon bath, which was introduced in a simplified manner: Only electronic population relaxation was modeled and the corresponding relaxation rates were determined by fitting the simulations to the experimental results.

This simple exciton model [37] was also employed for the simulation of 2D spectra [38]. The relaxation rates were computed using a modified Förster/Redfied theory and a reproduction of 2D profiles for finite population times was achieved. However, signatures of coherent energy transfer in 2D signals were beyond the scope of these simulations, since coherences between the exciton states were not taken into account. Furthermore, the scheme employed for the simulation of spectra contained a number of crude approximations and, in particular, did not allow for the evaluation of the 2D signal at zero population time.

In contrast to pump-probe experiments, which can be fitted by considering the time evolution of the diagonal elements of the density matrix (populations) only, PE spectroscopy is a coherent technique and knowledge of the time evolution of the off-diagonal elements of the density matrix (coherences) is required for an accurate description of this signal. The first steps toward the understanding of coherent effects in the 2D spectroscopy of the FMO complex were taken by considering 2D spectra of dimer and trimer systems [39, 40]. The simulations showed that electronic coherences can indeed be visualized by the 2D technique as oscillatory beatings of cross peaks in the intensity profiles as a function of the population time. New pulse-sequence schemes have been recently proposed

for the investigation of the coherent dynamics of the FMO complex [41, 42].

The present work employs the equation-of-motion phase-matching-approach (EOM-PMA) [43–45], for the efficient calculation of 2D electronic PE signals for a Frenkel exciton model. The numerical effort for the calculation of the PE polarization utilizing the EOM-PMA scales approximately as three times the number of elements in the density matrix times the square of the number of time steps [44]. With a given equation of motion of the material system under study, the EOM-PMA does not invoke additional approximations apart from the weak-field limit. This approach has been successfully used to compare simulated and experimental signals [46]. The computational efficiency of the EOM-PMA, allows for study of more complicated systems, including, for example, explicit intramonomer or intermonomer electron-vibrational couplings or a nonsecular multilevel Redfield description of vibrational energy and phase relaxation. In fact, the EOM-PMA enables the simulation of N-wave-mixing signals for any material system for which the equation of motion of the reduced density matrix can be numerically solved on the time scale of interest.

The model Hamiltonian of the FMO complex as specified in Refs. [37, 38] and an equation of motion that accounts for the time evolution of populations as well as coherences of the exciton density matrix (within the secular approximation) are employed. The electronic population relaxation parameters are taken from Ref. [38], while the pure dephasing rates are considered to be adjustable parameters. The comparison of the computed signals with the experimental result thus provides a stringent test of the chosen model of the material dynamics. Additionally, a rigorous exploration of various relaxation and dephasing effects is considered.

Recently, Ishizaki and Fleming employed a dimer model to point out the inadequacy of the standard Redfield equation to treat quantum coherence and

long-lived oscillations of 2D peak intensities [47]. In addition, excitons in the FMO complex of *Ch. tepidum* tend to be comprised of strongly coupled pairs of BChls [38]. As such, the dimer model lends itself for probing more complicated vibronic effects in system dynamics in molecular aggregates. This issue is addressed here as well for the Frenkel exciton model of one pair of BChl molecules within the FMO complex. In the present work, 2D PE spectra of an ideal dimer system under influence of the Redfield model of relaxation are simulated, using the EOM-PMA. Although the dimer model in the secular approximation was used to point out the inadequacy of the standard Redfield equation to treat quantum coherence and long-lived oscillations of 2D peak intensities, the present study adopts a nonsecular approach, while including vibrational modes explicitly. The inclusion of vibrational modes in the system Hamiltonian allows for a deeper understanding of the nature of quantum coherences, as well as the determining factors of their lifetimes. The dimer is modeled after BChls three and four of the FMO complex of *Ch. tepidum*, as designated in Ref. [22]. These particular molecules are chosen as they are the primary consituents of excitons one and three, [38] for which coherence 1–3 was seen to survive on a relatively long timescale, and thus its dynamics are particularly interesting, even at short timescales. Excitons one and three are also energetically well-separated from the other excitons, thereby justifying the omission of the other excitons in this model study.

The theory used to describe the system dynamics is well known, and an outline is provided in Chapter 2. In addition, a description of the two model systems under study, the full FMO complex and a dimer of BChls, is also provided. Details about how various dissipation mechanisms are modeled, as well as the EOM-PMA, are also outlined in Chapter 2.

In Chapter 3, accurate simulations of 2D PE signals for an existing simple

Redfield equation model [37, 38] are discussed. Various dephasing mechanisms on coherence lifetimes are systematically studied for this rather versatile model system. This demonstrates the successful application of the EOM-PMA for the efficient simulation of four-wave-mixing spectra for reasonably complex material systems.

With confirmation of the applicability of the EOM-PMA to molecular aggregates, we study details of dimer dynamics in Chapters 4 and 5. Specifically, relaxation and dephasing effects of a dimer modeled after BChls 4 and 5, so named in Ref. [22], in the FMO complex are studied. First, in Chapter 4, both site and eigenstate dynamics are studied after stimulation by a single laser pulse with the system coupled to an uncorrelated bath. Following this, analysis of the effect of a dimer experiencing (un-)(anti-)correlated baths is presented. Subsequently, in Chapter 5, 2DPE signals are calculated for the dimer system, using the EOM-PMA, and diagonal and crosspeak behavior is analyzed in the 2D spectral profiles.

Chapter 2

Theory

2.1 Quantum Master Equation

2.1.1 Liouville equation

The density matrix formalism is used in the following to describe the molecular complexes outlined in the previous section during and after excitation by an electric field, a complete and detailed description of which can be found in Refs. [48] and [49]. The total density matrix, also called the statistical operator, represents all degrees of freedom in the total system and is defined as

$$W = \sum_n w_n |\psi_n\rangle\langle\psi_n|, \tag{2.1}$$

which is a sum of projection operators on the states $|\psi_n\rangle$ weighted by the probabilites of finding the system in the aforementioned state, w_n. The diagonal elements of the density matrix, $\langle\phi_m|W|\phi_m\rangle$, give the total probabilities of finding a particle in the corresponding basis state, $|\phi_m\rangle$; and thus $W_{mm} \geq 0$. The density matrix is normalized, $\mathrm{tr}\{W\} = 1$, and is hermitian. The physical sig-

nificance of the time evolution of the off-diagonal elements is associated with quantum coherences. In this notation, the expectation value of any observable, A, can be found using $\langle A\rangle = \mathrm{tr}\{WA\}$.

The time-dependent Schrödinger equation can be used to derive the time evolution of the wave function ($\hbar = 1$):

$$i\frac{\partial|\psi(t)\rangle}{\partial t} = H(t)|\psi(t)\rangle, \tag{2.2}$$

and likewise for the adjoint. Eq. (2.2) can be generalized by defining the time evolution operator, $U(t) = \exp(-iHt)$, which transforms an initial state $|\psi(0)\rangle$ to a state at a later time, $|\psi(t)\rangle$:

$$|\psi(t)\rangle = U(t)|\psi(0)\rangle, \tag{2.3}$$

such that $U(0) = 1$. Using Eq. (2.3) and its hermitian conjugate in the Schrödinger equation, the equation of motion for the time evolution operator can be written as

$$i\frac{\partial U(t)}{\partial t} = H(t)U(t), \tag{2.4}$$

since the Schrödinger equation must hold for any wavefunction, $|\psi(t)\rangle$. The time evolution of the density matrix can thus be written using Eq. (2.3)

$$W(t) = U(t)W(0)U^{\dagger}(t). \tag{2.5}$$

Differentiating and using Eq. (2.4), its adjoint, and the Schrödinger equation, the equation of motion for the density operator can be derived

$$\frac{\partial W(t)}{\partial t} = -i[H(t), W(t)], \tag{2.6}$$

which is called the Liouville equation.

2.1.2 The interaction picture

When the Hamiltonian for a system can be described according to Eq. (2.34), and if the system-bath interaction is a small perturbation, then Eq. (2.4) can be solved using time-dependent perturbation theory. By defining the wave function in the interaction picture, $|\psi(t)_I\rangle$, as

$$|\psi(t)\rangle = e^{-iH_0t}|\psi(t)_I\rangle, \tag{2.7}$$

and inserting it into Eq. (2.2), we find that

$$\frac{\partial|\psi(t)_I\rangle}{\partial t} = H_{SB}(t)_I|\psi(t)_I\rangle, \tag{2.8}$$

where the perturbation in the interaction picture is defined as

$$H_{SB}(t)_I = e^{iH_0t}H_{SB}e^{-iH_0t}. \tag{2.9}$$

In other words, the time dependence of the wavefunction in the interaction picture is created only by the external potential term $H_{SB}(t)_I$. Since H_{SB} is a small perturbation, $|\psi(t)_I\rangle$ varies slowly with time. Note that all operators in the interaction picture can be defined using

$$A(t)_I = e^{iH_0t}A(t)e^{-iH_0t}. \tag{2.10}$$

Let $U(t)_0 = \exp(-iH_0t)$; then, since $U(0)_0 = 1$, the Schrödinger and inter-

action pictures are equivalent for $t = 0$. Using Eq. (2.3),

$$\begin{aligned} |\psi(t)_I\rangle &= e^{iH_0 t}U(t)|\psi(0)\rangle, \\ &= U(t)_I|\psi(0)_I\rangle, \end{aligned} \tag{2.11}$$

where we have defined

$$U(t) = e^{-iH_0 t}U(t)_I. \tag{2.12}$$

Thus, $U(t)_I$ determines the time evolution of states in the interaction picture.

The density matrix can be written in the interaction picture, as well:

$$\begin{aligned} W(t)_I &= \sum_n w_n|\psi(t)_{n,I}\rangle\langle\psi(t)_{n,I}| \\ &= e^{iH_0 t}W(t)e^{-iH_0 t}. \end{aligned} \tag{2.13}$$

Using Eqs. (2.5) and (2.12), this becomes

$$W(t)_I = U(t)_I W(0)U(t)_I^\dagger, \tag{2.14}$$

since $W(0)_I = W(0)$. The Liouville equation is written in the interaction picture by inserting Eq. (2.13) into Eq. (2.6). After some manipulation, it follows that the Liouville equation in the interaction picture is:

$$\frac{\partial W(t)_I}{\partial t} = -i[H_{SB}(t)_I, W(t)_I]. \tag{2.15}$$

2.1.3 Reduced density matrix

While the complex under study has been split into a relevant part, including a few degrees of freedom and a bath, the full density matrix, too, can be written as a product of the relevant system and the bath degrees of freedom:

$W(t) = \rho(t)R(t)$, where $\rho(t)$, called the reduced density matrix, describes only the relevant system of interest, and $R(t)$ describes the reservoir. The reduced density matrix can be defined by tracing out the bath degrees of freedom from the full density matrix:

$$\rho(t) = \mathrm{tr}_B\{W(t)\}, \tag{2.16}$$

likewise, in the interaction picture

$$\rho(t)_I = \mathrm{tr}_B\{W(t)_I\}. \tag{2.17}$$

In order to derive an equation of motion for the reduced density matrix, the Liouville equation in the interaction picture, Eq. (2.15) is formally integrated:

$$W(t)_I = W(0)_I - i\int_0^t d\tau[H_{SB}(\tau)_I, W(\tau)_I]. \tag{2.18}$$

This is the first-order approximation to the Liouville equation in the interaction picture. Inserting this back into Eq. (2.15), we find the second-order approximation to the Liouville equation in the interaction picture.

$$\frac{\partial W(t)_I}{\partial t} = -i[H_{SB}(t)_I, W(0)_I] - \int_0^t [H_{SB}(t)_I, [H_{SB}(\tau)_I, W(t)_I]]d\tau. \tag{2.19}$$

Assuming the interaction is turned on at a time $t = 0$, and by taking the trace over the reservoir degrees of freedom, the equation of motion for the reduced density operator in the interaction picture can be written

$$\begin{aligned}\dot{\rho}(t)_I &= -i\mathrm{tr}_B\{[H_{SB}(t)_I, \rho(0)_I R(0)]\} \\ &\quad - \int_0^t d\tau \mathrm{tr}_B\{[H_{SB}(t)_I, [H_{SB}(\tau)_I, \rho(\tau)_I R(\tau)]]\},\end{aligned} \tag{2.20}$$

since $W(0) = \rho(0)R(0) = W(0)_I$ at $t = 0$.

Consider now the basic condition of irreversibility, which states that the reservoir has so many degrees of freedom that the effects of an interaction with the system will quickly dissipate away and will not again affect the system to any measurable extent. In other words, $R(t) = R(0) \equiv R_0$ and so the density matrix can be rewritten as $W(t)_I = \rho(t)_I R_0$ for all time. Then Eq. (2.20) becomes

$$\begin{aligned} \dot{\rho}(t)_I &= -i\mathrm{tr}_B\{[H_{SB}(t)_I, \rho(0)_I R_0]\} \\ &\quad - \int_0^t d\tau \mathrm{tr}_B\{[H_{SB}(t)_I, [H_{SB}(\tau)_I, \rho(\tau)_I R_0]]\}, \end{aligned} \tag{2.21}$$

to second order in the system-bath interaction. The equation of motion for a reduced density matrix is known as the generalized master equation.

The Markov approximation states that the system has no memory of its past. In other words, $\rho(t)_I$ depends only on its present value, and not on its history. In this case, $\rho(\tau)_I$ in the integral of Eq. (2.21) can be replaced with $\rho(t)_I$ and thus

$$\begin{aligned} \dot{\rho}(t)_I &= -i\mathrm{tr}_B\{[H_{SB}(t)_I, \rho(0) R_0]\} \\ &\quad - \int_0^t d\tau \mathrm{tr}_B\{[H_{SB}(t)_I, [H_{SB}(\tau)_I, \rho(t)_I R_0]]\} \end{aligned} \tag{2.22}$$

is the equation of motion for the reduced density operator in the interaction picture to second order in the system-bath interaction.

If the system-bath interaction takes the form $\sum_i Q_i F_i$, where the coordinates, Q_i, are system operators and the F_i operate only on the bath, and the index counts contributions from different microscopic descriptions of the system-

bath coupling, then $H_{SB}(t)_I$ can be written

$$\begin{aligned} H_{SB}(t)_I &= e^{i(H_S+H_B)t} H_{SB} e^{-i(H_S+H_B)t} \\ &= \sum_i e^{iH_S t} Q_i e^{-iH_S t} e^{iH_B t} F_i e^{-iH_B t} \\ &= \sum_i Q_i(t) F_i(t), \end{aligned} \tag{2.23}$$

since F_i and Q_i commute. Inserting this into Eq. (2.22), and utilizing the cyclic property of the trace, we find that

$$\begin{aligned} \dot{\rho}(t)_I &= -i \sum_i ([Q_i(t), \rho(0)_I]) \mathrm{tr}_B\{F_i(t) R_0\} \\ &\quad - \int_0^t d\tau \Big([Q_i(t), Q_j(\tau)\rho(t)_I] \mathrm{tr}_B\{F_i(t) F_j(\tau) R_0\} \\ &\quad - [Q_i(t), \rho(t)_I Q_j(\tau)] \mathrm{tr}_B\{F_j(\tau) F_i(t) R_0\} \Big). \end{aligned} \tag{2.24}$$

Consider first the expectation value

$$\begin{aligned} \langle F_i(t) \rangle &= \mathrm{tr}_B\{F_i(t) R_0\} \\ &= \sum_N \langle N | F_i(t) | N \rangle \langle N | R_0 | N \rangle, \end{aligned} \tag{2.25}$$

which is expanded in bath eigenstates, $|N\rangle$, for convenience: In this basis, R_0 is diagonal. In other words, thermal fluctuations occur symmetrically around $F = 0$, and this term vanishes.

Consider now the time correlation functions

$$\langle F_i(t) F_j(\tau) \rangle = \mathrm{tr}_B\{F_i(t) F_j(\tau) R_0\}, \tag{2.26}$$

which are the expectation values of the product of physical quantities measured at different times, or the correlation which exists between interactions occurring

at times t and τ. Since the reservoir is large, it quickly dissipates the effects of an interaction, so that it "forgets" its interaction with the system. Therefore, the time correlation functions are only nonzero when $t-\tau \lesssim \tau_c$, where τ_c is some correlation time specific to a given reservoir. In other words, interactions at t and τ become uncorrelated ($\langle F_i(t)F_j(\tau)\rangle \to 0$) when $t-\tau \gg \tau_c$ and when $t=\tau$, the time correlation functions have reached a maximum value. It is also worth noting that the time correlation functions are stationary: They depend only on the time between the two interactions. Thus $\langle F_i(t)F_j(\tau)\rangle = \langle F_i(t-\tau)F_j\rangle \equiv C_{ij}(t-\tau)$.

Applying this to the Liouville equation, the integral over τ is only nonzero during the time interval $t-\tau \lesssim \tau_c$, and so Eq. (2.24) becomes

$$\begin{aligned}\dot{\rho}(t)_I &= -\sum_{ij}\int_0^t d\tau\Big([Q_i(t),Q_j(\tau)\rho(t)_I]\langle C_{ij}(t-\tau)\rangle \\ &\quad -[Q_i(t),\rho(t)_I Q_j(\tau)]\langle C^*_{ij}(t-\tau)\rangle\Big).\end{aligned} \tag{2.27}$$

Choosing $t' = t-\tau$, $dt' = -d\tau$ and $\int_0^t d\tau = \int_0^t dt'$; then the upper limit of integration can be taken to infinity with little error, since the correlation functions are effectively zero for $t' \gg \tau_c$. Then,

$$\begin{aligned}\dot{\rho}(t)_I &= -\sum_{ij}\int_0^\infty dt'\Big([Q_i(t),Q_j(t-t')\rho(t)_I]\langle C_{ij}(t')\rangle \\ &\quad -[Q_i(t),\rho(t)_I Q_j(t-t')]\langle C^*_{ij}(t')\rangle\Big).\end{aligned} \tag{2.28}$$

Writing the eigenstates of H_S as $|m\rangle$, and since $Q_i(t) = \exp(iH_S t)Q_i\exp(-iH_S t)$ from Eq. (2.23), the notation

$$\langle m|Q_i(t)|n\rangle = e^{i\omega_{mn}t}\langle m|Q_i|n\rangle \tag{2.29}$$

can be used, where $\omega_{mn} = E_m - E_n$, the difference in eigenenergies.

The Redfield operator, $\Re$, which describes the relaxation of the system, is introduced to simplify the notation in Eq. (2.28):

$$\dot{\rho}(t) = -i[H(t), \rho(t)] + \Re[\rho(t)], \tag{2.30}$$

where

$$\Re[\rho(t)] = \sum_{\kappa\lambda} R_{\mu\nu\kappa\lambda}\rho_{\kappa\lambda}(t), \tag{2.31}$$

and

$$R_{\mu\nu\kappa\lambda} = \Gamma^{+}_{\lambda\nu\mu\kappa} + \Gamma^{-}_{\lambda\nu\mu\kappa} - \delta_{\nu\lambda}\sum_{\alpha}\Gamma^{+}_{\mu\alpha\alpha\kappa} - \delta_{\mu\kappa}\sum_{\alpha}\Gamma^{-}_{\lambda\alpha\alpha\nu}. \tag{2.32}$$

The following notation has been introduced:

$$\begin{aligned}
\Gamma^{+}_{\lambda\nu\mu\kappa} &= \sum_{ij}\langle\lambda|Q_i|\nu\rangle\langle\mu|Q_j|\kappa\rangle\int_0^t d\tau C_{ij}(-\tau)e^{-i\omega_{\mu\kappa}\tau} \\
\Gamma^{-}_{\lambda\nu\mu\kappa} &= \sum_{ij}\langle\lambda|Q_i|\nu\rangle\langle\mu|Q_j|\kappa\rangle\int_0^t d\tau C_{ij}(\tau)e^{-i\omega_{\lambda\nu}\tau},
\end{aligned} \tag{2.33}$$

and Eq. (2.29) was used. Eq. (2.30) is called the quantum (or Pauli) master equation.

2.2 System Hamiltonians

In the case of laser-matter interaction, when the laser influences only a few relevant degrees of freedom of the complex under study, the description of the total system can be split into the relevant part, that which interacts with the laser field, and a dissipative reservoir, e.g. a heat bath. In this case, the Hamiltonian

describing the full complex, H, is

$$H = H_0 + H_{SB}, \tag{2.34}$$

with $H_0 = H_S + H_B$; H_S describes the system of interest, H_B is the Hamiltonian of the reservoir, and H_{SB} is the interaction between the two.

Two separate complexes will be presented here, both pertaining to a system of pigment-protein complexes found in photosynthetic systems of green sulphur bacteria. The full Fenna-Matthews-Olson (FMO) complex, which is in essence a wire connecting the light harvesting complex to the reaction center, will first be studied. The seven pigments make up the system, with the protein scaffold and vibrational modes comprising the bath. Subsequently, a dimer of bacteriochlorophyll$a$ (BChl) molecules will be studied to probe the role of vibrational levels on energy transfer dynamics in photosynthetic systems. Following the method outlined in Ref. [8], each monomer of the dimer complex can be described by two harmonic oscillator potentials with displaced excited potentials along a nuclear coordinate.

2.2.1 FMO Subunit

The FMO pigment-protein complex forms a trimer of identical, weakly interacting subunits. Each monomer contains seven BChl molecules, which serve to both collect energy and transfer it to the reaction center. The pigments are surrounded by a protein structure that holds the pigments in what are presumably their ideal positions, in order to maximize efficiency, ensure directionality of energy transfer toward the reaction center, and provide an energy sink [17].

The present study is based on a model of the FMO complex which has been elaborated over recent years by the analysis of experimental signals such as linear absorption, linear and circular dichroism [50], pump-probe [26–32],

and 2D photon echo (PE) [34, 38]. In this model, the interaction between the subunits is neglected and only a single monomer is considered (a comparative study of the monomer and trimer models justifies this approximation [51]). Each of the seven BChl molecules within the subunit is represented by an electronic two-level system. The excited states of the molecules are assumed to be coupled to each other and thus form a system of excitons. The vibrational degrees of freedom of the BChl pigment molecules and the protein environment are taken into account as a thermal bath. In the Hamiltonian given in Eq. (2.34), H_S is the electronic Hamiltonian of the seven BChl pigment molecules, H_B describes the protein scaffold, and H_{SB} determines the pigment-protein interaction. The system Hamiltonian can be further partioned as follows:

$$H_S = H_g + H_e, \tag{2.35}$$

where H_g and H_e describe the electronic ground states and the excited states of the pigment molecules, respectively. The ground states are assumed to be uncoupled and possess the same ground-state energy which is set to zero throughout: $H_g = |g\rangle\langle g|$. In the site representation (local basis), H_e reads

$$H_e = \sum_{\alpha=1}^{7} |\alpha\rangle \varepsilon_\alpha \langle\alpha| + \sum_{\alpha\neq\beta} \left(|\alpha\rangle J_{\alpha\beta} \langle\beta| + |\beta\rangle J_{\beta\alpha} \langle\alpha| \right), \tag{2.36}$$

where $|\alpha\rangle$ denotes the excited states of the BChl$a$ molecules, ε_α are the pertinent vertical excitation energies, and $J_{\alpha\beta}$ are electronic couplings between excited states α and β. The diagonalization of the system Hamiltonian results in the set of seven exciton states $|i\rangle$, with the eigenenergies E_i,

$$H_e|i\rangle = E_i|i\rangle. \tag{2.37}$$

2.2.2 Vibronic Dimers

Before describing the dimer Hamiltonian, the theory and notation will be clarified by a brief description of a simple harmonic oscillator with an excited electronic state displaced by an amount, d, along the reaction coordinate, from the ground state. The system can be described with the Hamiltonian given in Eq. 2.35, where the ground and excited state Hamiltonians are, in this case, ($\hbar = 1$)

$$\begin{aligned} H_g &= \varepsilon_g + \frac{p^2}{2m} + \frac{1}{2}m\omega_g^2 x^2, \\ H_e &= \varepsilon_e + \frac{p^2}{2m} + \frac{1}{2}m\omega_e^2 (x-d)^2. \end{aligned} \tag{2.38}$$

Here, the vertical transition energy of the ground (excited) state is $\varepsilon_{g(e)}$, while $\omega_{g(e)}$ is the normal mode frequency of the ground (excited) state, and x, p, and m are the usual reaction coordinate, momentum, and mass, respectively, This can also be written using the creation and annihilation operators:

$$\begin{aligned} a^\dagger &= \sqrt{\frac{m\omega}{2}}\left(x - \frac{i}{m\omega}p\right), \\ a &= \sqrt{\frac{m\omega}{2}}\left(x + \frac{i}{m\omega}p\right), \end{aligned} \tag{2.39}$$

as in

$$\begin{aligned} H_g &= \varepsilon_g + h_g \\ H_e &= \varepsilon_e + h_e + \omega_e \Delta^2 - \omega_e \Delta (a + a^\dagger), \end{aligned} \tag{2.40}$$

with the normal mode Hamiltonian defined as $h_i = \omega_i(a^\dagger a + \frac{1}{2})$, and the displacement along the dimensionless coordinate, $Q = (a + a^\dagger)/sqrt2$, is

$$\Delta = \sqrt{\frac{m\omega_e}{2}}d. \tag{2.41}$$

Given a pair of nearly identical chromophores, each with one electronic excited state, by neglecting the doubly excited state, the electronic Hilbert space of the dimer is three-dimensional:

$$\begin{aligned} |g;\nu_a,\nu_b\rangle &\equiv |a_g;\nu_a\rangle \otimes |b_g;\nu_b\rangle \\ |a;\nu_a,\nu_b\rangle &\equiv |a_e;\nu_a\rangle \otimes |b_g;\nu_b\rangle \\ |b;\nu_a,\nu_b\rangle &\equiv |a_g;\nu_a\rangle \otimes |b_e;\nu_b\rangle, \end{aligned} \tag{2.42}$$

where the subscript g (e) stands for the ground (excited) state of the molecule, and the vibrational states are denoted ν_m, for $m = a, b$. The shorthand notation for a generic state, $|m;\nu_a,\nu_b\rangle$, will be used in the following, along with the ladder operators a and $a^\dagger$ (b and $b^\dagger$) for monomer a (b). The schematic depicted in Fig. 2.1 shows the potential energy surfaces for each molecule, as well as the coupling between their excited states, J_{ab} (assumed to be independent of the nuclear coordinate). Taking the minimum energy of both ground states to be zero, then the total dimer Hamiltonian can be written:

$$H_{dimer} = |0\rangle h\langle 0| + \sum_{m=a,b} |m\rangle\big(E_m + h - \omega_m\Delta_m(m+m^\dagger)\big)\langle m| + J_{ab}(|a\rangle\langle b| + |b\rangle\langle a|), \tag{2.43}$$

where $E_m = \varepsilon_m + \omega_m\Delta_m^2$, and ε_m, Δ_m, and ω_m are the vertical excitation energy, the dimensionless shift of the excited electronic state, and the normal mode frequency of monomer $m = a, b$, respectively, as shown in Fig. 2.1. The vibrational Hamiltonian is $h = h_a + h_b$, where $h_m = \omega_{vib}(m^\dagger m + \frac{1}{2})$.

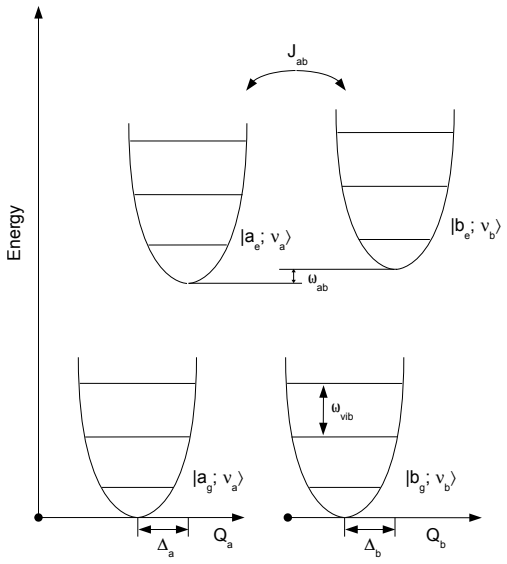

Figure 2.1: Potential energy surfaces for the dimer system along the dimensionless reaction coordinates Q_a and Q_b. Vibrational states are denoted ν.

A commonly employed approach, is to consider this system in the "exciton" basis; that is, the excited states are transformed to a new basis defined by the symmetric (+) and antisymmetric (−) subspaces,

$$|\pm\rangle = \frac{1}{\sqrt{2}}(|a\rangle \pm |b\rangle), \tag{2.44}$$

with corresponding ladder operators

$$\begin{aligned} b_+ &= (a+b)/\sqrt{2},\ b_+^\dagger = (a^\dagger + b^\dagger)/\sqrt{2}, \\ b_- &= (a-b)/\sqrt{2},\ b_-^\dagger = (a^\dagger - b^\dagger)/\sqrt{2}. \end{aligned} \tag{2.45}$$

In this basis, the dimer Hamiltonian can be written

$$\begin{aligned} H_S \quad = \quad & |0\rangle h\langle 0| + |+\rangle(2h + E_+ + J_{ab} - \sqrt{2}\omega\Delta(b_- + b_-^\dagger)\langle +| \\ & +|-\rangle(2h + E_+ - J_{ab} - \sqrt{2}\omega\Delta(b_- + b_-^\dagger)\langle -| \\ & +|+\rangle(E_- - \sqrt{2}\omega\Delta(b_- + b_-^\dagger))\langle -| \\ & +|-\rangle(E_- - \sqrt{2}\omega\Delta(b_- + b_-^\dagger))\langle +|, \end{aligned} \tag{2.46}$$

where $h = h_+ + h_-$ and $E_\pm = E_a \pm E_b$. This Hamiltonian can be partitioned into the symmetric and antisymmetric subspaces. Since the dimer reservoir is often modeled as a symmetric bath (see §2.3), the antisymmetric subspace of the dimer system does not couple to it, and thus can be disregarded when calculating the system-bath interaction.

Upon diagonalization of the system Hamiltonian, the system in the energy eigenstate representation can be partitioned into ground and excited arrays of states. For the purpose of dynamics calculations, only the few lowest states of each array need be retained.

2.3 Dissipation

In order to describe the dissipation term in Eqs. (2.30) and (2.31), or rather the bath correlation functions in Eq. (2.33), the reservoir must be defined for each system under study. Due to the macroscopic nature of a thermal bath, a quantum mechanical description is not possible. In the dimer model under study in this work, a harmonic ocsillator reservoir is employed, a description of which is given in §2.3.2. The FMO complex reservoir is modeled after invoking additional approximations outlined in the following section.

2.3.1 FMO Complex Reservoir

For study of the FMO subunit, consisting of seven electronically coupled BChl molecules, the secular approximation is invoked. In terms of the Redfield operator, Eq. (2.31), this means that only the secular terms in $R_{\mu\nu\kappa\lambda}$, i.e. those that satisfy

$$E_\mu - E_\nu - E_\kappa + E_\lambda = 0, \tag{2.47}$$

are retained. Then the evolution of the diagonal elements of the reduced density matrix are decoupled from the evolution of the off-diagonal elements. According to the Pauli master equation, the dissipation operator for the diagonal elements ("populations") of the system density matrix in the eigenstate (exciton) representation is then

$$\{\Re\rho(t)\}_{ii} = \sum_{j\neq i}(M_{ij}\rho_{ii}(t) - M_{ji}\rho_{jj}(t)). \tag{2.48}$$

To describe the relaxation of populations, we adopt the rates M_{ij} which have been determined in Ref. [38] using a modified Förster/Redfield theory. The dissipation operator for the off-diagonal terms of the reduced density matrix

("coherences") is given by

$$\{\Re\rho(t)\}_{ij} = \xi_{ij}\rho_{ij}(t), \quad \{\Re\rho(t)\}_{ig} = \xi_{ig}\rho_{ig}(t). \tag{2.49}$$

The dephasing of the exciton states is determined by ξ_{ij}, whereas the rate of pure optical dephasing between the ground state and the exciton states is denoted by ξ_{ig}. The rates ξ_{ij} can be estimated as $\xi_{ij} = (M_{ij} + M_{ji})/2 + \xi_{PD}$, where ξ_{PD} is the rate of pure dephasing of the exciton states. In this study, ξ_{ij} and ξ_{ig} are treated as adjustable parameters in order to explore their effect on both the coherent dynamics of the system and the 2D signals. Although the relaxation model is oversimplified and cannot account for coherence transfer or memory effects [47, 52], it is sufficient for our purposes: the systematic study of decoherence and population transfer effects on two-dimensional photon echo spectra within the existing Frenkel exciton model of the FMO complex.

2.3.2 Dimer Reservoirs

Before going into detail about the dimer reservoir, a review of the harmonic oscillator reservoir will be presented. This is in order, in part, to clarify notation, as well as to present full and consistent theory. The harmonic approximation can be used when the molecular complex under study forms a crystalline lattice with high symmetry. At a low enough temperature, lattice vibrations are simply small oscillations around the equilibrium position, and the driving force is proportional to their displacement from the equilibrium position. In this case, normal mode vibrations, called lattice phonons, can be introduced. The harmonic approximation is utilized for the dimer system, the description of which presented here is once again adopted from Ref. [48]. Its application to the dimer system is outlined below.

If a Taylor expansion is performed on H_{SB} with respect to the reservoir

coordinates, all higher-order terms can be neglected and H_{SB} is linear with respect to the harmonic oscillator reservoir coordinates, $q = \{q_\xi\}$. Since each monomer is coupled to an identical bath, Eq. (2.23) can be written as

$$H_{SB} = Q \sum_\xi c_\xi q_\xi, \tag{2.50}$$

where c_ξ is the system-bath coupling constant and Q is proportional to the sum of system creation and annihilation operators. The reservoir is comprised of decoupled harmonic oscillators; thus the bath Hamiltonian takes the form

$$H_B = \sum_\xi H_B^{(\xi)} = \sum_\xi \omega_\xi (C_\xi^\dagger C_\xi + \frac{1}{2}), \tag{2.51}$$

where $C_\xi^\dagger$ and C_ξ are the normal mode oscillator creation and annihilation operators, respectively, and ω_ξ is the normal mode frequency. The harmonic oscillator eigenstates, $|N_\xi\rangle$, are denoted by the quantum number N_ξ, with eigenenergies $E_{N_\xi} = \omega_\xi(N_\xi + 1/2)$. Bath coordinates are $q_\xi = \sqrt{1/2\omega_\xi}(C_\xi + C_\xi^\dagger)$.

We now assume that each degree of freedom of the BChl dimer is coupled to an identical harmonic bath. Using the notation outlined above (that $\langle q_\xi \rangle_R = 0$) and a bit of mathematical manipulation, the Fourier transform of the correlation function now takes the form

$$C(\omega) = 2\pi \sum_\xi \frac{c_\xi^2}{2\omega_\xi}((n(\omega_\xi)+1)\delta(\omega-\omega_\xi) + n(\omega_\xi)\delta(\omega+\omega_\xi)), \tag{2.52}$$

where the Bose-Einstein distribution, the mean occupation number of a harmonic oscillator mode,

$$n(\omega) = \frac{1}{e^{\omega/k_B T} - 1}, \tag{2.53}$$

was introduced, using the Boltzmann constant, k_B, and the temperature, T. If there are only a few bath oscillators, then energy is transferred from the

bath back into the system on a timescale that is equivalent to other relevant timescales. However, if there are more than about 20 bath modes, the recurrence time is found to be near infinity [53] and the spectral density, $J(\omega)$, can be introduced:

$$J(\omega) = \sum_{\xi} g_{\xi}^2 \delta(\omega - \omega_{\xi}), \tag{2.54}$$

with the dimensionless coupling constant g_{ξ} given by $c_{\xi}\sqrt{1/2\omega_{\xi}} = \omega_{\xi} g_{\xi}$. The spectral density will eventually be considered a smooth function of ω. Now, Eq. (2.52) can be further simplified:

$$C(\omega) = 2\pi\omega^2(1 + n(\omega))(J(\omega) - J(-\omega)). \tag{2.55}$$

The spectral density is defined for specific system-bath situations. For the purposes of this research, the Ohmic spectral density is used to define the protein environment, which encapsulates the BChl molecules:

$$\omega^2 J(\omega) = \Theta(\omega)\eta\omega e^{-\omega/\omega_c}, \tag{2.56}$$

and η is simply a normalization factor. The Heaviside step function ensures that $J = 0$ for $\omega < 0$. Using the stationary Redfield approximation ($t \to \infty$) and assuming a harmonic bath, Eqs. (2.33) can be rewritten as

$$Re(\Gamma^{+}_{\lambda\nu\mu\kappa}) = \langle\lambda|Q|\nu\rangle\langle\mu|Q|\kappa\rangle \begin{cases} J(\omega_{\kappa\mu})(1 + n(\omega_{\kappa\mu})) & \text{if } \omega_{\kappa} > \omega_{\mu} \\ J(\omega_{\mu\kappa})n(\omega_{\mu\kappa}) & \text{if } \omega_{\mu} > \omega_{\kappa} \\ \lim_{\omega\to 0} J(\omega)n(\omega) & \text{if } \omega_{\mu} = \omega_{\kappa} \end{cases} \tag{2.57}$$

$$Re(\Gamma^{-}_{\lambda\nu\mu\kappa}) = \langle\lambda|Q|\nu\rangle\langle\mu|Q|\kappa\rangle \begin{cases} J(\omega_{\lambda\nu})(1+n(\omega_{\lambda\nu})) & \text{if } \omega_\lambda > \omega_\nu \\ J(\omega_{\nu\lambda})n(\omega_{\nu\lambda}) & \text{if } \omega_\nu > \omega_\lambda \\ \lim_{\omega\to 0} J(\omega)n(\omega) & \text{if } \omega_\nu = \omega_\lambda. \end{cases} \tag{2.58}$$

The system coordinate takes the usual form: $Q = (a + a^\dagger)/\sqrt{2}$ in dimensionless units.

Now the general harmonic oscillator reservoir will be applied to a dimer. The explicit procedure for the construction of Redfield operator, $\Re$, for the dimer problem is described in detail elsewhere [48, 54]. However, there are several ways to construct the $Q_{ij}Q_{kl}$ term in Eqs. (2.57) and (2.58) in the system-bath interaction. This term can be generalized as

$$Q_{ij}Q_{kl} = (Q_a)_{ij}(Q_a)_{kl} + \gamma(Q_a)_{ij}(Q_b)_{kl} + \gamma(Q_b)_{ij}(Q_a)_{kl} + (Q_b)_{ij}(Q_a)_{kl}. \tag{2.59}$$

where $Q_{a(b)}$ is the coordinate for monomer a (b) and the new parameter, γ, is a correlation parameter [55]. Specifically, if $\gamma = 0$, then there are no cross-couplings and the bath-induced fluctuations are fully uncorrelated. This means that the relaxation of Q_a is solely determined by bath a and the relaxation of Q_b is solely determined by bath b. If $\gamma = 1$, then all of the coupling coefficients are equal, and the bath-induced fluctuations are then fully correlated. Roughly speaking, this means that both of the baths (on average) push or pull the dimer vibrational mode in the same direction with the same strength. If $\gamma = -1$, then the bath-induced fluctuations are fully anticorrelated. Hence, the baths (on average) pull or push the dimer vibrational mode in opposite directions, but with the same strength.

For brevity, the baths with $\gamma = 0, +1, -1$ will be referred to as baths with fully uncorrelated, correlated, and anticorrlated fluctuations, respectively. In previous studies of vibronic dimers within Redfield theory, baths with uncorre-

lated or fully correlated fluctuations have been considered. With this notation, the coordinates and momenta in the symmetric (+) and antisymmetric (-) subspaces can be defined

$$Q_{\pm} = \frac{Q_a \pm Q_b}{\sqrt{2}}, P_{\pm} = \frac{P_a \pm P_b}{\sqrt{2}}. \tag{2.60}$$

Then the system Hamiltonian can be written as the sum of the commuting operators $H_S^{(+)}$ and $H_S^{(-)}$:

$$H_S = H_S^{(+)} + H_S^{(-)}, [H_S^{(+)}, H_S^{(-)}] = 0. \tag{2.61}$$

As per the analysis in Ref. [55], the antisymmetric (symmetric) bath is completely decoupled from the system and can be dropped in the case of fully correlated (anticorrelated) fluctuations.

This means that the total Hamiltonian of the vibronic dimer coupled to two baths with fully correlated or anticorrelated fluctuations can be transformed to the sum of two mutually commuting Hamiltonians. As explained in detail in Ref. [55], for fully correlated fluctuations, the baths have no influence on the antisymmetric Hamiltonian, $H_S^{(-)}$, but $H_S^{(+)}$ is bilinearly coupled through the coordinate Q_+. If the fluctuations are fully anticorrelated, the opposite is true: The baths have no effect on $H_S^{(+)}$, but $H_S^{(-)}$ is bilinearly coupled through Q_-.

In other words, the dimer coupled to baths with fully correlated or anticorrleated fluctuations thus possesses decoherence-free subspaces (see Ref. [56] for definitions). More precisely, the decoherence-free subspace spans the entire Q_- subspace in the case of fully correlated fluctuations and the entire Q_+ subspace in the case of fully anticorrelated fluctuations. There also exists a classical analogue of this phenomenon: Distributions of linear/angular momenta of a particle immersed in a gas with fully correlated or fully anticorrelated collisions do not

relax to equilibrium [57].

Note that despite the vanishing of the commutator between the total symmetric and antisymmetric Hamiltonians, the dynamics in the Q_+ and Q_- subspaces are not completely decoupled, in general. The reason is that the dimer possesses not only continuous, but also discrete degrees of freedom. The antisymmetric system Hamiltonian in the singly excited state is not diagonal in the singly excited state basis. In the case of anticorrelated fluctuations, it is thus impossible to obtain a closed-form dissipation-free Liouville-von Neumann equation for the symmetric reduced density matrix, $\rho^{(+)}(t) \equiv \mathrm{tr}_{B,Q_-}\{\rho(t)\}$, by tracing out the bath and the Q_- degrees of freedom. This observation has clear dynamical manifestations in the behaviors of observables in the Q_+ subspace, as will be seen in §4.2 in detail.

On the other hand, all symmetric system sub-Hamiltonians are diagonal in their respective electronic basis. It is this property which allows for the derivation of an exact non-Markovian master equation for the reduced (dimer) density matrix for baths with fully correlated fluctuations. In this case, the dissipation-free Liouvill-von Neumann equation for the antisymmetric reduced density matrix, $\rho^{(-)}(t) \equiv \mathrm{tr}_{B,Q_+}\{\rho(t)\}$, holds in the ground, singly, and doubly excited exciton states.

There exist two major descriptions of transport and relaxation phenomena in excitonic systems: the vibration-bath-coupling model and the electronic-bath-coupling model. In this work, the focus is on the former. However, the majority of studies of the photoinduced dynamics of molecular dimers has been done within the electronic-bath-coupling model (see, e.g., Refs. [52, 58–60] and references therein). How the results of the vibration-bath-coupling model are translated to the electronic-bath-coupling model can be found in the appendices of Ref. [55]. Qualitatively, all major phenomena found for the vibration-bath-

coupling model have their counterparts for the electronic-bath-coupling model. These include the complete decoupling of one of the baths, the (im)possibility to derive an exact master equation for the reduced dimer density matrix in the case of baths with fully (anti)correlated fluctuations, incomplete relaxations, and the existence of decoherence-free subspaces.

2.4 Calculation of Spectra

2.4.1 System-Field Interaction Hamiltonian

In the case of laser-matter interaction, the time-dependent part of the full Hamiltonian is the system-field interaction, which is defined in the electric-dipole and rotating-wave approximations as

$$H_{SF}(t) = -X\mathbf{E}(t) + H.c. \tag{2.62}$$

The electronic transition dipole operator $\hat{\mu}$ of the exciton system is given by the expression

$$\hat{\mu} = \sum_{i=1}^{N} \mu_i(|g\rangle\langle i| + |i\rangle\langle g|) = X + X^{\dagger}, \tag{2.63}$$

where the μ_i determine the dipole strengths of the excitonic transitions from the ground state, $|g\rangle$, to one of the N excited eigenstates $|i\rangle$.

Consider an experiment in which three temporally spaced fields interact with the system, see Fig. 2.2. The fields are characterized by

$$\mathbf{E}(t) = \sum_{a=1}^{3} Ae^{-(t-t_a)^2/2\Gamma^2} e^{i\omega t} e^{-i\mathbf{k}_a\mathbf{r}}, \tag{2.64}$$

where A, t_a, $\mathbf{k}_a$, and ω are the amplitude, envelope central time, wave vector, and frequency of the pulses. The pulse duration is characterized by Γ, which is

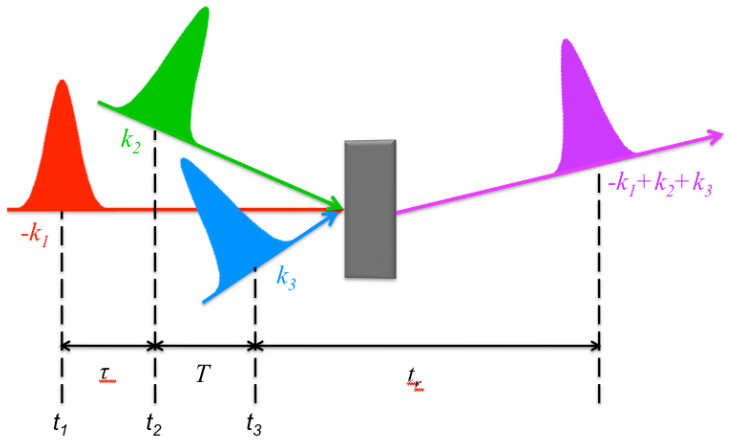

Figure 2.2: Schematic of four-wave (three input + one output) mixing setup.

related to the FWHM of Gaussian pulses by $2\sqrt{2\ln(2)}\Gamma$. Note that all pulses are assumed to have equal amplitudes, carrier frequencies, and durations.

Since the interaction with the laser field is included in the commutator in Eq. (2.30), no *ad hoc* assumption of initial populations is needed. The system is initially in the electronic ground state; when a vibrational mode is included, the ground state population is distributed among vibrational levels using the Maxwell-Boltzmann thermal distribution function

$$\frac{N_i}{N} = \frac{e^{-E_i/k_BT}}{\sum_j e^{-E_j/k_BT}}. \tag{2.65}$$

Subsequent interaction with laser pulses of appropriate duration creates a realistic initial condition.

2.4.2 Photon echo spectroscopy

The signal resulting from the interaction of the system and the electric field in Eq. (2.64) is a function of time and the center times of each laser pulse:

$P_{PE}(t, t_1, t_2, t_3)$. It can be detected in any of the eight directions $\mathbf{k}_s = \pm\mathbf{k}_1 \pm \mathbf{k}_2 \pm \mathbf{k}_3$. For a given system with two electronic levels, and a field that is at or near resonance with the system ($\omega_1,\ \omega_2,\ \omega_3 \sim \omega_{eg}$) the rotating wave approximation (RWA) is invoked in order to neglect the quickly oscillating terms, those proportional to $\omega_a + \omega_{eg}$, and retain only the slowly varying terms, those proportional to $\omega_a - \omega_{eg}$. In order to prevent a highly oscillating term after the second interaction, the first two interactions must have an opposite sign of frequency (one interaction with E, the other with E^*). Therefore, the dominant signal will be produced at the four possible wavevector directions $\pm k_3 \pm (k_2 - k_1)$. The applicable double-sided Feynman diagrams, adopted from Ref. [61], can be seen in Fig. 2.3 on the following page. In photon echo experiments, the signal is detected with the wavevector $\pm\mathbf{k}_s \equiv \pm(-\mathbf{k}_1 + \mathbf{k}_2 + \mathbf{k}_3)$, which selects only the R_2 and R_3 pathways.

The photon echo is generated in the following manner (see Fig. 2.2): Initially the system is assumed to be in its ground state, ρ_{gg}. At a time t_1, the first pulse interacts with the system creating a coherence, ρ_{eg}, which is allowed to evolve during the coherence time, $\tau = t_2 - t_1$. The second pulse then interacts with the system at a time t_2, creating population in either the ground (ρ_{gg}, R_3 pathway) or excited (ρ_{ee}, R_2 pathway) state. The population then evolves during the population time, $T = t_3 - t_2$. Finally, the system interacts with the third pulse at a time t_3, which again creates a coherence. The photon echo signal reaches a maximum when it is allowed to rephase for the same amount of time as it spent in the first coherence, i.e. at a time $t = t_1 + \tau + T + \tau$. The photon echo signal can thus be considered to be a function of the coherence, population, and rephasing times only: $P_{PE}(\tau, T, t_r)$.

For the purpose of calculating photon echo signals, pulse one is chosen to remain fixed at 800 fs, with respect to "absolute" time, and the other two pulses

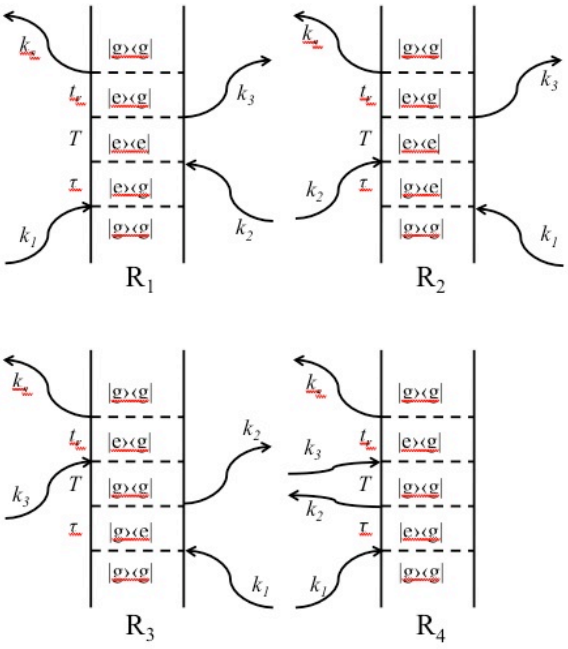

Figure 2.3: Double-sided Feynman diagrams for time-domain four-wave mixing in a two-level system. The diagrams shown are those that survive the rotating wave approximation.

scan across is. The photon echo polarization can now be plotted with respect to the coherence and absolute times, as seen in Figs. 2.4a and 2.5a for a simple two-level system, for two different population times, $T = 0$ and 400 fs, respectively. The horizontal line in each plot indicates the location of t_1. Vertical lines are drawn for $\tau = 0$ and $\tau = -T$. The photon echo signal clearly has a triangular shape, reaching a maximum when $\tau = 0$ and absolute time is 1.2 ps, or $t_1 + T$ (as stipulated above, for $\tau = 0$). Along the absolute time (vertical) axis, no signal will be seen untill all pulses have interacted with the system i.e. $t \gtrsim t_1 + \tau + T$ (the $\sim$ is due to overlap effects). The maximum line is along the diagonal, indicating the situation in which the rephasing time is equal to the coherence time. Along the coherence axis, we see that there is no signal for negative τ until the third peak begins to overlap with the first, i.e. when $\tau \sim -T$.

Figs. 2.4b and 2.5b show the two-dimensional Fourier transform of the signal in the former. A large peak is generated at the freqency of the excited state, in this case set to zero. Because there is only a single excited state, no additional diagonal peaks, and thus no cross-peaks, are generated. For nonzero population times, additional peaks can be seen along the coherence axis, which is caused by taking a Fourier transform over the Heaviside step function in this direction, as explained in detail below. The spacing of these peaks is found to be directly related to the population time.

A commonly employed approach is to split the 2D signal into rephasing and nonrephasing spectra; that is, the Fourier transform over the positive and negative values of the coherence time, respectively. Examples of nonrephasing and rephasing spectra can be seen in Figs. 2.4 and 2.5, panels c and d. For zero population time, the nonrephasing spectrum is shown in Fig. 2.4c. Here, there is no peak along the coherence axis, since there is no signal for negative coherence times. On the other hand, for $T = 400$ fs, the nonrephasing spectrum

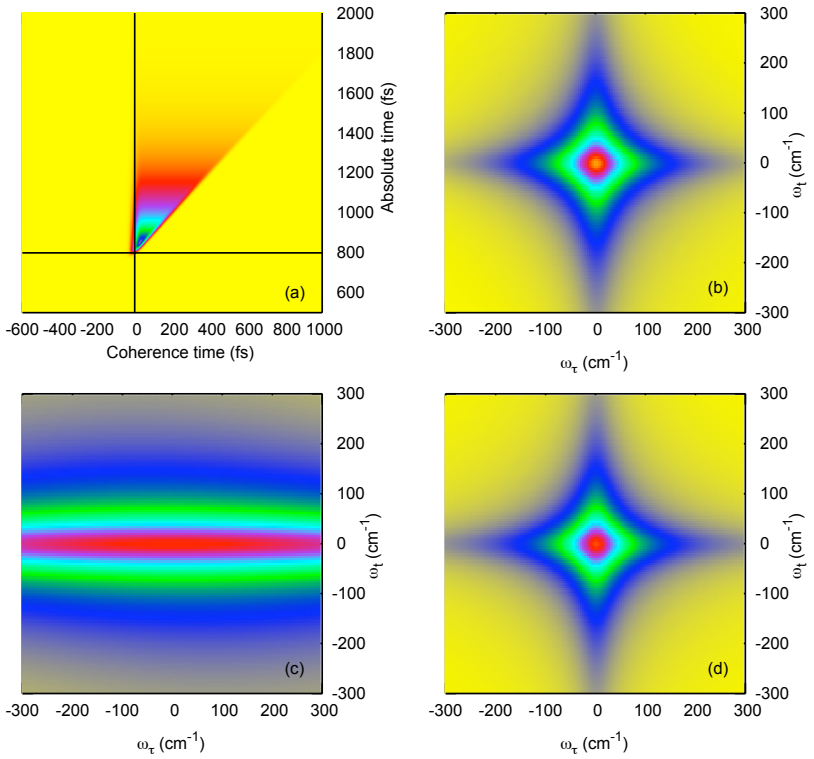

Figure 2.4: (a) Photon echo polarization of a two electronic level system at population time, $T = 0$ fs. Horizontal line drawn at peak one center time, t_1. Vertical line drawn at coherence time, $\tau = 0fs$. (b) Two-dimensional photon echo spectra, i.e. the 2D Fourier transform of (a). (c) Nonrephasing spectrum (Fourier transform over negative τ). (d) Rephasing spectrum (Fourier transform over positive τ). The absolute value is shown for clarity.

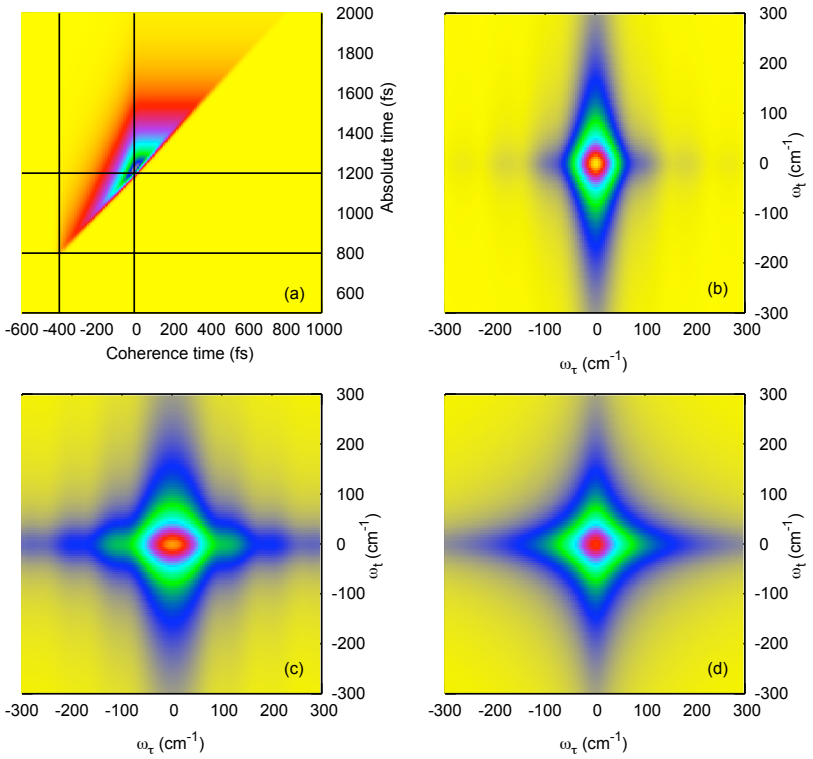

Figure 2.5: (a) Photon echo polarization of a two electronic level system at population time, $T = 400$ fs. Horizontal line drawn at peak one center time, t_1. Vertical lines drawn at coherence times 0 and $-T$. (b) Two-dimensional photon echo spectra, i.e. the 2D Fourier transform of (a). (c) Nonrephasing spectrum (Fourier transform over negative τ). (d) Rephasing spectrum (Fourier transform over positive τ). The absolute value of is shown for clarity.

(Fig. 2.5c), displays the expected peak at $\omega_\tau = 0$ $\mathtt{cm}^{-1}$, as well as very distinct additional oscillations along this axis. For even longer population times, these peaks become more closely spaced (not shown). This artifact is due to taking the Fourier transform over a step function along the coherence axis in the region $-T < \tau < 0$, marked by the two vertical lines in Fig. 2.5c. This results in the sinc function, $\sin(\pi x)/(\pi x)$, where x is proportional to the population time.

Conversely, the rephasing spectra do not show this artifact. Instead of integrating over the Heaviside step function in the region $-T < \tau < 0$, the positive

τ region is characterized by a simple step function. The numerical analysis of this region does not give rise to these additional peaks. As such, only dimer rephasing spectra will discussed in Chapter 5. The FMO spectra, on the other hand, exhibit rather strong signals, such that this artifact does not interfere with the 2D spectra. Therefore, full 2D FMO spectra will be analyzed in Chapter 3.

2.4.3 EOM-PMA

As in any four-wave mixing scheme, the main computational task is the determination of the induced nonlinear polarization obeying a particular phase-matching condition. Recently, an efficient computational scheme, the equation-of-motion phase-matching approach (EOM-PMA [43–45]), has been proposed, which can be implemented to evaluate four-wave mixing signals. The EOM-PMA is valid up to the third order in the system-field interaction, has no limitations with respect to pulse duration, and automatically accounts for pulse-overlap effects.

The particular realization of the method is determined by the required phase-matching condition. In the case of the PE signal, the system of interest interacts with a series of three laser pulses, which are centered at times t_1, t_2, and t_3, and the phase-matching direction is given by $\mathbf{k}_s = -\mathbf{k}_1 + \mathbf{k}_2 + \mathbf{k}_3$, where $\mathbf{k}_a$ ($a = 1, 2, 3$) denote the wave vectors of the three incoming fields [61].

In the EOM-PMA, the polarization in the PE direction can be calculated by simultaneously propagating three auxiliary density matrices (σ_1, σ_2, σ_3), each of which obeys a modified equation of motion [45],

$$\begin{aligned}
\partial_t \sigma_1(t) &= -i[H_S - V_1(t,t_1) - V_2^\dagger(t,t_2) - V_3^\dagger(t,t_3), \sigma_1(t)] - \Re\sigma_1(t) \\
\partial_t \sigma_2(t) &= -i[H_S - V_1(t,t_1) - V_2^\dagger(t,t_2), \sigma_2(t)] - \Re\sigma_2(t) \\
\partial_t \sigma_3(t) &= -i[H_S - V_1(t,t_1) - V_3^\dagger(t,t_3), \sigma_3(t)] - \Re\sigma_3(t),
\end{aligned} \tag{2.66}$$

where the $V_a(t, t_a) = XAe^{-(t-t_a)^2/2\Gamma^2}e^{i\omega t}$ are derived from Eq. (2.62). To third-order, the desired polarization in the PE direction is then obtained as

$$P_{PE}(t_1, t_2, t_3, t) = \mathrm{e}^{i\mathbf{k}_s\cdot\mathbf{r}}\langle X(\sigma_1(t) - \sigma_2(t) - \sigma_3(t))\rangle + c.c., \tag{2.67}$$

where the bracket $\langle \ldots \rangle$ denotes evaluation of the trace. In this work, the fourth-order Runge-Kutta method with a fixed time step (see Appendix A.1 on page 107) has been used to propagate Eqs. (2.66).

The 2D PE experiment uses the heterodyne detection scheme. In the limit of ideal detection, the heterodyne PE signal is proportional to the polarization $P_{PE}(t_1, t_2, t_3, t)$, where t denotes the detection time. Therefore, the ideally detected 2D spectrum can be calculated as

$$S_{PE}(\omega_\tau, T, \omega_t) \sim \int \mathrm{d}\tau \int \mathrm{d}t e^{-i\omega_\tau \tau} e^{i\omega_t t} P_{PE}(\tau, T, t), \tag{2.68}$$

where τ and T denote the delays between the incoming pulses: $\tau = t_2 - t_1$, $T = t_3 - t_2$. The coherence time, τ, corresponds to a period in which the system is in a coherence state after the first interaction with the electric field. The second interaction with the field creates populations, and the delay between the second and the third pulses, T, is therefore referred to as population time. For the case $\tau = 0$, the 2D PE scheme reduces to a frequency-dispersed pump-probe measurement. The population time is thus analogous to the delay time between pump and probe pulses.

The Fourier transforms in Eq. (2.68) are performed over the coherence time τ and the detection time t. The corresponding frequencies ω_τ, ω_t are often refered to as coherence (or absorption) and rephasing (or emission) frequencies, respectively.

The assumption of a Gaussian envelope for the detection pulse (local oscil-

lator) allows for simulation of realistic detection schemes by post-processing of spectral data obtained with Eq. (2.68). To achieve this, the FMO spectra calculated with Eq. (2.68) are convoluted with a Gaussian function $\exp(-\Gamma^2(\omega_t - \omega)^2/2)$ of the rephasing frequency ω_t to account for the finite duration of the pulse width of physical detectors. The detection pulse is centered at the same wavelength ω as the incoming laser pulses, and its duration has the same FWHM of $2\sqrt{2\ln(2)}\Gamma$. As follows from Eq. (2.68), the 2D signal is a complex quantity. In the following, only the part associated with the absorptive changes (the real part) is considered.

The only approximations in the signal calculations of this work are the assumed Gaussian profiles of the field envelopes and the third-order perturbative treatment of the system-field interaction. These assumptions are appropriate for the experiments reported so far. Note, however, that we do not include excited-state absorption (ESA), since our main interest is the detection of coherence survival. ESA is known to influence only the region $\omega_t > \omega_\tau$ of the 2D profiles; our 2D plots do not reproduce the negative contibution due to ESA in this region.

2.4.4 Inhomogeneous Broadening

Static disorder, giving rise to inhomogeneous broadening, occurs due to variations in the excited-state transition energy of each molecule. This can be accounted for by using different realizations of the system Hamiltonian to calculate the polarization, and then average over the resulting spectra [62]. In the present work, fluctuations in the transition frequencies are assumed to obey Gaussian distributions of the form

$$\exp(-(E_i' - E_i)^2/2\sigma_i^2), \tag{2.69}$$

where the σ_i are the standard deviations, resulting in the full width at half maximum (FWHM) of $2\sqrt{2\ln(2)}\sigma_i$. The Box-Muller transform has been used to generate normally distributed random numbers. The effect of inhomogeneous broadening on FMO spectral profiles is studied in detail in §3.2.3.

Chapter 3

FMO Complex

The seven bacteriochlorophyll*a* molecules (BChl) of the Fenna-Matthews-Olson complex (FMO) of *Chlorbium tepidum* is modeled as a system of seven electronic excited states and one common electronic ground state. The parameters of the system Hamiltonian in both the site and the exciton representations were identified from best fits with experimental observables [31, 36–38, 50] as well as calculated independently [51, 63]. The differences in the resulting exciton energies are minor. Here we adopt the set of parameters employed in Ref. [38], since this set has been used for the calculation of 2D spectra, as in the present work. For convenience, Table 3.1 gives site energy levels, ε_α, and electronic couplings, $J_{\alpha\beta}$, and Table 3.2 gives exciton energy levels, E_i, as well as dipole couplings, $|\mu_i|^2$.

The broadening of each exciton transition has been previously estimated from the linear absorption spectrum [38], and is also included in Table 3.2 in terms of FWHM. These data contain both the homogeneous and the inhomogeneous contributions. In order to vary and adjust the strength of the inhomogeneous broadening, we scale the FWHM values of Table 3.2 by a factor

$\delta_{inhom} < 1$.

Table 3.1: Site energy levels and electronic couplings (cm^{-1}) of BChl molecules as in the model of Ref. [38].

	BChl 1	BChl 2	BChl 3	BChl 4	BChl 5	BChl 6	BChl 7
BChl 1	12400	-106	8	-5	6	-8	-4
BChl 2	-106	12540	28	6	2	13	1
BChl 3	8	28	12120	-62	-1	-9	17
BChl 4	-5	6	-62	12295	-70	-19	-57
BChl 5	6	2	-1	-70	12440	40	-2
BChl 6	-8	13	-9	-19	40	12480	32
BChl 7	-4	1	17	-57	-2	32	12380

In this section, we first briefly discuss the exciton dynamics induced by laser excitation and then turn to simulations of the corresponding 2D spectra. Several electronic 2D PE experiments for the FMO complex have been reported: The pioneering work by Brixner et al. [34], followed more recently by measurements of Engel et al. [35], did much to encourage extensive studies on the FMO complex. In Ref. [34], cross peaks indicating couplings between exciton transitions were resolved, and the intensity modulations of the peaks with the popoulation time, T, were highlighted and analyzed. An additional finding was reported in Ref. [35]: It was demonstrated that both diagonal and cross peaks exhibit coherent oscillations of their intensity with respect to the population time. It has been found that these oscillations survive for at least 660 fs [35].

Table 3.2: Exciton energy levels (cm^{-1}), dipole strengths ($|\mu_i|^2$) and FWHM (cm^{-1}) of the linear absorption spectrum [38].

exciton	1	2	3	4	5	6	7
E_i	12101	12265	12346	12397	12442	12526	12600
$\|\mu_i\|^2$	49	87	73	31	82	24	36
FWHM	141	102	129	123	100	102	129

Here, we discuss both the overall 2D spectral profiles for various population times as well as intensity modulations of several diagonal and cross peaks as

a function of the population time. Therefore, we mainly adopt the work by Engel et al. [35] as the experimental reference. The pulse carrier frequencies and durations employed in the calculations are $\omega = 12422$ cm^{-1} (805 nm) and $\Gamma = 17$ fs (40 fs at FWHM), which are very close to the experimental parameters of Ref. [35] (808 nm and 41 fs at FWHM) and Ref. [34] (805 nm and 50 fs at FWHM). The field amplitude is chosen to be $A = 40$ cm^{-1} and corresponds to the weak-field regime.

3.1 Photoinduced Dynamics

Let us first discuss the exciton dynamics which is initiated by a single laser-pulse. The equation of motion, Eq. (2.30), is solved numerically; H_{SF} represents the interaction with a pump pulse of 40 fs (FWHM) duration and centered at $t = 0$. The system is initially in the ground state and the pulse excites all exciton states and creates coherences. Subsequent population dynamics in the exciton representation (diagonal elements $\rho_{ii}(t)$) is shown in Fig. 3.1a. The overall population evolution is determined by the master equation, i.e., by the rates M_{ij} and is thus similar to previous reports [38, 51]. The initial populations created by the pump pulse are, however, different from those estimated in Ref. [38] (by consideration of the spectral distribution of the laser intensity) and obtained in Ref. [51] (by approximate description of excitation by a pulse of 50 fs (FWHM) duration). As is seen in the inset of Fig. 3.1a, which shows the early-time exciton dynamics and the pump-pulse envelope, exciton states two, three, and five are populated almost equally and most efficiently. Exciton four is populated to about 44% of the maximum population, while excitons one and seven are each populated to about 37%, and exciton six to about 27% of the maximum population. Since the excitation pulse (FWHM 736 cm^{-1}, centered at $\omega =$ 12422 cm^{-1}) covers all exciton transitions, the initial populations are primarily

determined by the dipole strengths (c.f. Table 3.2). The populations of states four to seven decay much faster than those of the lower exciton states. Around 40 fs, the preparation process is complete and relaxation rates determine the subsequent dynamics. Note that the employed relaxation rates lead to a longer lifetime of exciton three compared to exciton two, even though exciton three has a higher energy.

Fig. 3.1b shows the coherence between excitons 1 and 3, $\rho_{13}(t)$ (this coherence is chosen since it is of relevance for the discussion of the 2D spectra below). In the absence of dephasing processes, each coherence oscillates with a frequency determined by the energy difference between the coresponding states; for $\rho_{13}(t)$ the resulting period is 136 fs. Within the present model, the oscillations decay within a time scale dictated by the dephasing rate ξ_{13}. The latter can be estimated as $(M_{13} + M_{31})/2 + \xi_{PD} = 0.6\ \text{ps}^{-1} + \xi_{PD}$. Shown in Fig. 3.1b is $\rho_{13}(t)$ obtained with $\xi_{13} = 5\ \text{cm}^{-1} \approx 0.9\ \text{ps}^{-1}$ (blue line) and $\xi_{13} = 20\ \text{cm}^{-1} \approx 3.7\ \text{ps}^{-1}$ (red line). When $\xi_{13} = 5\ \text{cm}^{-1}$, the coherences survive for over 2 ps, while when $\xi_{13} = 20\ \text{cm}^{-1}$, which is dominated by pure dephasing, the coherences survive for about 1 ps.

In Fig. 3.1c, the population dynamics in the local basis (site representation, $\rho_{\alpha\alpha}(t)$) is shown. The coherence dephasing rates are $\xi_{ij} = 5\ \text{cm}^{-1}$ (solid lines) and $20\ \text{cm}^{-1}$ (dashed lines) for all i, j. For clarity, we have picked the excited-state populations of molecules BChl 1 (red lines), BChl 3 (blue lines), and BChl 7 (green lines). The populations of all molecules show pronounced modulations due to exciton coherences that last as long as the coherences survive. The mediating BChl 1 and BChl 7 are seen to be modulated by only one frequency, whereas multiple frequencies contibute to the population dynamics of the BChl 3 excited state. BChl 1, which contributes to excitons three (strongly) and seven (weakly) [38], oscillates with a period of approximately 131 fs, corresponding to

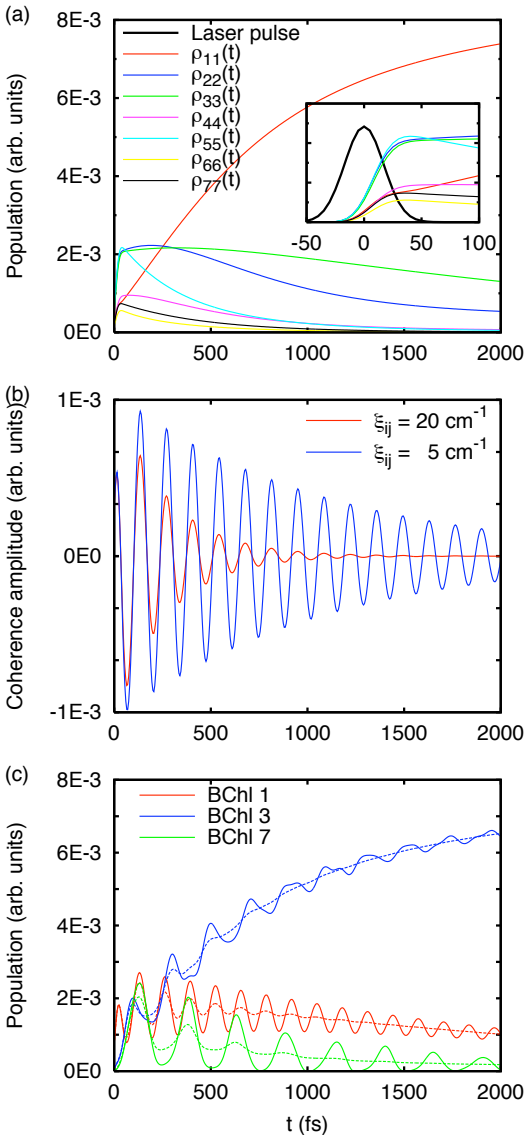

Figure 3.1: (a) Electronic population dynamics of the FMO model in terms of the diagonal elements of the density matrix in the exciton representation, $\rho_{ii}(t)$. (b) Off-diagonal element $\rho_{13}(t)$ of the density matrix in the exciton representation (real part) for two dephasing rates, $\xi_{13} = 5$ cm^{-1} (blue line) and $\xi_{13} = 20$ cm^{-1} (red line). (c) Population dynamics of BChl one, three, and seven (site or local representation of the density matrix, $\rho_{\alpha\alpha}(t)$) obtained with $\xi_{13} = 5$ cm^{-1} (solid lines) and $\xi_{13} = 20$ cm^{-1} (dashed lines).

the coherence between excitons three and seven ($\Delta E_{37} = 254$ cm^{-1}). Similarly, BChl 7, which contributes to excitons two (weakly) and four (strongly) [38], oscillates with a period of about 255 fs. This corresponds to the coherence between excitons two and four ($\Delta E_{24} = 132$ cm^{-1}). The dominating frequency in the BChl 3 dynamics corresponds to the energy difference between excitons one and two ($\Delta E_{12} = 164$ cm^{-1}, period of approximately 200 fs). Note that even a relatively strong exciton dephasing $\xi_{ij} = 20$ cm^{-1} gives rise to pronounced coherent modulations of the local populations at times up to about one picosecond. The picture is very different if the exciton coherences are neglected (see, for example, the supplementary material of Ref. [63]).

3.2 2D Photon Echo Spectra

In addition to the relaxation and dephasing parameters relevant to exciton dynamics, the spectroscopic signals are also strongly influenced by optical dephasing and inhomogeneous broadening. In this section, 2D signals of the model for various population times are calculated and the influence of dephasing processes on 2D profiles are addressed in some detail. Unless otherwise specified, a weak dephasing rate of the exciton coherences is assumed ($\xi_{ij} = 5$ cm^{-1}).

3.2.1 Near-ideal Case

We start the discussion in this section by considering a 2D PE spectrum for population time $T = 0$ for an idealized case of very weak optical dephasing ($\xi_{ig} = 5$ cm^{-1} for all i, which is one order of magnitude less than the average energy difference between successive excitons, 84 cm^{-1}) and no inhomogeneous broadening. Fig. 3.2 shows a very clear pattern in this near-ideal regime: The spectrum exhibits seven characteristic diagonal peaks arising from the transitions to the seven exciton states. The cross peaks, which reflect the couplings

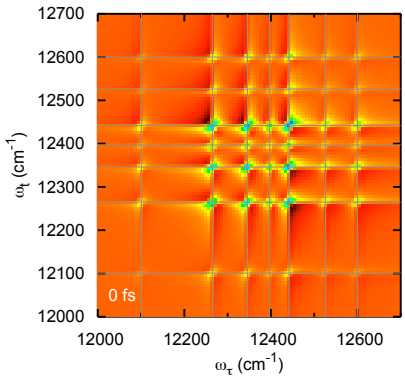

Figure 3.2: 2D PE spectra of the FMO model, calculated with a near-ideal value of the optical dephasing rate ($\xi_{ig} = 5$ cm^{-1}) and without inhomogeneous broadening ($\delta_{inhom} = 0$) at population time $T = 0$ fs. Gray lines are drawn along $\omega_\tau = E_i$ and $\omega_t = E_i$ to indicate the locations of exciton transition energies.

between these transitions (via the common ground state), are also observed at their expected positions. The intensity of the peaks is determined by the dipole strengths of the corresponding transitions and slightly modified due to the finite pulse durations (the pulses are centered at 12422 cm^{-1} and have a width (FWHM) of about 736 cm^{-1}). The effect of excited state absorption (ESA) is neglected in our calculations. Therefore, the spectral intensity above and below the diagonal is expected to be very similar for population time $T = 0$.

3.2.2 Homogeneous Broadening

The experimental peak profiles of Ref. [35] are significantly broader than the spectrum in Fig. 3.2 and the individual peaks are not resolved. This suggests that a realistic optical dephasing (homogeneous broadening) is considerably stronger than the employed, $\xi_{ig} = 5$ cm^{-1}, and that inhomogeneous averaging must also be taken into account. We first consider the influence of these two broadening mechanisms separately, then study their combined effect.

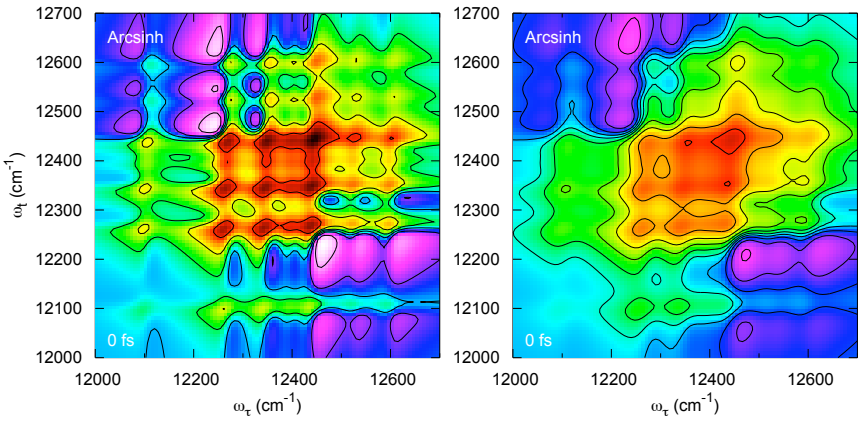

Figure 3.3: 2D PE spectra of the FMO model obtained with an optical dephasing rate of $\xi_{ig} = 20$ $\mathtt{cm}^{-1}$ (left panel) and $\xi_{ig} = 35$ $\mathtt{cm}^{-1}$ (right panel) for population time $T = 0$, in the absence of inhomogeneous broadening. The spectra are displayed with arcsinh scaling to enhance weaker aspects of the peak profiles.

The spectra shown in Fig. 3.3 were calculated using optical dephasing rates $\xi_{ig} = 20$ cm^{-1} (left panel) and $\xi_{ig} = 35$ cm^{-1} (right panel), but without inhomogeneous broadening, $\delta_{inhom} = 0$ (population time, $T = 0$). As expected, larger values of the dephasing rate lead to broader peaks along both the ω_τ and the ω_t axes. However, in both cases, the peaks are still too localized to be considered accurate reproductions of experimental spectra [35].

3.2.3 Inhomogeneous Broadening

In Fig. 3.4, inhomogeneous broadening is included, while the optical dephasing rate is kept at 5 cm^{-1}. Shown are the signals at $T = 0$ for $\delta_{inhom} = 0.5$ (left panel) and $\delta_{inhom} = 0.7$ (right panel). Inclusion of inhomogeneous broadening leads to the averaging of the highly localized diagonal peaks observed in Fig. 3.2 due to variations of transition frequencies. This leads to an elongation of spectra along the $\omega_\tau = \omega_t$ line, as well as a loss of intensity and poor resolution of the

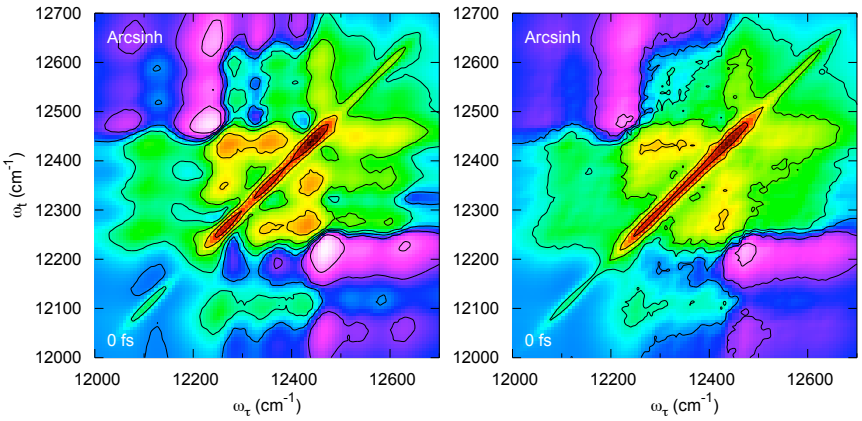

Figure 3.4: 2D PE spectra of the FMO model, calculated with very weak optical dephasing $\xi_{ig} = 5$ cm^{-1} and inclusion of inhomogeneous broadening for population time $T = 0$. $\delta_{inhom} = 0.5$ in the left panel and 0.7 in the right panel. The spectra are displayed with arcsinh scaling to enhance weaker aspects of the peak profiles.

cross peaks. In agreement with the experimental results of Ref. [35], only two peaks can be well resolved along the diagonal: The lower peak corresponds to the spectrally well separated transition to exciton one, while the higher-frequency region represents the contribution from the remaining exciton transitions.

3.2.4 Combined dephasing mechanisms

Finally, Fig. 3.5 shows our best fit of the experimental spectra within the employed simple exciton model. It has been achieved with the optical dephasing rate $\xi_{ig} = 30$ cm^{-1} and $\delta_{inhom} = 0.5$. As in Ref. [35], the signals for four values of the population time $T = 0$, 150, 280, and 600 fs are shown. Since ESA is not included, the simulated signals disregards the negative contibution in the region $\omega_t > \omega_\tau$ (above the diagonal). Otherwise, the agreement with experimental profiles is satisfactory. For larger T, population relaxation leads to an intensity redistribution between the cross peaks [59]. The development of a strong

and broad peak below the diagonal with increasing T is a typical experimental observation [34, 35] and has also been reproduced in previous simulations [38]. This finding is easy to rationalize: Since population relaxation progresses with T, emission occurs at lower frequencies as T increases. The analysis of coherent oscillations in peak intensities is slightly more involved. In the next section the intensity evolution of individual peaks is considered in more detail.

Before closing this section, we briefly address the effect of a stronger exciton dephasing rate ξ_{ij} on the 2D profiles. It can only become prominent at larger population times (cf. Fig. 3.1), since the dephasing becomes more efficient with T. Since dephasing rates scale with the difference in energy between two states, optical dephasing, ξ_{ig}, should always be stronger than the dephasing between excited states, ξ_{ij}. The effect on spectra of stronger ξ_{ij} (5 cm^{-1}, left panel and 20 cm^{-1}, right panel), for a fixed value of the optical dephasing ($\xi_{ig} = 35$ cm^{-1}) at $T = 600$ fs, is shown in Fig. 3.6. As can be seen, the spectral profiles are not strongly influenced by the dephasing rate: Overall peak widths and intensities are relatively unaffected. Since the dephasing between excited states does not significantly alter 2D spectra snapshots, a record of intensity evolution of a particular peak is required to gain information about the decoherence time scale.

3.3 Peak Evolution

In Ref. [35], the intensities of the lowest diagonal peak (DP 1) and of the lower ($\omega_t < \omega_\tau$) cross peak between excitons one and three (CP 1-3) were measured as a function of the population time, T. The intensities of the peaks exhibited strong quantum beating with multiple frequencies for at least 660 fs. The oscillations were attributed to electronic coherences between excitons. Furthermore, it has been argued that coherence transfer takes place; the observed multiple frequencies in the intensity evolution of CP 1-3 were assigned to the frequencies

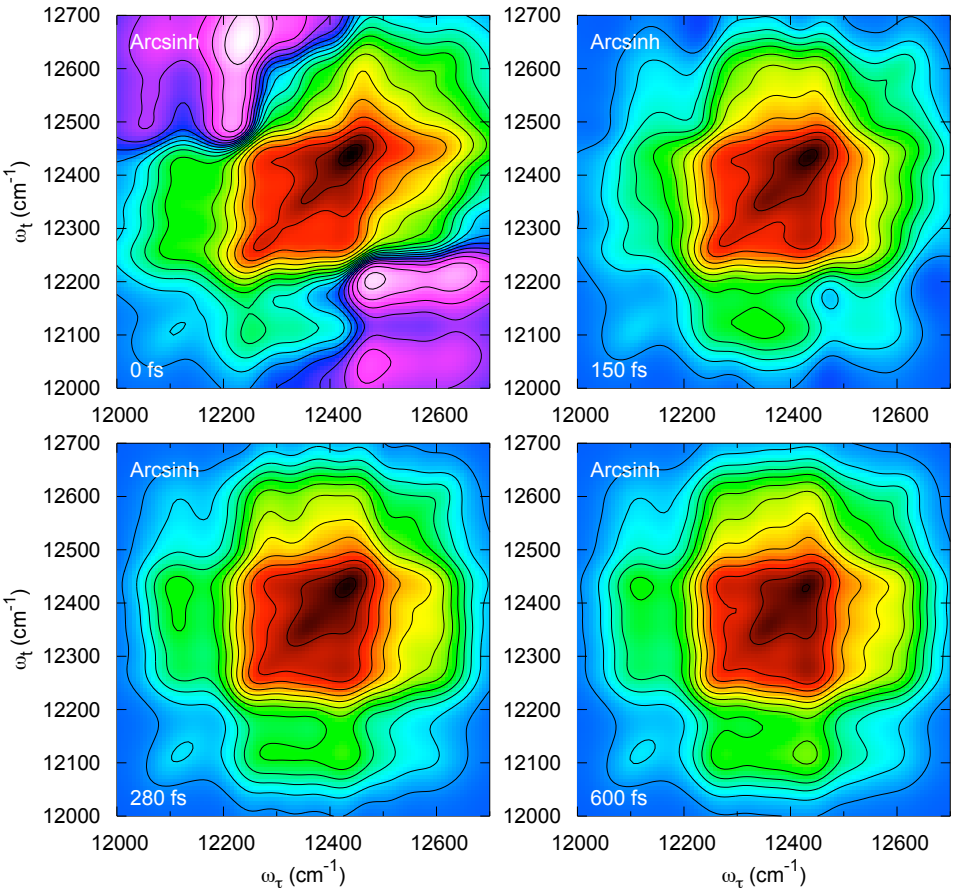

Figure 3.5: 2D PE spectra of the FMO model, calculated with $\xi_{ig} = 30$ $\mathtt{cm}^{-1}$ and $\delta_{inhom} = 0.5$ for various population times as indicated. The spectra are displayed with arcsinh scaling to enhance weaker aspects of the peak profiles. The figure shows the best reproduction of the experimental 2D signals of Ref. [35].

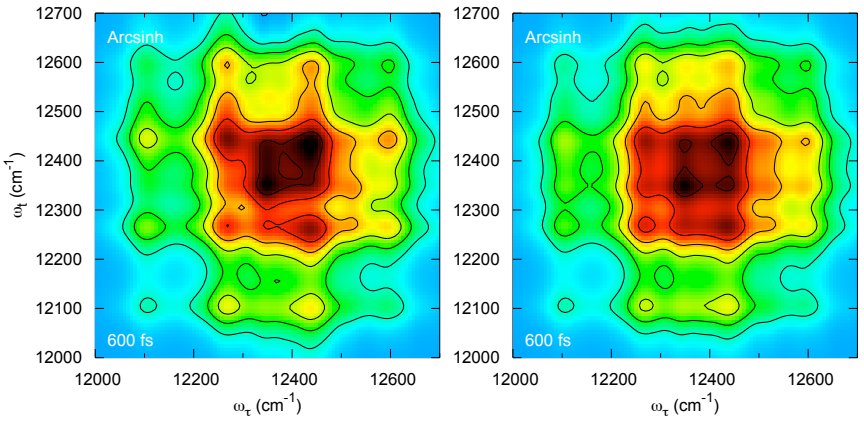

Figure 3.6: 2D PE spectra of the FMO model, calculated with optical dephasing $\xi_{ig} = 35$ $\mathtt{cm}^{-1}$, without inhomogeneous broadening, and for the population time, $T = 600$ fs. The exciton coherence dephasing is $\xi_{ij} = 5$ $\mathtt{cm}^{-1}$ (left panel) and 20 $\mathtt{cm}^{-1}$ (right panel). The spectra are displayed with arcsinh scaling to enhance weaker aspects of the peak profiles.

between all participating exciton transitions.

This interpretation suggests that the bath induces transfer between the excitonic coherences (ρ_{ij}), and simultaneously allow the coherences to survive on an experimentally observable time scale. The model employed in the current section does not include coherence transfer mediated by the bath, but it provides an estimate of coherence lifetimes in the presence of several dephasing mechanisms directly from experimental observables. Chapters 4 and 5 address coherence transfer effects in a dimer of BChl molecules. Note that in the existing simulations of conceptually new 2D spectroscopies for the FMO complex [41, 42], exciton dephasing has not been taken into account.

3.3.1 Cross Peaks

In the absence of dissipation, cross peaks are expected to oscillate with T like the corresponding off-diagonal elements of the reduced density matrix, $\rho_{ij}(t)$,

i.e. with a frequency equal to the energy difference between corresponding excitons [39, 64]. The decay of the oscillations is induced by dissipation. While the coherences of the density matrix decay with the rates ξ_{ij}, the intensity modulations of the cross peaks can be further influenced by the optical dephasing (ξ_{ig}) and inhomogeneous broadening.

As in the reported experiment [35], we focus on CP 1-3 located at $\omega_t = E_1 = 12101$ cm^{-1}, $\omega_\tau = E_3 = 12346$ cm^{-1} as well as on DP 1 at $\omega_t = \omega_\tau = 12101$ cm^{-1}. The calculated intensities of CP 1-3 and DP 1 with respect to the population time are shown in Figs. 3.7 and 3.8, respectively (a 10 fs population time step was employed in the calculations). The dotted line in Fig. 3.7a corresponds to the idealized case of Fig. 3.2, i.e. to the limit of very weak dephasing, $\xi_{ig} = \xi_{ij} = 5$ cm^{-1}, and no inhomogeneous broadening, $\delta_{inhom} = 0$. In this limit, a well-resolved long-lived oscillation in the intensity of CP 1-3 with a period of 136 fs (corresponding to the energy difference between excitons three and one, $E_3 - E_1 = 245$ cm^{-1}) is observed. While an increase in optical dephasing considerably influences the 2D spectral profiles (Fig. 3.3), it does not significantly dampen the oscillations in the cross peak intensity: The dashed and solid lines in Fig. 3.7a have been obtained with $\xi_{ig} = 20$ cm^{-1} and $\xi_{ig} = 35$ cm^{-1}, respectively ($\xi_{13} = 5$ cm^{-1} has been retained).

To demonstrate how cross peak intensity oscillations map the corresponding off-diagonal density matrix elements, Fig. 3.7b shows the evolution of CP 1-3 for $\xi_{13} = 5$ cm^{-1} (solid line) and $\xi_{13} = 20$ cm^{-1} (dashed line). Since the strength of the dephasing scales with the energy difference between states, a value for the optical dephasing $\xi_{ig} = 35$ cm^{-1} is used. As can be seen, the decay of the cross peak oscillation is determined by the dephasing between exciton states, ξ_{13}, in the same manner as the decay of $\rho_{13}(t)$ in Fig. 3.1b. Comparing with experimental results [35], a moderate value of the dephasing rate, $\xi_{13} = 20$ cm^{-1}

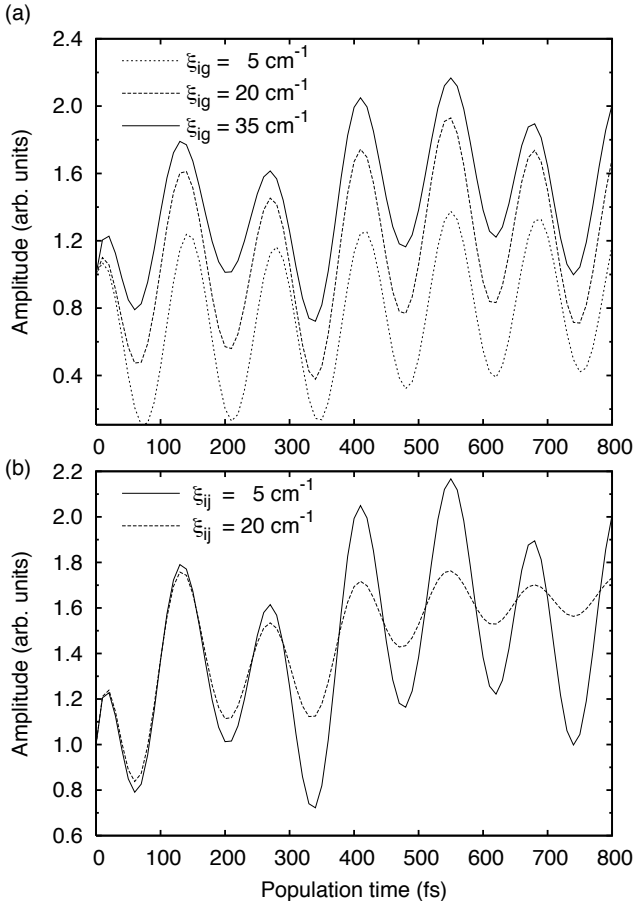

Figure 3.7: The normalized amplitude of CP 1-3 as a function of population time, for (a) various values of the optical dephasing ξ_{ig} with $\xi_{ij} = 5$ $\mathtt{cm}^{-1}$, and (b) various values of the dephasing rate ξ_{ij} with $\xi_{ig} = 35$ $\mathtt{cm}^{-1}$. The solid lines in (a) and (b) represent the same data.

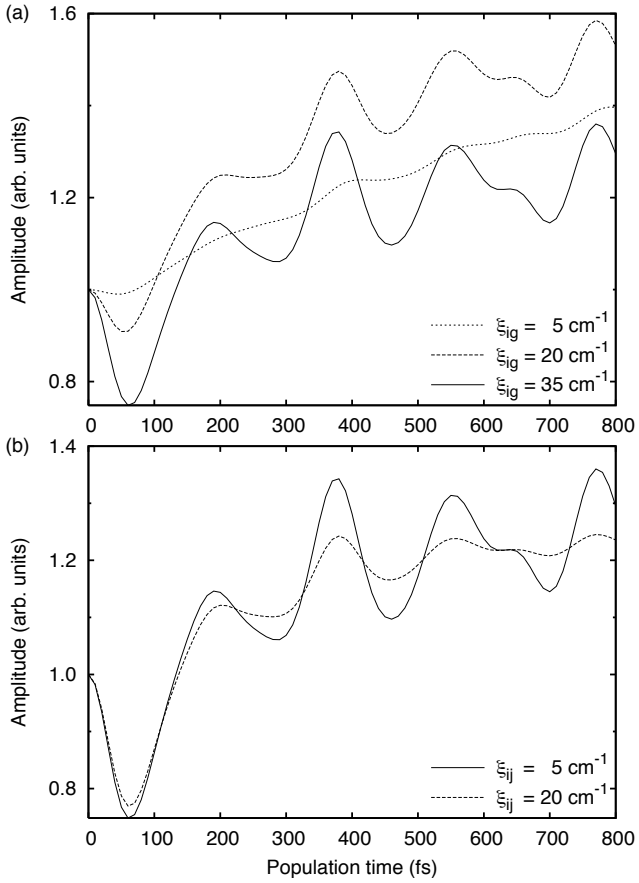

Figure 3.8: The normalized amplitude of DP 1 as a function of population time, for (a) various values of the optical dephasing ξ_{ig} and $\xi_{ij} = 5$ $\mathtt{cm}^{-1}$, and (b) various values of the dephasing rate ξ_{ij} with $\xi_{ig} = 35$ $\mathtt{cm}^{-1}$. The solid lines in (a) and (b) represent the same data.

or weaker, must be used in order to resolve oscillations beyond 660 fs. Indeed, Ref. [65] shows that beating in crosspeak 1–3 survives for about 300 fs even at physiological temperature. This result is attributed to the correlated motion within the protein structure surrounding the chromophores. They conclude that the protein scaffold mediates efficient energy transport despite thermal fluctuations.

3.3.2 Diagonal Peaks

The intensity of DP 1 (Fig. 3.8a, dotted line) exhibits very weak oscillations when idealistic values for dephasing ($\xi_{ig} = \xi_{ij} = 5$ cm^{-1}) and inhomogeneous broadening ($\delta_{inhom} = 0$) are used. As can be seen in Fig. 3.8a, an increase of optical dephasing induces oscillations in the diagonal peak. This effect scales with the strength of the optical dephasing and can be understood by comparing 2D spectra in the ideal case (Fig. 3.2) and in the case of stronger optical dephasing (Fig. 3.3). The modulation is most likely due to the spread of peak widths, which leads to the overlap of the oscillating cross peaks with the diagonal peaks. In the specific case of DP 1, the oscillation can be approximated to be 223 cm^{-1} (corresponding to a period of about 150 fs), which is approximately equal to the energy difference between excitons one and two ($E_1 = 12101$ cm^{-1} and $E_2 = 12265$ cm^{-1}). As can be seen in the left panel of Fig. 3.3, the cross peaks between excitons one and two have spread to such an extent that they overlap with DP 1. This interpretation is confirmed by Fig. 3.8b: Modulations in the amplitude of DP 1 observed for $\xi_{ij} = 5$ cm^{-1} and $\xi_{ig} = 35$ cm^{-1} (solid line) decay faster with an increase of dephasing between the exciton states ($\xi_{ij} = 20$ cm^{-1}, dashed line), since this damps the contributing cross peak oscillations more efficiently. Another source of the oscillations of the diagonal peak intensity is the so-called non-rephasing contribution [40], which is automatically

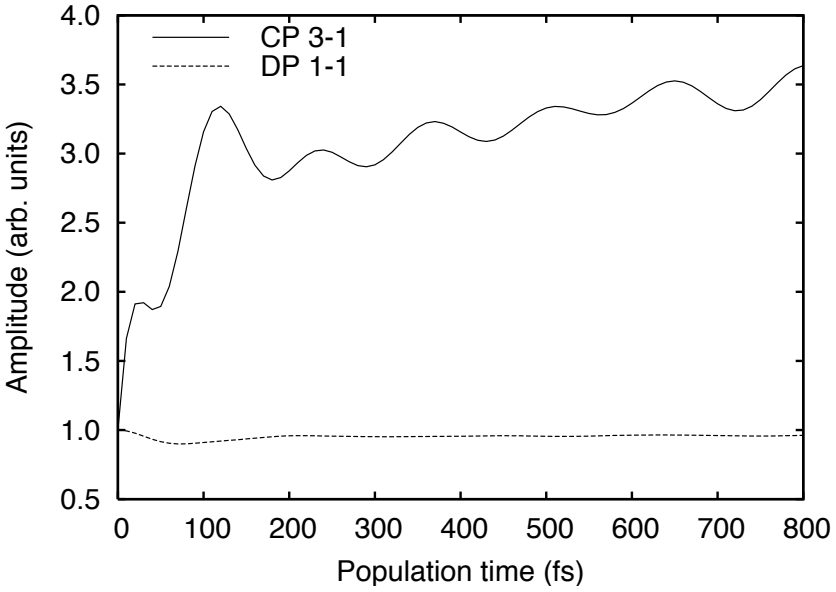

Figure 3.9: The normalized amplitude of CP 1-3 and DP 1-1 as a function of population time using parameters that best reproduce the experimental 2D spectra: $\xi_{ig} = 30$ $\mathtt{cm}^{-1}$ and $\delta_{inhom} = 0.5$ (cf. Fig. 3.5). A weak dephasing, $\xi_{ij} = 5$ $\mathtt{cm}^{-1}$, is used.

taken into account in the present calculations.

So far, we did not include the effect of the inhomogeneous broadening on the peak intensity modulations with population time. The best reproduction of the experimental 2D spectra [35] (cf. Fig. 3.5) is obtained with the adjustable parameters of $\xi_{ig} = 30$ cm^{-1} and $\delta_{inhom} = 0.5$. In this case, we find that the coherent modulation of CP 1-3 is reduced and that of DP 1 cannot be resolved, even in the case of slow dephasing ($\xi_{ij} = 5$ cm^{-1}), as can be seen in Fig. 3.9. This finding indicates that the signatures of excitonic coherences are rather sensitive to inhomogeneous dephasing.

In the reported experiment both CP 1-3 and DP 1 are found to oscillate with multiple frequencies [35]. Within the model employed in this study, each cross peak at a particular $\omega_t = E_i$, $\omega_\tau = E_j$ is expected to oscillate with a

single frequency determined by the energy difference $|E_i - E_j|$. The additional frequencies in CP 1-3 (found experimentally [35]) could arise due to the overlap of broadened neighboring peaks. The effects of broad cross peaks on diagonal peaks are observed here, yet they are insufficient to produce additional oscillations in either diagonal or cross peak intensities. This result strongly suggests that another physical mechanism must be involved. A possible hypothesis is that the bath initiates a very fast coherence transfer so that the evolution of each off-diagonal element of the system density matrix depends on several frequencies $|E_i - E_j|$. So far, this has not been theoretically confirmed, although a number of developments have recently emerged [52, 66]. Another possibility is that high-frequency vibrational degrees of freedom of the monomers are excited in the experiment which give rise to the observed oscillations.

Chapter 4

Photoinduced dynamics of vibronic dimers

Consider the standard model of a molecular chromophore, which consists of two electronic states coupled to a number of vibrational modes. If the modes can be modeled as harmonic and the electron-vibrational coupling is at most quadratic in the vibrational displacements, then the dynamics of the system and its nonlinear response to external fields can be calculated exactly.[61] If two such molecules form a dimer, their mutual (usually dipole-dipole) interactions cause intermonomer electronic couplings, which complicate the electronic and vibrational dynamics and render the ensuing nonlinear responses more difficult to calculate and to interpret.

There exist two major approaches to the modeling of energy transport and relaxation phenomena in exictonic systems, and dimers in particular.[61, 67, 68] In the first approach, a few high-frequency optically active vibrational modes are incorporated into the system Hamiltonian and treated explicitly. The rest of the vibrational modes are assumed to form a thermal reservoir. The reservoir

is normally treated as harmonic, with bilinear system-bath coupling. In the second approach, all vibrational modes are incorporated into the reservoir. In this representation, the vibrational (usually harmonic) reservoir is coupled to the system's electronic degrees of freedom directly, inducing fluctuations of the site energies. Hereafter, these approaches will be referred to as the vibration-bath-coupling model and the electronic-bath-coupling model, respectively.

The two models of the exciton transport are, in principle, equivalent. Via a canonical transformation, one can switch from one description to the other by incorporating the system modes into the bath or by singling out several (high-frequency) modes from the bath and treating them explicitly (see Refs. [69–72] for a comprehensive discussion). In the present study of vibronic dimers, the vibration-bath-coupling model is investigated for the following reasons: We are primarily interested in the study of vibrational and electron-vibrational coherent effects, which requires the explicit consideration of spectroscopically-relevant vibrations. Furthermore, the exact treatment of certain high-frequency modes, which are strongly coupled to the electronic degrees of freedom, allows us to assume that the remaining bath modes are coupled to the monomers rather weakly. This assumption justifies the use of Redfield theory for the description of the vibrational relaxation of the dimer.

Exact results concerning the photoinduced dynamics of vibronic dimers are scarce in the literature. The Hamiltonian of a symmetric dimer with a single vibrational mode per monomer can be partitioned into the sum of the commuting Hamiltonians in the symmetric and antisymmetric vibrational subspaces. [10] If the energies in the single-exciton subspace are doubly degenerate (e.g. molecules of D_4 symmetry with Jahn-Teller active vibrational modes), a $\pi/4$-rotation diagonalizes the Hamiltonian and reduces the problem to a displaced harmonic oscillator. [73, 74] Certain exact results also exist beyond the strictly degener-

ate case (see, for example, Refs. [12, 75–78] and references therein). Beyond these exact results, several approximate methods are widely employed for the investigation of the photoinduced dynamics of molecular dimers: Redfield theory, [8, 36, 79–81] the stochastic Schrödinger equation, [82, 83] or the quantized Hamiltonian dynamics. [83] If vibrational relaxation and thermal fluctuations can be neglected on the timescale of interest, the Schrödinger equation can be solved numerically to obtain the spectroscopic observables. [84, 85] More generally, third-order response functions are used for the calcuation of spectroscopic signals of dimers and other multi-exciton systems. [67, 73, 86–88]

The origins of long-lived coherent optical responses of dimers [89, 90] and more complex aggregates coupled to dissipative environments [35, 91–97] are being actively debated at present. This Chapter addresses the dissipative dynamics of the vibronic dimer, which is a minimal model relevant for the analysis of the dynamics of multi-exciton systems. The dimer comprises a pair of electronic two-level systems, each of which possesses a vibrational mode. Through these vibrational modes, the dimer is bilinearly coupled to a harmonic reservoir. Using firmly established results regarding relaxation pathways [55] as a guideline, the relaxation of vibronic dimers is studied in detail numerically, with emphasis on the effects of bath-induced correlations on the dimer dynamics. Redfield theory is used to study the relaxation of the dimer vibrational modes and the evolution of populations and coherences of the dimer density matrix, considering the evolution of the bath-induced fluctuations from the fully uncorrelated to the fully anticorrelated.

For the purposes of these simulations, $\Delta = \Delta_a = \Delta_b$ will be varied in order to observe the effect of increasing the excited state displacement, as well as the effect of varying an asymmetry between the molecules ($\Delta_a \neq \Delta_b$), on the system dynamics. The chromophores are assumed to be bilinearly coupled to two baths

(§2.3.2), which are modeled using the Ohmic spectral density (Eq. 2.56). A moderate vibrational dissipation, $\eta = 0.2$, is assumed. The cutoff frequency, $\omega_c = 600$ $\mathtt{cm}^{-1}$, is on the order of magnitude of the system-mode vibrational frequency. To emphasize coherent effects, the temperature is taken to be low, $T = 4.5$ K.

Electronic dipole moments were found after transformation of the matrix of electronic dipole moments from the exciton basis (given in Ref. [38]) to the site basis, resulting in $\mu_a = 3.8249$ D and $\mu_b = 6.8718$ D. The pulse carrier frequency is in the infrared: $\omega_{field} = 900$ $\mathtt{cm}^{-1}$, (note the use of reduced energies throughout) which is only slightly closer to the energies of eigenstates 5 and 6, than to states 3 and 4 (see Table 4.1). The pulse duration of 30 fs at FWHM corresponds to a width of 980 $\mathtt{cm}^{-1}$ in the frequency domain, and so the laser pulse creates populations of all states in listed in Table 4.1, as well as higher states and coherences.

Table 4.1: Eigenenergies of the first nine eigenstates for each value of the coordinate displacement in the symmetric case, i.e. $\Delta = \Delta_a = \Delta_b$. All values are given in $\mathtt{cm}^{-1}$.

Δ	0.5	1.0	1.5	2.0
E_1	0	0	0	0
E_2	206	190	179	175
E_3	751	752	750	747
E_4	757	759	751	750
E_5	950	934	929	925
E_6	956	940	932	929
E_7	1501	1502	1499	1498
E_8	1508	1508	1501	1501
E_9	1512	1509	1503	1502

The Redfield equation (Eq. 2.30) is converted in to matrix form, by an expansion in terms of the eigenstates of the system Hamiltonian. The field-matter interaction is treated numerically exactly. The fourth-order Runge-Kutta method

is used for the propagation of the reduced density matrix (see Appendix A.1 for details).

4.1 Photoinduced dynamics for uncorrelated baths

In the following discussion, the dynamics of the system after excitation by a single laser pulse is discussed, for which the two electronically excited states are displaced along the dimensionless coordinate axis from their respective ground state by an equal amount, $\Delta \equiv \Delta_a = \Delta_b = 1.5$. Initially, the dimer is in the electronic ground state, while vibrational levels are populated according to the thermal distribution given in Eq. (2.65). Additionally, the baths are assumed to be uncorrelated ($\gamma = 0$). Upon interaction with a laser pulse, dynamics of the first six eigenstates can be seen in Fig. 4.1a; higher states are not shown due to their negligible population. States 5 and 6 are initially more efficiently populated than states 3 and 4, while relatively little population is transfered to the lowest eigenstate.

Pumping is complete within about 25 fs; after which dissipation dominates the dynamics. The system-bath interaction is characterized by the coupling, $\eta = 0.2$, and the bath cutoff frequency, $\omega_c = 600\ \mathtt{cm}^{-1}$, and the temperature used is $T = 4.5$ K. With these parameters, eigenstates 3 through 6 decay within about 200 fs, and population transfers to the lowest eigenstate, as expected. Eigenstate 2, however, decays significantly slower than higher states. This is due to the weak coupling between the molecules: Higher states relax to the ground state of their respective molecule; subsequently, population transfers from state $|b;0,0\rangle$ to state $|a;0,0\rangle$ at a rate corresponding to the coupling strength, $J_{ab} = -62\ \mathtt{cm}^{-1}$.

The dynamics of the coherences between the lowest three eigenstates is shown in Fig. 4.1b. The dominant oscillation in these coherences is proportional to the

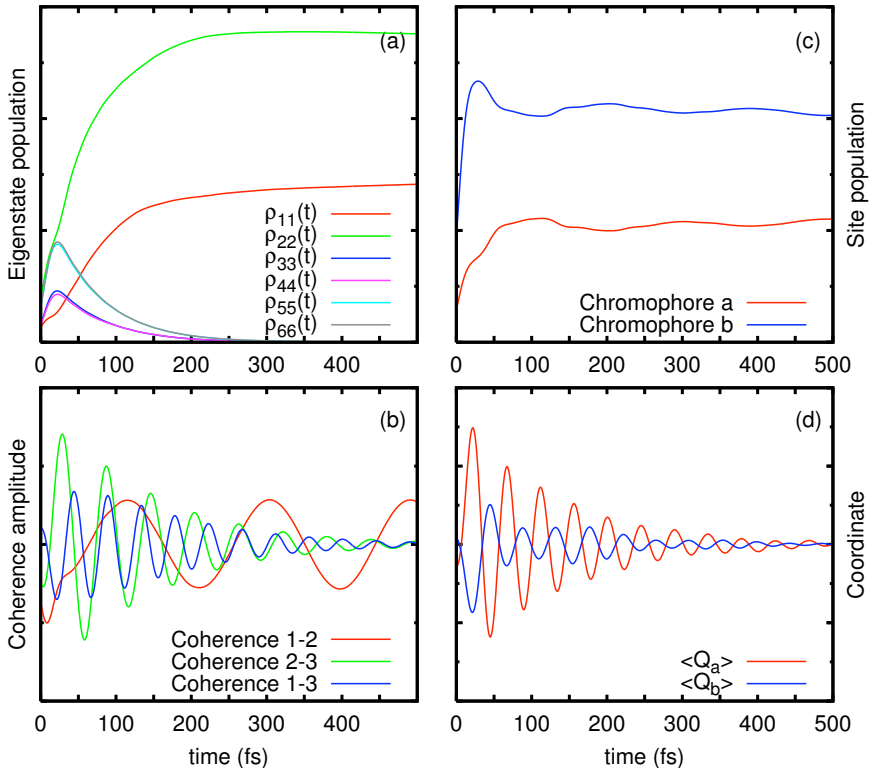

Figure 4.1: Dynamics for the dimer system with $\Delta = 1.5$ for (a) the first six eigenstates; (b) coherences 1-2, 2-3, and 1-3; (c) total populations in the local electronically excited states for chromophores a and b; (d) normalized coordinate dynamics for chromophores a and b.

energy difference between corresponding eigenstates, as expected. For example, coherence 1–2 oscillates with a period of $T = 186$ fs, consistent with $\omega_{12} = 179$ $\mathtt{cm}^{-1}$; coherence 2–3 has a period of about 59 fs, closely corresponding to $\omega_{23} = 572$ $\mathtt{cm}^{-1}$; and coherence 1–3 oscillates with period of about 44.5 fs, approximately equal to $\omega_{13} = 750$ $\mathtt{cm}^{-1}$. Except for coherence 1–2, which has a pronounced lifetime longer than 3 ps, coherences decay on a timescale of about 500 fs. The rate of decay depends on system-bath coupling strength. Notice the fast oscillation in coherence 1–2 in the first 100 fs. Its origin and dependence on the displacement will be discussed in the following.

The population dynamics in the local basis (site representation $\rho_{\alpha\alpha}$) of the excited electronic states of chromophores a and b is shown in Fig. 4.1c. A weak modulation on the order of ω_{12}, can be seen due to exciton coherences. This oscillation has a period of about 162 fs (206 $\mathtt{cm}^{-1}$). Its behavior on the coordinate displacement will also be studied in detail below.

The dynamics of the normalized coordinate expectation values, $\langle Q_a \rangle$ and $\langle Q_b \rangle$, (where the brackets imply normalization by the population of the electronically excited state of chromophore i, i.e. $\langle Q_i/P_i \rangle$) is shown in Fig. 4.1d. Both coordinate expectation values oscillate around 1.5 as expected, since $\Delta_a = \Delta_b = 1.5$, with a period of about 45 fs; This corresponds closely to $\omega_{vib} = 750$ $\mathtt{cm}^{-1}$ (compare with 737 $\mathtt{cm}^{-1}$). For this value of the displacement, ω_{vib} is approximately equal to ω_{13}. However, as the coordinate displacement is varied, thereby modifying ω_{13}, this oscillation remains consistant (not shown) and can therefore be attributed to the vibrational energy.

Now the effect of varying the coordinate displacement on system dynamics is studied. Site population dynamics for various values of the displacement is shown in Fig. 4.2. Notice that the efficiency decreases both for the largest and the smallest values of the coordinate displacement. This is due to the fact that

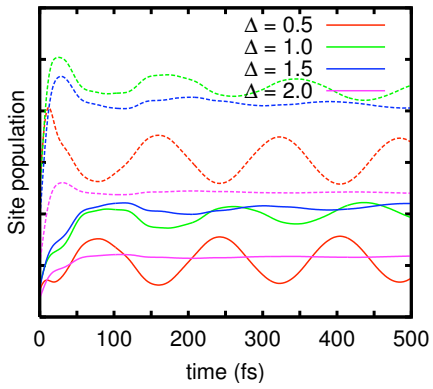

Figure 4.2: Population dynamics of the electronically excited state of chromophore a (solid) and b (dashed), for various values of the coordinate displacements (colors as indicated).

the electronic dipole moments, (via Franck-Condon overlaps), determine the efficiency of population transfer; see Appendix A.2 for details on calculations of Franck-Condon overlap integrals. Thus, even though ω_{field} is approximately centered between the degenerate pairs of eigenstates: 3, 4 and 5, 6, the efficiency of population transfer is not constant when the displacement is varied. For example, when $\Delta = 0.5$, the Franck-Condon factor, which is proportional to the square of the overlap $\langle 0|0\rangle$, is relatively large and decreases significantly as the coordinate displacement increases. On the other hand, the overlap $\langle 0|i\rangle$, for $i = 3, 4, 5, 6$, are quite small and increase only a small amount as the displacement increases.

Modulation in the site population dynamics arises due to the excitonic nature of the system. As seen in Fig. 4.2, the weak modulation in the site populations becomes more pronounced as Δ is decreased. For $\Delta = 0.5$, it is easily measurable, and clearly related to ω_{12}, with a period of 162 fs (206 $\mathtt{cm}^{-1}$). This oscillation survives for at least 3 ps in this case (not shown), and for $\Delta = 1.0$, it decays in about 2.5 ps.

While 2D PE spectroscopy is believed to provide information about system coherences, in the model considered here, the coherences are represented by the off-diagonal elements of the reduced density matrix in the system eigenstate representation, $\rho_{\mu\nu}$. If initially nonzero and in the absence of dissipation, they evolve with time as $\exp\{-i\omega_{\nu\mu}t\}$. The eigenenergies listed in Table 4.1 therefore provide an idea as to which frequencies will be present in the coherent dynamics. According to Table 4.1, the eigenstate structure is only slightly modified for various displacement values of the symmetric dimer. Therefore, the coherences between the same eigenstates can be directly compared.

Coherence dynamics for various values of the coordinate displacement is shown in Fig. 4.3. Coherences 1–3 and 2–3 oscillate at ω_{23} and ω_{13}, respectively, for all values of the displacement as expected. Slight modifications in the oscillation frequency arise due the slight variances in the eigenstate values; see Table 4.1 for eigenenergies for each case. Coherence 1–2 also oscillates at ω_{12} as expected, however, an additional fast oscillation can be seen in the first 200 fs. This fast oscillation has a period of approximately 46 fs, corresponding to an energy of 724 $\mathtt{cm}^{-1}$, which is close (less than 4% discrepancy) to the vibrational energy of the chromophores. As the coordinate displacement increases, the strength and detectability likewise become more pronounced. Notice that the manner in which this fast oscillation in coherence 1–2 depends on the coordinate displacement is opposite of the effect of increasing coordinate displacement on electronic site population dynamics.

Fig. 4.4 shows the coherence between the eigenstates 1 and 2 (panel (a), $\omega_{21} = E_2 - E_1 = 206, 190, 179$ cm^{-1} for the three displacements considered) and between 2 and 6 (panel (b), $\omega_{62} = E_6 - E_2 = 750, 750, 753$ cm^{-1} for $\Delta = 0.5, 1, 1.5$, respectively). These are two of the most dominant system coherences generated upon laser excitation. They represent two major time

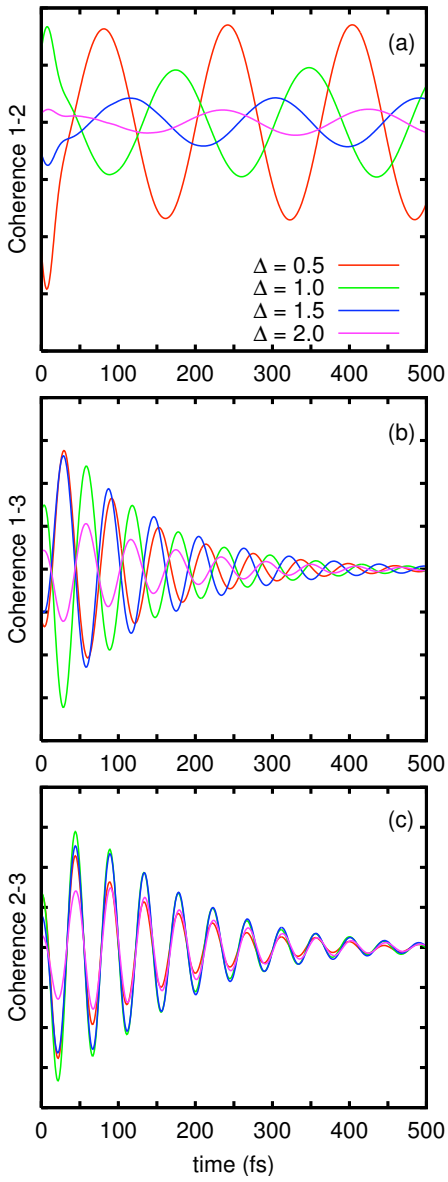

Figure 4.3: Dynamics of the coherences involving the first three eigenstates for various values of Δ (colors as indicated). The coherences shown in each panel should not have the same frequency, as the various coordinate displacements give rise to slightly different eigenvalues (see Table 4.1).

scales of the coherent system dynamics: The slow oscillation is due to eigenstates closely spaced in energy (as the lowest states 1 and 2 shown in panel (a)), and is mainly determined by the coupling J_{ab} and the vertical energy gap of the two excited states $\varepsilon_b - \varepsilon_a$. The faster oscillation is between eigenstates separated by about one vibrational quantum (e.g. states 2 and 6 shown in panel (b)), and the corresponding frequency depends on both the vibrational frequency and on the coupling J_{ab}. Since the eigenstates separated by about one or more vibrational quanta are only significantly populated when the difference between the equilibrium geometry of the electronic states (here Δ) is not negligible, these types of coherences are often referred to as vibrational coherences. If only the lowest vibrational states are mostly populated upon optical excitation, then the created coherence is of purely electronic origin. Therefore, the coherences like the one between the lowest eigenstates 1 and 2 are often referred to as electronic coherences.

Coherence 1–2 shows a very slow decay on the considered timescale, while coherence 2–6 decays almost completely. The reason for this is that the bath cut-off frequency is 650 cm^{-1}, and the system eigenfrequencies close to this value experience the strongest influence of the bath. The amplitude of the low-frequency "electronic" oscillation (coherence 1–2) has been reduced by a factor of four in Fig. 4.4 in case $\Delta = 0.5$, while no scaling has been performed for the fast coherence 2–6. Therefore, for the smallest displacement value, we expect the lower-frequency oscillation to dominate the system dynamics. For Δ =1 , 1.5, on the other hand, the two coherences are on the same order of magnitude. This allows for the observation of the effect of coherence transfer by the bath: At short times, coherence 1–2 is modulated by its higher-frequency vibrational counterpart.

Incorporating a small asymmetry between the coordinate displacements of

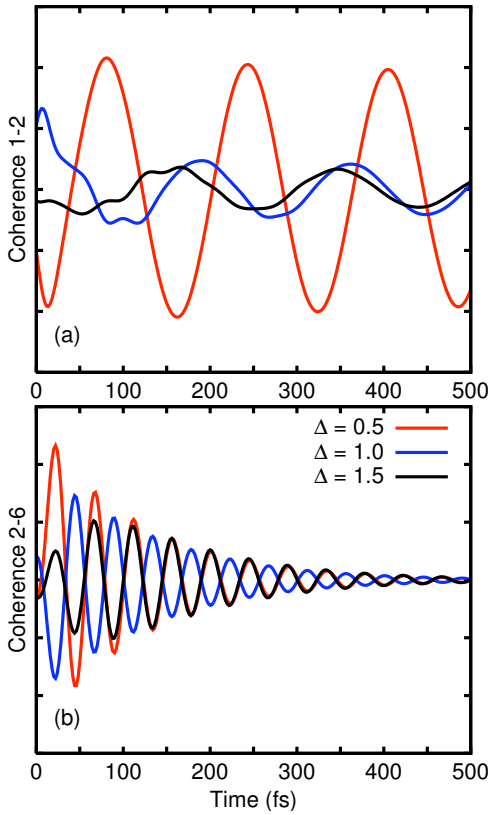

Figure 4.4: Coherences 1–2 (ρ_{12}) (a) and 2–6 (ρ_{26}) (b) in the symmetric case $\Delta_a = \Delta_b$ =0.5 (red), 1.0 (blue) and 1.5 (black).

each monomer leads to only slight changes in the dynamics of the system, as can be seen in Fig. 4.5. The top panel shows the dynamics of the electronically excited state of each monomer (solid lines denote BChl a and dashed lines are for BChl b) for the symmetric case ($\Delta_a = \Delta_b = 1.5$ shown in red), and for the two asymmetric cases: $\Delta_a = 1.5$, $\Delta_b = 1.3$ (green) and $\Delta_a = 1.3$, $\Delta_b = 1.5$ (blue). The same color scheme is used to show the dynamics of coherence 1–2 in the bottom panel. Here, it can be seen that, as in the symmetric case, coherence 1–2 beats with a frequency equal to the energy difference, ω_{12}, and at short times, it also exhibits a fast oscillation, which is consistent with the vibrational energy.

This asymmetry is now increased such that one monomer's electronically excited state is displaced by 0.5 and the other by 1.5, and the dynamics are presented in Fig. 4.6. The left panels (site population dynamics in (a) and coherence 1–2 dynamics in (b)) shows the cases for which Δ_b is fixed at 1.5, while $\Delta_a = 1.5$ (for the symmetric case, shown in red) or $\Delta_a = 0.5$ (the asymmetric case, shown in blue). The dynamics for these two situations are remarkably similar to each other. Again, the population transfer rate between monomers is nearly unchanged, and the weak modulation in site population dynamics is related to the oscillation in coherence 1–2. Notice, however, that an additional fast modulation appears in the site population dynamics of the asymmetric case, which can be seen for very short times (< 100 fs).

Switching the displacement asymmetry leads to significantly different dynamics, as shown in the right panels of Fig. 4.6 (site population dynamics in (c) and coherence 1–2 dynamics in (d)). Here, Δ_b is fixed at 0.5, and the symmetric case ($\Delta_a = 0.5$, red) is compared with the asymmetric case ($\Delta_a = 1.5$, blue). In the site population dynamics, the strong oscillation seen in the symmetric case (proportional to ω_{12}) becomes weaker when the asymmetry is added. However,

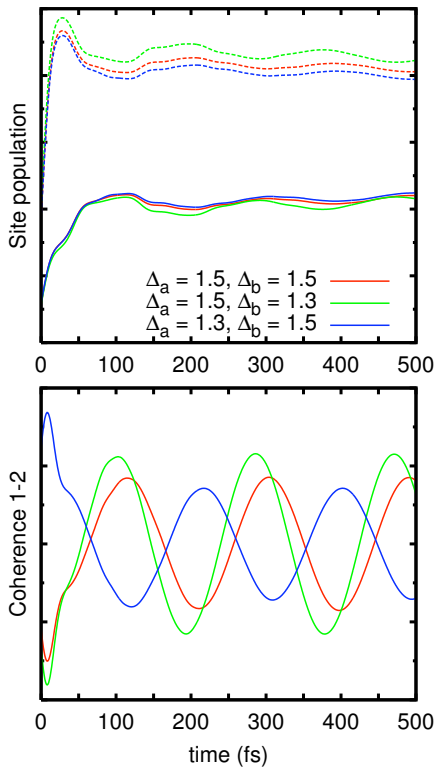

Figure 4.5: (Top panel) Population dynamics of the electronically excited state of chromophore a (solid) and b (dashed) in the local basis, and (bottom panel) dynamics of coherence 1–2 (ρ_{12}) for various small asymmetries in the values of the coordinate displacements (colors as shown).

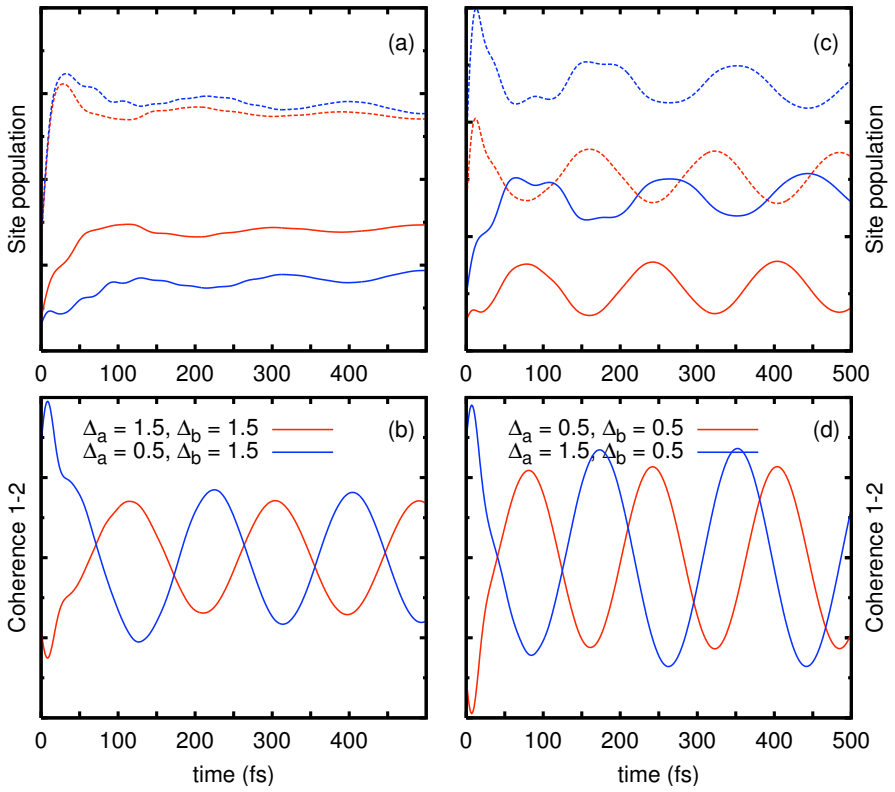

Figure 4.6: (Top panels) Population dynamics of the electronically excited state of chromophore a (solid) and b (dashed) in the local basis, and (bottom panels) dynamics of coherence 1–2 (ρ_{12}) for various large asymmetries in the values of the coordinate displacements. Red lines denote the symmetric cases: $\Delta = 1.5$ (left panels) or $\Delta = 0.5$ (right panel). Blue lines denote the asymmetric cases: $\Delta_a = 0.5$ and $\Delta_b = 1.5$ (left panels) or $\Delta_a = 1.5$ and $\Delta_b = 0.5$ (right panels).

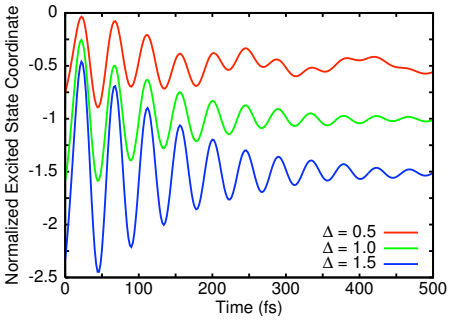

Figure 4.7: Expectation value of the excited-state coordinate of monomer a, corresponding to the model with equal displacements $\Delta_a = \Delta_b = \Delta$ =0.5 (red), 1.0 (blue), and 1.5 (black).

there once again can be seen a fast oscillation ($\sim \omega_{vib}$) that survives for about 200 fs in the site population dynamics. This fast oscillation does not appear in coherence 1–2.

The excited-state coordinate expectation value, $\langle Q_a \rangle$, is shown in Fig. 4.7. In all cases, it has been normalized by a constant representing the overall excited-state population after the interaction with the laser pulse. The oscillatory behavior of this observable is dominated by "vibrational" coherence. The amplitude of the oscillations (or, of the vibrational motion) increases with the coordinate displacement value, Δ. This is particularly noticeable when $\Delta = 0.5$, in which case the electronic coherence is so dominant that it is clearly resolved as a slow oscillation of the coordinate.

4.2 Bath-induced correlation effects on photoinduced dynamics

To illustrate the influence of the bath-induced correlations on the dynamics of the vibronic dimer, the chromophores are now assumed to be bilinearly coupled

to two partially correlated baths (c.f. §2.3.2), where $-1 \leq \gamma \leq 1$. Initially, the dimer is assumed to be in its ground electronic state and in vibrational thermal equilibrium, Eq. (2.65). Because of the interesting dynamics that arise with the inclusion of a large asymmetry, two cases will be considered for the coordinate displacements: a symmetric dimer ($\Delta_a = \Delta_b = 1.5$) and an asymmetric dimer ($\Delta_a = 1.5$ and $\Delta_b = 0.5$). As before, a moderate vibrational dissipation, $\eta = 0.2$, is assumed and the reservoir cutoff frequency, $\omega_c = 600$ cm^{-1}, is on the order of the system-mode vibrational frequency. To emphasize coherent effects, the temperature is chosen to be $T = 4.5$ K.

Fig. 4.8 shows the coordinate expectation values, $\langle Q_+(t)\rangle$ (panel (a)) and $\langle Q_-(t)\rangle$ (panel (b)), for the symmetric dimer ($\Delta = 1.5$) coupled to correlated ($\gamma = 1$, green lines), uncorrelated ($\gamma = 0$, red lines), and anticorrelated ($\gamma = -1$, blue lines) baths. Consistent with the theoretical analysis in Ref. [55], $\langle Q_-(t)\rangle$ for a correlated bath and $\langle Q_+(t)\rangle$ for an anticorrelated bath exhibit no damping. On the other hand, the Q_+ and Q_- subspaces are subjected to vibrational relaxation in the reversed case, as shown.

Notice that $\langle Q_+(t)\rangle$ in the case of anticorrelated baths (Fig. 4.8a, blue line) exhibits undamped harmonic oscillations with a period of 44.5 fs. These oscillations are modulated by a longer beating with a period of about 187 fs (~ 178 cm^{-1}). This is the so-called energy gap beating ($E_b - E_a = 175$ cm^{-1}) [98–100]. Likewise, $\langle Q_-(t)\rangle$ for a correlated bath (Fig. 4.8b, green line) exhibits fast oscillations with the vibrational period of 44.5 fs, superimposed on which are slower, energy-gap beatings with a period of ~ 187 fs.

On the other hand, the Q_+ subspace for a correlated bath and the Q_- subspace for an uncorrelated bath exhibit bath-induced relaxation; Thus the green line in Fig. 4.8a and the blue line in Fig. 4.8b decay. This behavior is similar to the case of an uncorrelated bath (panels (a) and (b), red lines), since

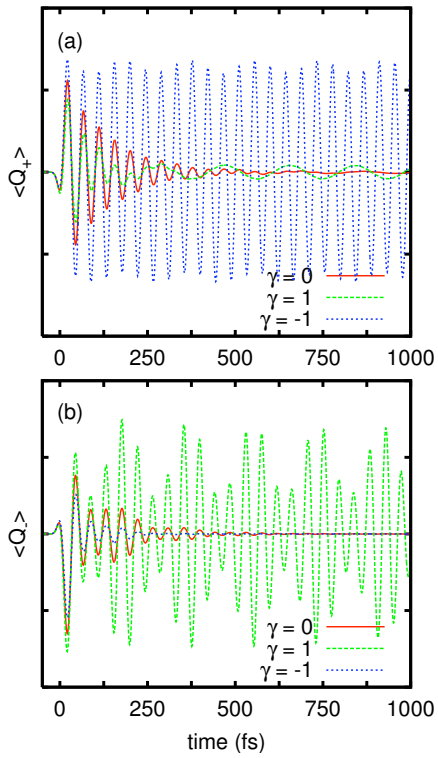

Figure 4.8: Expectation values of the (a) symmetric and (b) antisymmetric coordinate for the symmetric ($\Delta_a = \Delta_b = 1.5$) dimer coupled to baths with uncorrelated ($\gamma = 0$, red, solid lines), correlated ($\gamma = 1$, green, dashed lines), and anticorrelated ($\gamma = -1$, blue, dotted lines) fluctuations.

an uncorrelated bath induces relaxation in both the Q_+ and Q_- subspaces. All of these curves exhibit fast damped vibrational oscillations with a period of 44.5 fs, on which the energy-gap beatings are superimposed.

Fig. 4.9 shows the coordinate expectation values $\langle Q_+(t)\rangle$ (panel (a)) and $\langle Q_-(t)\rangle$ (panel (b)) for the asymmetric dimer ($\Delta_a = 1.5$ and $\Delta_b = 0.5$). Qualitatively, evolutions of $\langle Q_+(t)\rangle$ and $\langle Q_-(t)\rangle$ in Figs. 4.8 and 4.9 are markedly similar. However, notice that $\langle Q_-(t)\rangle$ for a correlated bath (Fig. 4.9b, green line) exhibits certain incomplete bath-induced relaxations, which is weakly damped compared to $\langle Q_+(t)\rangle$ for a correlated bath (Fig. 4.9a, green line) and $\langle Q^a_-(t)\rangle$ for an anticorrelated bath (panel (b), blue line). Thus, it can be said that the Q_- (Q_+) subspace is weakly affected by the correlated (anticorrelated) bath, even for asymmetric dimers. Furthermore, noting that these cases do not completely relax within 1 ps, it can be inferred that a small fraction of the decoherence-free subspaces is mixed with the coherence-free subspaces in the case of fully correlated or anticorrelated baths.

Fig. 4.10 shows the dynamics of the populations of the system density matrix, $\rho_{ii}(t)$, for the first six eigenstates $|\psi_i\rangle$ ($i = 1, \ldots, 6$) of the symmetric dimer. Results for an uncorrelated bath are shown in panel (a). The bath ensures that the dimer density matrix eventually relaxes to the equilibrium Boltzmann distribution in the singly excited excitonic state. For the chosen dimer parameters, the lowest eigenenergy $E_1 \gg k_B T$ (as is usual for optically-excited vibrations). Therefore, only the lowest ($i = 1$) state of the equilibrium distribution is predominantly populated. Indeed, $\rho_{ii}(t)$ for $i = 3 - 6$ relax to zero within about 250 fs (for the dimer and pulse parameters chosen, the near-degenerate pairs of states ($\alpha = 3, 4$ and $5, 6$) are almost equally populated initially). Relaxation of $\rho_{11}(t)$ and $\rho_{22}(t)$ is much slower; this effect is discussed in detail below.

Correlated and anticorrelated baths do not describe a proper relaxation of

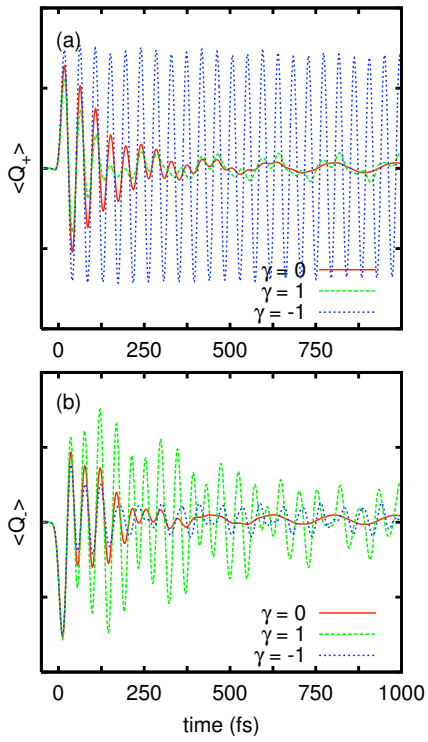

Figure 4.9: Symmetric (a) and antisymmetric (b) coordinate expectation values for the asymmetric ($\Delta_a = 1.5, \Delta_b = 0.5$) dimer for three different baths: uncorrelated ($\gamma = 0$, red, solid lines), correlated ($\gamma = 1$, green, dashed lines), and anticorrelated ($\gamma = -1$, blue, dotted lines).

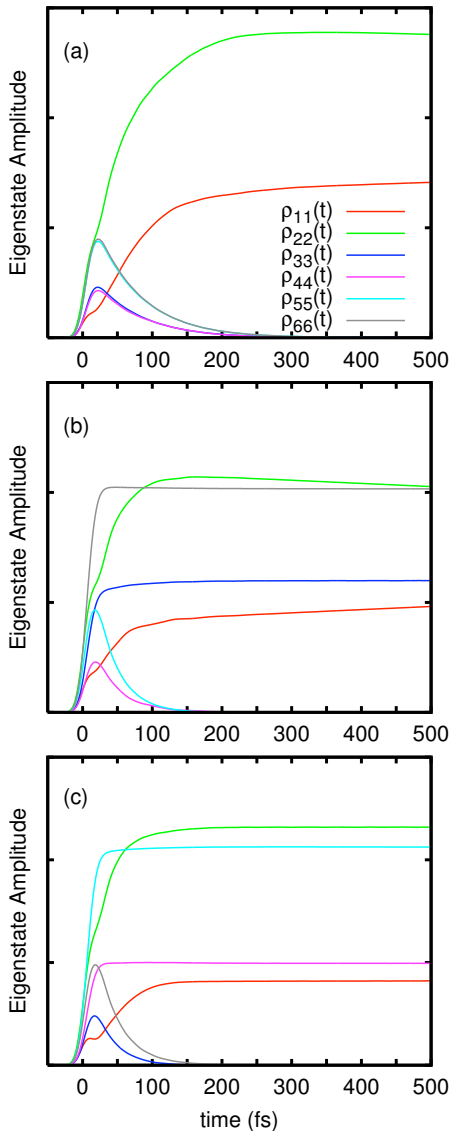

Figure 4.10: Time evolution of the density matrix populations $\rho_{ii}(t)$ for the lowest six eigenstates ($i = 1, ...6$) for the symmetric dimer ($\Delta_a = \Delta_b = 1.5$) coupled to (a) an uncorrelated, (b) a correlated, and (c) an anticorrelated bath.

the dimer to equilibrium, due to the presence of decoherence-free subspaces. Therefore $\rho_{33}(t)$ and $\rho_{66}(t)$ for a fully correlated bath (Fig. 4.10b), as well as $\rho_{44}(t)$ and $\rho_{55}(t)$ for a fully anticorrelated bath (Fig. 4.10c), do not tend to zero. Interestingly, the eigenstates which relax due to the coupling to a correlated bath, do not relax due to the coupling to an anticorrelated bath, and vice versa. This indicates that the eigenstates $|\psi_3\rangle$ and $|\psi_6\rangle$ belong predominantly to the Q_- subspace, while states $|\psi_4\rangle$ and $|\psi_5\rangle$ belong predominantly to the Q_+ subspace.

Fig. 4.11 depicts the evolutions of the coherences, $\rho_{ij}(t)$ for $i \neq j$, involving the lowest three eigenstates ($i = 1, 2, 3$). As expected, all $\rho_{ij}(t)$ oscillate at the frequencies $\omega_{ij} = E_i - E_j$. Since the electronic coupling, J_{ab}, is relatively small, $\omega_{21} \approx E_b - E_a$, $\omega_{31} \approx \omega_{vib}$, and $\omega_{32} \approx \omega_{vib} - (E_b - E_a)$. Hence the oscillation periods for $\rho_{12}(t)$, $\rho_{31}(t)$, and $\rho_{32}(t)$ are 187, 44.5, and 58.6 fs, respectively. An uncorrelated bath induces a rapid decay of all coherences, except $\rho_{12}(t)$ (Fig. 4.11a), which relaxes on a much longer timescale. This will be discussed in greater detail below. Qualitatively similar behaviors are exhibited for $\rho_{ij}(t)$ in the case of a fully anticorrelated bath (panel c). On the other hand, a fully correlated bath is not efficient in damping these coherences (panel b). Evolutions of $\rho_{ij}(t)$ for an asymmetric dimer is qualitatively similar (not shown).

Let us now reinspect Fig. 4.10a, which depicts the evolution of $\rho_{ii}(t)$ in the case of an uncorrelated bath. Clearly, the $\rho_{ii}(t)$ for $i = 3, \ldots, 6$ relax to zero within ~ 250 fs. However, relaxation of $\rho_{11}(t)$ and $\rho_{22}(t)$ is much slower. This behavior is rather general and reflects the following physics: If $J_{ab} = 0$, the two monomers are independent, so that the distributions in the Q_a and Q_b subspaces (or in the Q_+ and Q_- subspaces) relax independently to equilibrium. The corresponding relaxation rate, ν, is determined by the coupling of each monomer to its vibrational bath. If we now allow for $J_{ab} \ll |E_2 - E_1| \neq 0$,

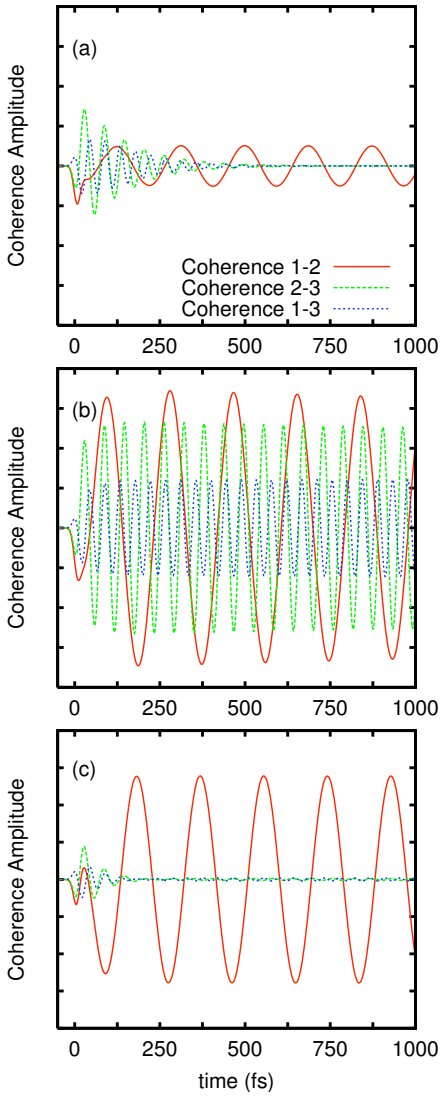

Figure 4.11: Time evolution of the density matrix coherences $\rho_{ij}(t)$ involving the lowest three eigenstates of the symmetric dimer ($\Delta_a = \Delta_b = 1.5$) coupled to (a) an uncorrelated, (b) a correlated, and (c) an anticorrelated bath; with $\rho_{12}(t)$ shown by red, solid lines, $\rho_{23}(t)$ by green, dashed lines, and $\rho_{13}(t)$ by blue, dotted lines.

then each monomer first reaches its local equilibrium in the relevant subspace at the same rate ν. Subsequent relaxation to global equilibrium will take place at the rate $\nu_{J_{ab}} \sim J(\omega_{21})\sin^2(2\theta)$, where $J(\omega)$ is the bath spectral density (Eq. 2.54) and $2\theta = \arcsin(2J_{ab}/\sqrt{(\omega_{21})^2 + 4J_{ab}^2})$ is the (double) mixing angle for the effective two-level system $|\psi_1\rangle$, $|\psi_2\rangle$ (see, e.g., Ref. [59]). In fact, $\nu_{J_{ab}}$ is also the rate for the intermonomer energy transfer. Normally, $\nu_{J_{ab}}$ is (much) slower than $\nu \sim J(\omega_{vib})$. Only for dimers with the vertical electronic energies $E_a \approx E_b$, and thus $E_2 \approx E_1$, are these two rates comparable. In the present case, $E_b - E_a = 175$ cm^{-1}, $\sin^2(2\theta) \approx 0.33$, and $\nu_{J_{ab}}/\nu \approx 0.2$. The actual ratio of the rates is even smaller than the one resulting from the above qualitative analysis.

The long-time decays of the density matrix populations $\rho_{11}(t)$ and $\rho_{22}(t)$ are presented in Fig. 4.12. The solid lines depict the same populations as in Fig. 4.10a, but on a longer timescale. The dashed lines, which show the populations calculated for a stronger intermonomer coupling $J_{ab} = -150$ cm^{-1}, exhibit noticeably faster relaxations. Remnants of the slow relaxations with a characteristic timescale of $1/\nu_{J_{ab}}$ are also seen in the upper panels of Figs. 4.8 and 4.9: $\langle Q_+(t)\rangle$ does not decay to zero within ~ 250 fs but rather exhibits low-amplitude damped oscillations on the timescale of ~ 1 ps.

The presence of two relaxation rates, ν and $\nu_{J_{ab}} \ll \nu$, manifests itself vividly in the relaxation of the coherences. Even when the dimer is coupled to an uncorrelated bath, which provides the fastest relaxation rates in both the Q_+ and Q_- subspaces, $\rho_{12}(t)$ decays much slower than all other coherences (Fig. 4.11a). The slow long-time decay of $\rho_{12}(t)$ is shown in Fig. 4.12b. The solid lines correspond to the intermonomer coupling, $J_{ab} = -62$ cm^{-1}, and the dashed lines to the stronger coupling, $J_{ab} = -150$ cm^{-1}. Again, the stronger the coupling, the faster the decay of the coherences. The following qualitative picture is thus

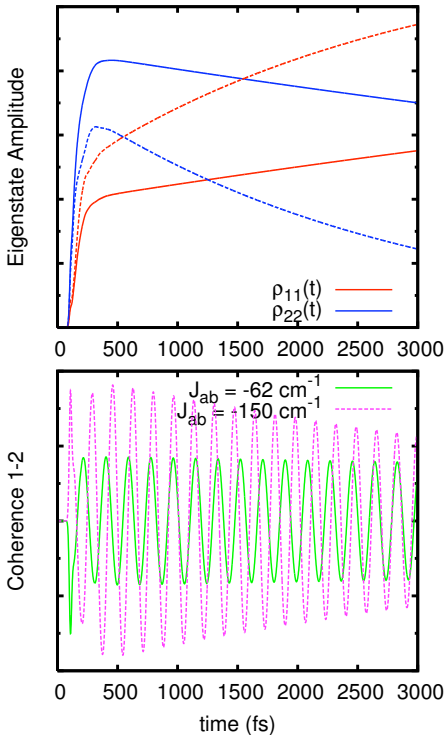

Figure 4.12: Long-time evolution of (a) the density matrix populations $\rho_{11}(t)$ and $\rho_{22}(t)$ and (b) coherences $\rho_{12}(t)$ for the symmetric dimer ($\Delta_a = \Delta_b = \Delta = 1.5$) coupled to an uncorrelated bath. Solid lines correspond to $J_{ab} = -62$ $\mathtt{cm}^{-1}$; dashed lines correspond to $J_{ab} = -150$ $\mathtt{cm}^{-1}$.

emerging: If the dimer is coupled to an uncorrelated bath, it effectively becomes a two-level system after $t \geq 1/\nu$. Only the populations in the two lowest levels ($|\psi_1\rangle$, $|\psi_2\rangle$) as well as the coherence between them ($|\psi_1\rangle\langle\psi_2|$) remain nonzero. Thus, the existence of the long relaxation time $\sim 1/\nu_{J_{ab}}$ may be a source of long-lived populations and coherences in quantum dissipative systems.

Fig. 4.13 illustrates the effect of partial bath correlations ($\gamma = 1/\sqrt{2}$, panel (a)) and anticorrelations ($\gamma = -1/\sqrt{2}$, panel (b)) on the relaxation of the density matrix populations $\rho_{ii}(t)$ ($i = 1, \ldots, 6$). The evolution of $\rho_{44}(t)$ and $\rho_{55}(t)$ for a fully correlated bath, as well as the evolution of $\rho_{33}(t)$ and $\rho_{66}(t)$ for a fully anticorrelated bath, are almost unaffected by the presence of $\gamma \neq 0$ (compare Fig.4.10b with 4.13a, and Fig. 4.10c with 4.13b). These are the components of the density matrix that exhibit vibrational relaxation for a fully correlated and a fully anticorrelated bath, respectively. On the other hand, $\rho_{33}(t)$ and $\rho_{66}(t)$ for a fully correlated bath, as well as $\rho_{44}(t)$ and $\rho_{55}(t)$ for a fully anticorrelated bath (which do not relax for a fully correlated (Fig. 4.10b) or anticorrelated (Fig. 4.10c) bath, respectively) now exhibit bath induced relaxations with the rates $\nu_\gamma \sim \nu(1 - |\gamma|)$. Due to the reasons described above, the relaxations of $\rho_{11}(t)$ and $\rho_{22}(t)$ are much slower.

Fig. 4.14 shows the influence of partial bath correlations ($\gamma = 1/\sqrt{2}$, panel (a)) and anticorrelations ($\gamma = -1/\sqrt{2}$, panel (b)) on the evolution of the density matrix coherences $\rho_{ij}(t)$. Two aspects are to be emphasized here: First, $\rho_{23}(t)$ and $\rho_{31}(t)$, which do not decay for fully correlated bath (Fig. 4.11b), now relax at the rate $\nu_\gamma \sim \nu(1 - |\gamma|)$. Second, the coherence between the two lowest eigenstates, $\rho_{12}(t)$, now undergoes additional relaxation on the timescale $1/\nu_\gamma$ (note the difference in the maximum amplitude of $\rho_{12}(t)$ in Figs. 4.11 and 4.14). Subsequently, they slowly decay at the rate $\sim \nu_{J_{ab}}$ (not shown).

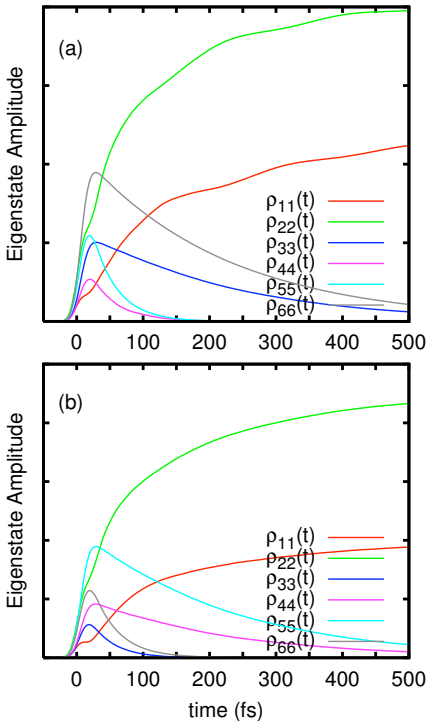

Figure 4.13: Time evolution of the density matrix populations $\rho_{ii}(t)$ for the lowest six eigenstates ($i = 1, ...6$) of the symmetric dimer ($\Delta_a = \Delta_b = \Delta = 1.5$) coupled to a partially (a) correlated ($\gamma = 1/\sqrt{2}$) and a partially (b) anticorrelated ($\gamma = -1/\sqrt{2}$) bath.

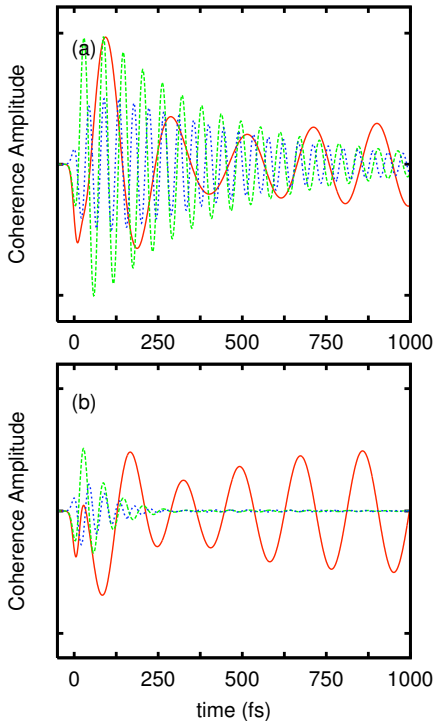

Figure 4.14: Time evolution of the density matrix coherences $\rho_{ij}(t)$ involving the lowest three eigenstates of a symmetric dimer ($\Delta_a = \Delta_b = 1.5$) coupled to a partially (a) correlated ($\gamma = 1/\sqrt{2}$) and a partially (b) anticorrelated ($\gamma = -1/\sqrt{2}$) bath; $\rho_{12}(t)$ is shown by red, solid lines, $\rho_{23}(t)$ by green, dashed lines, and $\rho_{13}(t)$ by blue, dotted lines.

Chapter 5

Time-resolved spectroscopy of vibronic dimers

5.1 2D photon echo spectra

In the previous Chapter, we have demonstrated how different coherences exhibit themselves in system observables. A much more challenging task is to relate coherent dynamics to measurable signals. It is often assumed that the system coherences are represented by cross peaks (CP) of the 2D PE signals. This belief is based on the response-function analysis of an excitonic dimer, where, in the absence of relaxation and in the impulsive limit, the CP intensity depends on the population time T as $e^{\pm i(E_1-E_2)T}$, i.e., it evolves exactly as a coherence between a pair of excitonic-dimer eigenstates with energies E_1 and E_2.

The same response-function analysis (in the zero-temperature limit, with no dissipative processes, in the limit of instantaneous excitation) can be applied to a vibronic dimer, when both the ground and the excited electronic states have multilevel vibrational structure. The oscillating T-dependence of a cross peak at

an absorption frequency $\omega_\tau = E_e - E_0$ and an emission frequency $\omega_t = E_{e'} - E_g$ (E_e is the energy of the excited state resonant with the absorption frequency ω_τ, E_0 denotes the energy of the initial state, and $E_{e'}$ and E_g can pertain to any vibrational levels in the excited- and ground-state manifold, respectively) is determined by

$$\mathrm{CP}\left(\omega_\tau = \omega_{e0}, \omega_t = \omega_{e'g}\right) \sim \sum_{e',g} \mu_{0e}\mu_{eg}\mu_{ge'}\mu_{e'0}\left(e^{i\omega_{ee'}T} + e^{i\omega_{g0}T}\right), \tag{5.1}$$

where $\omega_{ee'} = E_{e'} - E_e$, $\omega_{g0} = E_g - E_0$ and $\mu_{\mu\nu}$ denote the dipole transition strengths between a pair of eigenstates μ and ν, and the initial state E_0 corresponds to the ground vibrational state. For each CP at certain ω_τ and ω_t, the oscillative behavior with population time T is determined by the frequencies $\omega_{ee'}$ and ω_{g0} related by $\omega_{ee'} + \omega_{g0} = \omega_\tau - \omega_t$.

Eq. 5.1, as well as the computed signals that follow, correspond to the rephasing part of the signal and do not include the ESA contribution. The rephasing part of 2D PE is an experimentally measurable and well-defined observable, as described in Section 2.4, which corresponds to positive coherence time, i.e. $\tau > 0$ in the Fourier transform in Eq. 2.68. The 2D PE signals discussed in this Chapter have been calculated with the same laser pulses as the one employed in the previous Chapter (reduced carrier frequency $\omega = 900$ $\mathtt{cm}^{-1}$ and 30 fs duration at FWHM), and optical dephasing equal to 30 $\mathtt{cm}^{-1}$. Inhomogeneous broadening is neglected here because it was previously shown not to significantly affect peak dynamics with population time[46].

As can be recognized from the employed model Hamiltonian (Eq. 2.43), the ESA contribution is not taken into account in the present work. The reason for this simplification is that the vibronic effects addressed here are most pronounced for the stimulated-emission (SE) contribution. Therefore, the 2D PE profiles shown in Fig. 5.1 are purely model observables. Nevertheless, the data

provide valuable information about how the 2D PE signals of a dimer are affected by the variation of the excited-state displacement. While different displacement values only slightly affect the eigenstate structure in the present model, they significantly influence the dipole strengths (via Franck-Condon factors, refer to Appendix A.2 for details) of individual transitions.

Fig. 5.1 displays 2D PE signals at $T = 0$ obtained with the excited-state displacements $\Delta = 0.5, 1.0, 1.5$, and 2.0. The location of the peaks can be rationalized using the expressions $\omega_\tau = E_e - E_0$ and $\omega_t = E_{e'} - E_g$, the eigenvalues listed in Table 4.1, and the fact that the ground-state vibrational manifold is equidistant and obeys $E_g = n\omega_{vib}$, $n = 0, 1, 2, \ldots$. The signal visualizes the eigenstate structure discussed in the previous Chapter (the small peaks separations due to the splitting via the interstate coupling, and the larger separations on the order of the vibrational frequency), and provides a very clear picture of how increasingly higher vibronic states get excited with the increase of the coordinate displacement Δ by identical laser pulses. The resulting 2D profiles of the vibronic dimer are similar to the previously reported signals of the vibronic electron-transfer model, and we refer the interested reader to Ref. [64] for a detailed discussion of the fine structure of the 2D profiles.

The intensity of the peaks is determined by the dipole strengths of the corresponding transitions (as well as Franck-Condon factors of the involved vibrational states) and are slightly modified by the finite pulse durations. Notice that as the displacement increases, the peaks corresponding to eigenstates 3-6 (around $\omega_t = \omega_\tau = 950$ $\mathtt{cm}^{-1}$) become brighter. This is due to the increase in Franck-Condon factors involving these higher states when the coordinate displacement is large, and thus more efficient population transfer to these states.

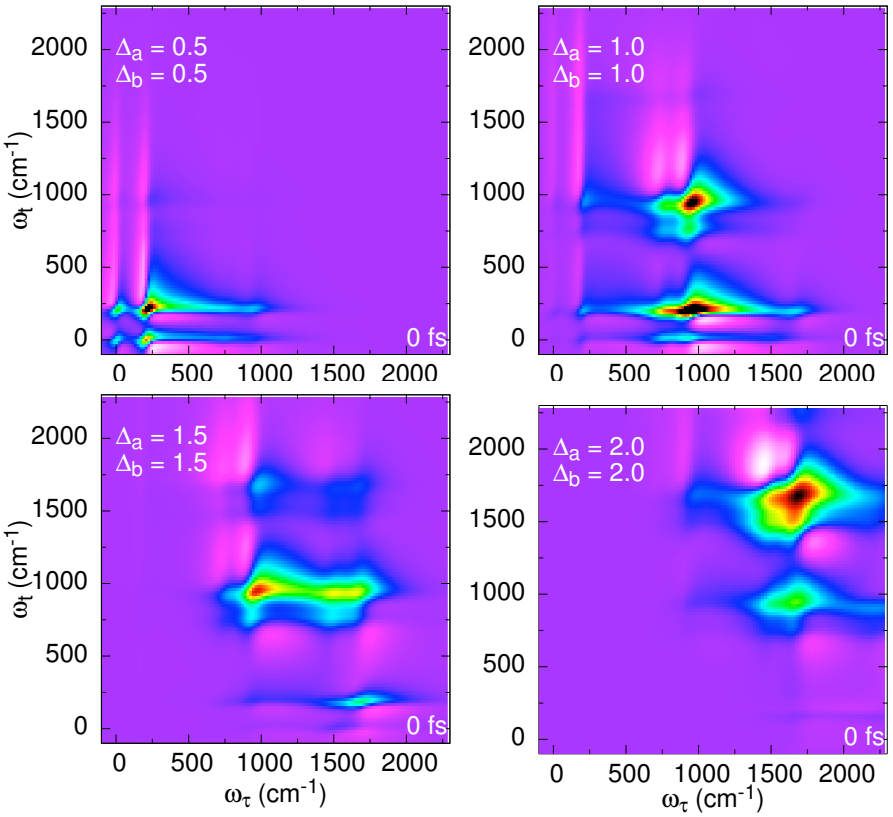

Figure 5.1: 2D PE spectra at population time $T = 0$ fs for the symmetric cases Δ =0 .5 (top-left panel), $\Delta = 1.0$ (top-right), $\Delta = 1.5$ (bottom-left panel), and Δ =2 .0 (bottom-right). Arcsinh scaling is used to highlight weaker peaks in the spectral profiles.

5.2 Peak evolution

Now, we turn to the CP dynamics with population time and study to what extent it can be related to the evolution of the system coherences. For each cross peak, only ω_τ corresponds to one particular, energetically well-defined transition from the initial state to a certain excited state with the energy $E_0 + \omega_\tau$. As for ω_t, several transitions satisfying $E_{e'} - E_g = \omega_t$ may contribute. According to Eq. (5.1), three distinct contributions may arise; Fig. 5.2 shows the relevant energy level diagram illustrating these contributions. The red arrow shows the transition with a well-defined absorption frequency, $\omega_\tau = E_e - E_0$. The first contribution (i) corresponds to the blue lines, for which $\omega_t = \omega_{e'0}$, such that $\omega_t = \omega_{e'0}$ and the CP oscillating component has the single frequency $\omega_{ee'} = \omega_\tau - \omega_t$ (denoted by the blue, vertical line). The second contribution (ii) corresponds to the green lines in Fig. 5.2, for which $\omega_t = \omega_{eg}$, and the CP oscillating component has the single frequency $\omega_{g0} = \omega_\tau - \omega_t$ (denoted by the green, vertical line). The final contribution (iii) can be manifested by several scenarios, all of which have $\omega_t = \omega_{e'g}$; two examples are shown by the purple lines in Fig. 5.2. In this situation, $\omega_{g0} \neq 0$ and $\omega_{ee'} \neq 0$ (Fig. 5.2 purple, vertical lines), which would lead to a superposition of CP oscillations with frequencies $\omega_{ee'}$ and ω_{g0}, which are related by $\omega_{ee'} + \omega_{g0} = \omega_\tau - \omega_t$.

The contributions (ii) and (iii) involve vibrational levels of the electronic ground state, i.e., they may arise for any system with discrete vibrational structure in the initial electronic state. One of them may coexist together with a contribution of type (i), if the eigenstate structure is such that $\omega_{ee'} \sim \omega_{g0}$ can be fulfilled. For a simultaneous realization of (ii) and (iii), the presence of the eigenstates with $\omega_{ee'} \sim \omega_{gg'}$ is required. Note that case (ii) is special: The transition associated with the emission frequency ω_t (green line in Fig. 5.2) occurs from a state $|e\rangle$ and is well defined by the absorption frequency. Therefore, it is

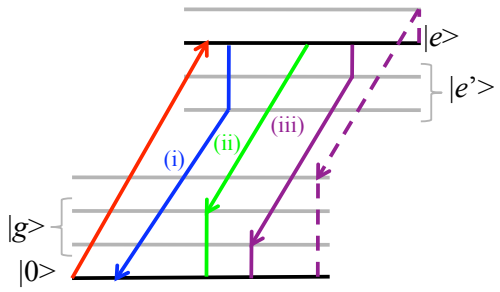

Figure 5.2: Transitions contributing to a cross peak at $\omega_\tau = E_e - E_0$ (red) and $\omega_t = E_{e'} - E_0$ (blue), $\omega_t = E_e - E_g$ (green), and $\omega_t = E_{e'} - E_{g'}$

realized only for those CPs with $\omega_\tau > \omega_t$ (in our notation, CPs below diagonal) and located at $\omega_\tau = \omega_t + \omega_{g0}$.

If the oscillatory behavior of a CP with population time T shows only one frequency corresponding to the difference $\omega_\tau - \omega_t$, then for CPs above the diagonal contributions of type (i) dominate. This is most probable for those CPs where the transition dipoles μ_{e0} are large, so that the diagonal peaks at given ω_τ and ω_t are most intense. The weaker peaks at the diagonal provide ω_τ and ω_t for which contributions of type (iii) may become comparable or larger then those of type (i), and the observation of multiple frequencies in the CP evolution is most probable. For certain CPs below the diagonal, contributions of type (ii) may be present as well, but it delivers a single-frequency oscillative component corresponding to a vibrational energy splitting in the ground state manifold, which is hard to distinguish from the components of type (i) (both frequencies should approximately equal $\omega_\tau - \omega_t$)

In the following, we first address the CPs where ω_t results in an intense diagonal peak at $\omega_t = \omega_\tau$, when contribution of type (i) will most likely dominate, and a single-frequency evolution of CPs is expected. For $\Delta = 0.5$, we study the lower diagonal peak at $\omega_\tau = 0$ $\mathtt{cm}^{-1}$, $\omega_t = 200$ $\mathtt{cm}^{-1}$, and its above-

diagonal mirror CP; for $\Delta = 1.0$, we take the above- and below-diagonal peaks at 190 $\mathtt{cm}^{-1}$, 940 $\mathtt{cm}^{-1}$; and for $\Delta = 1.5$, the peaks at 930 $\mathtt{cm}^{-1}$, 1500 $\mathtt{cm}^{-1}$ are studied. This discussion extends then to cases when multiple-frequency behavior in CP dynamics is observed. For the dimer model considered here, due to an equidistant vibrational energy ladder in the ground-state manifold, $\omega_{g0} = E_g - E_0 = n\omega_{\mathtt{vib}}$. Therefore, case (ii) can be realized only for CPs with $\omega_\tau = \omega_t + n\omega_{\mathtt{vib}}$, and in case (iii), a superposition of oscillations with frequencies $n\omega_{\mathtt{vib}}$ and $|n\omega_{\mathtt{vib}} - (\omega_\tau - \omega_t)|$ is expected. A time step of 2 fs was used in the calculations in order to resolve all fast and slow oscillations in peak dynamics.

For $\Delta = 0.5$, the brightest peaks are located in the bottom-left corner of Fig. 5.1 (top-left panel), and the diagonal peaks correspond to the transitions to the two lowest excited states $E_1 = 0$ and $E_2 = 206$ cm^{-1} (Table 4.1). The dipole moments of these two transitions are of the same order and the strongest for the system (Table **??**). We consider the CP below the diagonal at $\omega_\tau = 206$ $\mathtt{cm}^{-1}$, $\omega_t = 0$ $\mathtt{cm}^{-1}$ and its mirror counterpart above the diagonal at $\omega_\tau = 0$ $\mathtt{cm}^{-1}$, $\omega_t = 206$ $\mathtt{cm}^{-1}$. The evolution of their intensity with population time is shown in Fig. 5.3. When $\omega_\tau = 0$ $\mathtt{cm}^{-1}$, $\omega_t = 206$ cm^{-1} (blue, dashed line in Fig. 5.3), absorption occurs to the lowest excited state with the energy E_1 ($\omega_\tau = E_1 - E_0 =$ 0 $\mathtt{cm}^{-1}$). At the same time, ω_t corresponds to several transitions simultaneously: the transition from the second excited state with energy $E_2 = 206$ cm^{-1} to the ground state ($E_0 = 0$ $\mathtt{cm}^{-1}$), the transition from $E_6 = 956$ $\mathtt{cm}^{-1}$ to the vibrationally excited ground state with energy equal to one vibrational quanta ($E_g = \omega_{\mathrm{vib}} = 750$ cm^{-1}), as well all other transitions of type (iii). However, only the single frequency $\omega_t - \omega_\tau = 206$ $\mathtt{cm}^{-1}$ is resolved in Fig. 5.3. The type (i) contribution dominates, since the dipole transition to the second excited state is much stronger than to the higher-lying states ($\mu_{20} \gg \mu_{n0}$, $n > 2$, cf. Fig. 5.1 and Table 5.1), and the transitions involving excited vibrational states of the

ground state are weak.

Table 5.1: Dipole moments μ_{0i} between the lowest vibrational ground electronic state and the first twelve (i) excited eigenstates, for each value of the coordinate displacement in the symmetric case, i.e. $\Delta = \Delta_a = \Delta_b$.

Δ	0.5	1.0	1.5
$\mu_{0,1}$	-5.29	-4.15	2.76
$\mu_{0,2}$	5.23	4.71	-3.74
$\mu_{0,3}$	-1.00	1.69	1.96
$\mu_{0,4}$	0.52	-1.46	1.91
$\mu_{0,5}$	1.76	-2.65	2.70
$\mu_{0,6}$	-1.28	2.28	2.72
$\mu_{0,7}$	0.08	0.36	1.40
$\mu_{0,8}$	-0.19	0.40	0.59
$\mu_{0,9}$	-0.20	-0.83	1.03
$\mu_{0,10}$	-0.26	-1.33	0.34
$\mu_{0,11}$	-0.47	-0.92	1.13
$\mu_{0,12}$	0.21	0.86	2.68

The same single frequency is characteristic for the dynamics of the lower CP at $\omega_\tau = 206$ cm^{-1}, $\omega_t = 0$ $\mathtt{cm}^{-1}$ (red, solid line in Fig. 5.3). In this case, the absorption process is to the second excited state E_2, and the contribution corresponding to the emission from $E_1 = 0$ $\mathtt{cm}^{-1}$ to $E_0 = 0$ $\mathtt{cm}^{-1}$ dominates the CP oscillatory dynamics. The type (ii) contribution cannot arise for the CP since $\omega_\tau - \omega_t$ does not correspond to any $\omega_{g0} = n\omega_{\mathtt{vib}}$.

For $\Delta = 1$, the most intense diagonal peak corresponds to transitions to the closely lying levels $E_5 = 936$ $\mathtt{cm}^{-1}$ and $E_6 = 940$ $\mathtt{cm}^{-1}$. For our analysis, we follow the most intense cross peak below the diagonal at $\omega_\tau = 940$ cm^{-1}, $\omega_t = 190$ cm^{-1}, as well as its mirror counterpart at $\omega_\tau = 190$ cm^{-1}, $\omega_t = 940$ cm^{-1}, which is plotted with population time in Fig. 5.4. In this case, the difference between ω_τ and ω_t is on the order of one vibrational quantum and the contribution of type (ii) may occur for the lower CP. The single-frequency beating with $|\omega_\tau - \omega_t| = \omega_{\mathtt{vib}} = 750$ $\mathtt{cm}^{-1}$ dominates the oscillation dynamics

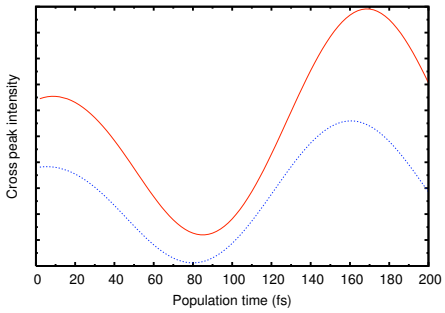

Figure 5.3: The amplitude of the most intense crosspeak of the 2D PE profile corresponding to $\Delta = 0.5$ as a function of population time, $\omega_\tau = 206$ $\mathtt{cm}^{-1}$, $\omega_t = 0$ $\mathtt{cm}^{-1}$ (red, solid line) and the mirror counterpart with $\omega_\tau = 0$ $\mathtt{cm}^{-1}$, $\omega_t = 206$ $\mathtt{cm}^{-1}$ (blue, dashed line).

of both CPs shown in Fig. 5.4. For the upper CP, one can thus conclude that the type (i) contribution dominates. Here, the emission frequency matches all transitions from $E_{5,6} + n\omega_{\mathtt{vib}}$ to the ground-state levels with $n\omega_{\mathtt{vib}}$, but only the case $n = 0$ is observed. For the lower CP, one cannot exclude the type (ii) contribution, since it is nearly indistinguishable from the type (i) contribution. The emission at $\omega_t = 190$ $\mathtt{cm}^{-1}$ may correspond either to the transitions from the levels with energy of about E_2 to the initial state E_0 (type (i)), or to the transitions from $E_{5,6}$ to the ground-state levels with $\omega_{\mathtt{vib}}$ (type (ii)). The dynamics of both CPs in Fig. 5.4 are similar to each other, with the exception of their relative intensity. This difference arises, since the absorption frequency of the lower CP (red, solid line in Fig. 5.4) corresponds to transitions from the initial state ($E_0 = 0$) to the excited states with $E_5 \approx E_6$ (see Table 4.1), which are resonant with the excitation pulse, while the absorption frequency of the upper CP corresponds to the off-resonant E_2 level.

The most intense CP For $\Delta = 1.5$, is located around $\omega_t = 930$ $\mathtt{cm}^{-1}$ and $\omega_\tau = 1500$ $\mathtt{cm}^{-1}$. The dynamics of this CP, as well as its mirror counterpart, is shown in Fig. 5.5. In contrast to Figs. 5.3 and 5.4, the oscillative character

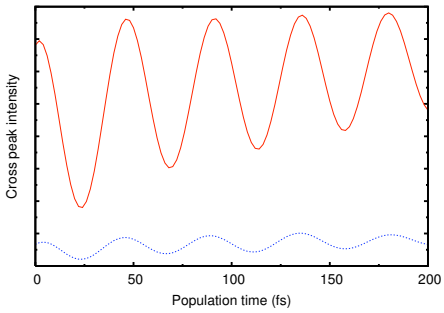

Figure 5.4: The amplitude of the most intense crosspeak of the 2D PE profile corresponding to $\Delta = 1.0$ as a function of population time, $\omega_\tau = 940$ $\mathtt{cm}^{-1}$, $\omega_t = 190$ $\mathtt{cm}^{-1}$ (red, solid line) and the mirror counterpart with $\omega_\tau = 190$ $\mathtt{cm}^{-1}$, $\omega_t = 940$ $\mathtt{cm}^{-1}$ (blue, dashed line).

differs significantly for the two mirror peaks considered. For the lower peak, $\omega_\tau = 1500$ $\mathtt{cm}^{-1}$, $\omega_t = 930$ $\mathtt{cm}^{-1}$, the absorption goes to the three states of a very similar energy $E_7 \approx E_8 \approx E_9$. For the emission at 930 $\mathtt{cm}^{-1}$, we may expect, in general, all possible transitions from $E_{5,6} + n\omega_{\rm vib}$ to the ground-state levels of $n\omega_{\rm vib}$. Since only the single-frequency component of 1500 $\mathtt{cm}^{-1}$ − 930 $\mathtt{cm}^{-1}$ = 570 $\mathtt{cm}^{-1}$ is well resolved in the CP dynamics, we conclude that dominating contribution is of type (i). The upper peak, where excitation occurs to the levels $E_5 \approx E_6$, and the emission frequency must match 1500 $\mathtt{cm}^{-1}$, i.e., transitions from $E_{7,8,9} + n\omega_{\rm vib}$ to $E_g = n\omega_{\rm vib}$, however, shows a different, higher frequency, as compared to the 570 $\mathtt{cm}^{-1}$ oscillation of the lower CP. This can be understood in terms of the type (iii) contribution that leads to a superposition of oscillations with frequencies $n\omega_{\rm vib}$ and $n\omega_{\rm vib} + 570$ $\mathtt{cm}^{-1}$. Most likely, the stimulated-emission processes of both types are reflected in the dynamics of the upper CP: transitions from $E_{7,8,9}$ to E_0 (type (i)) and transitions from $E_{7,8,9} + \omega_{\rm vib}$ to $E_g = \omega_{\rm vib}$ (type (iii) for $n = 1$). The observation of multiple frequencies in the dynamics of the upper cross peak only can be related (using Eq. 5.1) to the fact that the dipole strength of the transitions to $E_{5,6}$ are much

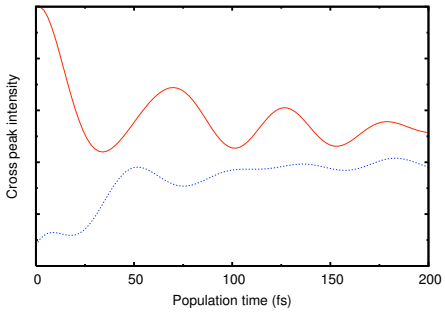

Figure 5.5: The amplitude of the most intense crosspeak of the 2D PE profile corresponding to $\Delta = 1.5$ as a function of population time, $\omega_\tau = 1500$ $\mathtt{cm}^{-1}$, $\omega_t = 930$ $\mathtt{cm}^{-1}$ (red, solid line) and the mirror counterpart with $\omega_\tau = 930$ $\mathtt{cm}^{-1}$, $\omega_t = 1500$ $\mathtt{cm}^{-1}$ (blue, dashed line).

higher than those of the transitions to $E_{7,8,9}$ (Table 5.1), which is also reflected in the relative intensity of the corresponding diagonal peaks.

To pursue the idea that less intense transitions may lead to CPs with multiple frequencies in their CP dynamics, we consider additional CPs of the 2D PE signals obtained for the dimer with the excited-state displacements $\Delta = 1$. Fig. 5.6 shows CP at $\omega_\tau = 940$ cm^{-1}, $\omega_t = 750$ cm^{-1} (red, solid line) as well as its mirror counterpart at $\omega_\tau = 750$ cm^{-1}, $\omega_t = 940$ cm^{-1} (blue, dashed line). Along with the type (i) frequency of 940 $\mathtt{cm}^{-1}$ − 750 $\mathtt{cm}^{-1}$ = 190 cm^{-1}, the intensities of both peaks show higher-frequency modulations, which arise due to non-negligible contributions from transitions involving vibrationally excited states of the ground-state manifold, $\omega_{g0} = n\omega_{\rm vib} \neq 0$ in Eq. (5.1). For the lower peak (absorption to the excited states with $E_3 \approx E_4$, red, solid line), the higher frequency component arises due to a superposition of oscillations with $n\omega_{\rm vib}$ and $n\omega_{\rm vib} - 190$ $\mathtt{cm}^{-1}$ (750 $\mathtt{cm}^{-1}$ and 560 $\mathtt{cm}^{-1}$ for $n = 1$), while for the upper peak (absorption to the excited states with $E_5 \approx E_6$, blue, dashed line), the type (iii) contribution results in the additional frequencies $n\omega_{\rm vib}$ and $n\omega_{\rm vib} + 190$ $\mathtt{cm}^{-1}$ (750 $\mathtt{cm}^{-1}$ and 940 $\mathtt{cm}^{-1}$ for $n = 1$).

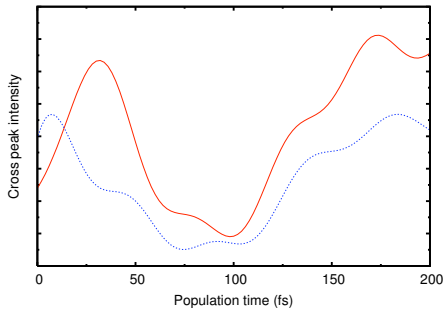

Figure 5.6: The amplitude of a crosspeak of the 2D PE profile corresponding to $\Delta = 1.0$ as a function of population time, $\omega_\tau = 940$ $\mathtt{cm}^{-1}$, $\omega_t = 750$ $\mathtt{cm}^{-1}$ (red, solid line) and the mirror counterpart with $\omega_\tau = 750$ $\mathtt{cm}^{-1}$, $\omega_t = 940$ $\mathtt{cm}^{-1}$ (blue, dashed line).

Cross peak oscillation dynamics with multiple frequencies is observed in another case, for $\Delta = 1.0$. Fig. 5.7 shows the CP at $\omega_\tau = 940$ cm^{-1}, $\omega_t = 0$ $\mathtt{cm}^{-1}$ (red, solid line) and the mirror peak at $\omega_\tau = 0$ $\mathtt{cm}^{-1}$, $\omega_t = 940$ cm^{-1} (blue, dashed line). The high-frequency oscillation can be related to $|\omega_\tau - \omega_t| = 940$ $\mathtt{cm}^{-1}$. The low-frequency modulation of the lower peak can be rationalized as the contribution from $|n\omega_{\mathrm{vib}} - (\omega_\tau - \omega_t)| = 190$ $\mathtt{cm}^{-1}$. As for the low-frequency component of the upper peak, it must arise as an amplitude modulation due to a superposition of high-frequency oscillations with 940 $\mathtt{cm}^{-1}$, 750 $\mathtt{cm}^{-1}$ and $940 + 750 = 1690$ $\mathtt{cm}^{-1}$. An alternative explanation is simply an overlap with neighboring peaks.

Finally we briefly address the issue of coherence transfer, noted in Chapter 4 when considering the system low-frequency coherences ρ_{12} (Fig. 4.4) for $\Delta = 1$ and $\Delta = 1.5$. The CPs corresponding to the transitions involving the levels E_1 and E_2 are those at $\omega_\tau = E_1 = 0$ $\mathtt{cm}^{-1}$, $\omega_t = E_2 \approx 180 - 190$ $\mathtt{cm}^{-1}$ and vice versa; as shown in Fig. 5.8 for $\Delta = 1$. The CP dynamics closely resembles the dynamics of the same CPs for $\Delta = 0.5$ (Fig. 5.3) and, in contrast to system coherences ρ_{12} (Fig. 4.4), no signatures of high-frequency modulations

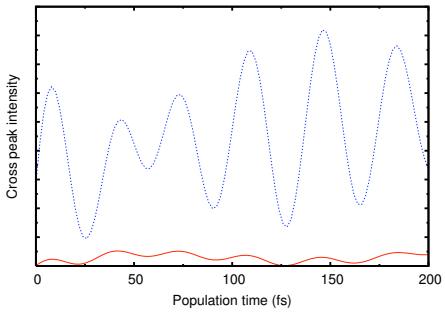

Figure 5.7: The amplitude of a crosspeak of the 2D PE profile corresponding to $\Delta = 1.0$ as a function of population time, $\omega_\tau = 940$ $\mathtt{cm}^{-1}$, $\omega_t = 0$ $\mathtt{cm}^{-1}$ (red, solid line) and the mirror counterpart with $\omega_\tau = 0$ $\mathtt{cm}^{-1}$, $\omega_t = 940$ $\mathtt{cm}^{-1}$ (blue, dashed line).

are observed. Although present in the system dynamics, the coherence-transfer effect is not reflected in the evolution of the corresponding CPs for the considered model. This finding questions the interpretation of a multiple-frequencies oscillative evolution of CPs as a signature of coherence transfer, given, e.g., in Ref. [35] for the FMO complex. Furthermore, this observation, together with the above analysis, suggests that 2D PE spectroscopy does not, in general, provide direct information on the system coherences. The signals depend strongly on the transition dipoles between the system eigenstates, and, as system energy levels become increasingly complex, a correct interpretation may become very tedious.

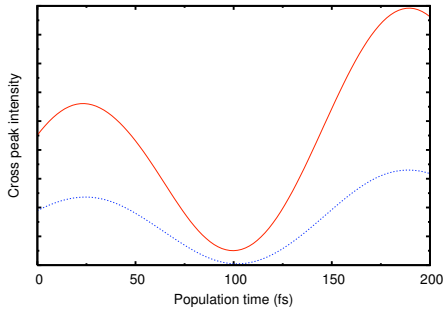

Figure 5.8: The amplitude of a crosspeak of the 2D PE profile corresponding to $\Delta = 1.0$ as a function of population time, $\omega_\tau \approx 185$ $\mathtt{cm}^{-1}$, $\omega_t = 0$ $\mathtt{cm}^{-1}$ (red, solid line) and the mirror counterpart with $\omega_\tau = 0$ $\mathtt{cm}^{-1}$, $\omega_t \approx 185$ $\mathtt{cm}^{-1}$ (blue, dashed line).

Chapter 6

Conclusion

In this work, accurate simulations of 2D photon echo signals applied to a single subunit of the Fenna-Matthews-Olson complex have been performed using the equation-of-motion phase-matching-approach. The system is based on the model of Ref. [38], which has been extended to explicitly consider the evolution of exciton coherences. Realistic pulse durations were considered and pulse-overlap effects were taken into account. The simulations reproduce peak profiles and allow for the study of both diagonal and cross peak oscillations, the latter being visual representations of quantum coherences.

We have thoroughly studied the effects of various dephasing mechanisms on the exciton dynamics, 2D profiles, and oscillations in peak intensity with population time within the Redfield equation model for the FMO complex. We have identified the broadening parameters that result in 2D spectra that are in good agreement with experimental results [35]. The FMO complex is coupled to a bath with a strength of $\eta = 0.2$, while optical dephasing equal to 30 $\mathtt{cm}^{-1}$ was found to be appropriate for reproducing experimental spectral profiles. Using these parameters, the evolution of 2D spectra with population time is adequately

reproduced, apart from the negative contribution due to ESA.

Multiple frequencies in peak oscillations, as detected experimentally, were not observed in these initial simulations. Since the secular approximation has been employed for the description of the system-bath interaction, the phenomenon of coherence transfer through dissipation could not be addressed. The conclusion can be drawn that the fast oscillations of cross peaks observed in experimental data must arise from a more complicated interaction between excitons and bath vibrations than is considered here. Consequently, further developments in the description of the mechanisms underlying energy transfer in the FMO complex are required. A dynamical description beyond the Redfield and Förster theories has been recently proposed [52]. It allows for long-lived coherences, but coherence transfer could not be addressed in the dimer model studied.

Resonance Raman experiments [101–103] have revealed dozens of BChl vibrational modes with frequencies in the range of 88 to 1700 $\mathtt{cm}^{-1}$. These and lower-frequency vibrations have been resolved in a recent fluorescence line-narrowing experiment [104] on the FMO complex of *Cb. tepidum*. The most intense bands lie in the regions near 200, 770, 1200, and 1600 $\mathtt{cm}^{-1}$ and are close to the frequencies obtained by a Fourier transform of the experimental 2D peak oscillations with population time [35]. As has been shown theoretically [44, 64] and experimentally [105], the dynamics of vibrational modes can considerably alter the 2D peak profiles and coherent vibrational motion can contribute to peak intensity oscillations [64]. A study of the effect of damped intramonomer high-frequency vibrational modes on the 2D signals of the FMO complex is a challenging problem.

In order to further probe the dynamics of the FMO system in particular, and of molecular aggregates in general, inclusive of vibrational modes, we have

both extended and simplified our study to a vibronic dimer. The FMO complex lends itself to the modeling by a dimer system, since FMO excitons are primarily created through the interaction of only two BChl molecules. In addition, molecular aggregates form dimer pairs in myriad other biomolecular systems. With this impetus, we have modeled a vibronic dimer after BChl molecules three and four of the FMO complex [22], since these are the primary constituents of excitons one and three, which were extensively studied experimentally [35] and theoretically [46]. Single pulse dynamics of the vibronic dimer are computed and analyzed, with special attention focused on the dimer bilinearly coupled to two harmonic baths through the vibrational modes of the monomers. We have analytically shown that the dimer coupled to baths with fully correlated or fully anticorrelated fluctuations possesses decoherence-free subspaces. The existence of such subspaces is a striking manifestation of quantum interference. Qualitatively similar effects have also been studied in Ref. [106]. For baths with fully correlated fluctuations, an exact master equation for the reduced density matrix of the vibronic dimer was derived in Ref. [55]. No decoherence-free subspaces exist for baths with uncorrelated or partially correlated fluctuations, which ensure relaxation of the entire system towards equilibrium. Similar phenomena have also been demonstrated for the vibrationless dimer within the electronic-bath-coupling model (for further details, see Appendix C of Ref. [55]).

Baths with uncorrelated fluctuations are the default choice in many simulations, although there exists strong experimental evidence that this is not universally the case [92, 93, 95, 107, 108], and baths with partially correlated fluctuations are more appropriate for describing coherent energy and exciton transport [38, 51, 58, 109–121]. We have demonstrated that partially correlated fluctuations give rise to three different relaxation mechanisms with the characteristic rates ν, $\nu_{J_{ab}}$, and ν_γ, where ν characterizes the vibrational relaxation

within each individual monomer, $\nu_{J_{ab}}$ governs the global vibrational relaxation of the dimer as a whole ($\nu_{J_{ab}} = 0$ if $J_{ab} = 0$), and ν_γ describes the vibrational relaxation in those subspaces, which are decoherence-free for fully correlated or uncorrelated fluctuations ($\nu_\gamma = 0$ if $\gamma = \pm 1$). The existence of slow vibrational relaxation channels (ν_γ , $\nu_{J_{ab}} < \nu$) manifests itself in slow decays of the populations and coherences of the dimer density matrix. This observation may contribute to the understanding of the observed long-lived coherences in dimers [89, 90] and more complex excitonic systems. [35, 65, 91–95, 97]

Finally, simulations of 2D PE signals for a vibronic dimer coupled to an uncorrelated harmonic bath were performed. Short Gaussian pulses of 30 fs duration have been employed in the calculations. Optical excitation leads, on the one hand, to a manifestation of the inter-monomer dipole-dipole interaction in the system dynamics and, on the other hand, initiates coherent vibrational motion in excited states of the dimer. The mixing of electronic and vibrational degrees of freedom creates a vibronic manifold, which can be probed by 2D PE spectroscopy. Since ESA was not taken into account (although we believe that the striking dependence of the 2D profiles on the displacement between the equilibrium geometries of the optically coupled electronic case will remain when ESA is included), we concentrated our attention on those vibronic effects on the CP dynamics, which arise due to multilevel vibrational structure in the electronic ground state. The oscillatory behavior of CPs using analytical response-function results for a simplified dephasing- and dissipation-free case have been thoroughly analyzed. Only the rephasing contribution has been calculated, and the employed response-function analysis has involved only the rephasing pathways.

It has been shown that only one contribution to the oscillatory behavior of the CP intensities of a vibronic dimer has the frequency $|\omega_\tau - \omega_t| = |\omega_{ee'}|$ charac-

terisitic for the system excited-state coherence $\rho_{ee'}$ between the two levels with energies E_e and $E_{e'}$. For the most intense transitions (those with the largest μ_{e0}), this contribution is likely to dominate and will lead to single-frequency CP dynamics with population time. Another source of single-frequency dynamics is specific for those CPs for which $\omega_\tau - \omega_t$ is positive and matches a transition frequency between the initial ground state and one of the excited vibrational levels of the ground-state manifold, ω_{g0}. If a similar transition frequency exists between the levels of the excited-state manifold, the two contributions are nearly indistinguishable. A mechanism that leads to multiple frequencies in CP oscillations is a superposition of oscillations with excited-state ($\omega_{ee'}$) and ground-state (ω_{g0}) characteristic frequencies. These contributions due to higher-lying levels become more pronounced if the corresponding dipole transition strengths become significant. Therefore, the probability of finding multiple-frequency oscillations in CP dynamics is larger for the CPs for which ω_t corresponds to relatively weak transitions. Linear-absorption profiles can provide useful hints in this respect. Another interesting observation is that CPs above and below the diagonal can show different frequencies if several oscillatory contributions are resolved. We believe that a Fourier analysis of the CP oscillatory behavoir, combined with information on ground-state vibrational frequencies, will prove very helpful for the interpretation of vibronic effects in 2D PE spectroscopy of complex systems.

The excited state coordinate displacement of the dimer determines the dipole strengths of the transitions between the levels of the electronic ground and excited-state manifolds. We have shown how larger values of the displacement complicate the 2D PE signals and interpretation of the CP oscillatory dynamics. This effect is due to the fact that for larger displacement values more transitions with non-negligible dipoles are involved.

Although included in the calculations, dissipative effects were not the focus of the 2D PE crosspeak analysis for the dimer system under study. The effect of coherence transfer was briefly addressed and it was shown that it is not detected by 2D PE spectroscopy in the present model. The presented analysis is general for any vibronic system and will remain valid for 2D PE spectroscopy of conical intersections, for example, with the exception of the equidistant vibrational ladder specific for the dimer model considered here.

Appendix A

Mathematical Calculations

A.1 The Four-step Runge-Kutta Method

The equation of motion to be modeled in (2.30) is simply a first-order differential equation of the form:

$$\frac{dy(x)}{dx} = f(t, y). \tag{A.1}$$

Given the initial values of t_0 and y_0 (e.g. $t_0 = 0$ and $\rho_{ij}(t_0) = 0$, except for the case $i = j = 1$, for which $\rho_{ij}(t_0) = 1$), subsequent values for the function, $f(t, y)$ can be computed. The Runge-Kutta numerical analysis methods are commonly employed techniques for solving initial value problems for ODEs. These methods are well described in Ref. [122] and subsequent editions, as well as in other numerical analysis texts. The four-step Runge-Kutta method (RK4) is used in this work, and is defined by the equations:

$$\begin{aligned} y_{n+1} &= y_n + \frac{1}{6}k_1 + \frac{1}{3}k_2 + \frac{1}{3}k_3 + \frac{1}{6}k_4 + O(h^5) \\ t_{n+1} &= t_n + h, \end{aligned} \tag{A.2}$$

where y_{n+1} is the RK4 approximation of $y(t_{n+1})$, h is the temporal step size, and

$$\begin{aligned} k_1 &= hf(t_n, y_n) \\ k_2 &= hf(t_n + \frac{1}{2}h, y_n + \frac{1}{2}k_1) \\ k_3 &= hf(t_n + \frac{1}{2}h, y_n + \frac{1}{2}k_2) \\ k_4 &= hf(t_n + h, y_n + k_3). \end{aligned} \tag{A.3}$$

A.2 Franck-Condon Overlap Integrals

Franck-Condon overlap integrals are calculated using an expression derived in Ref. [123], which is briefly summarized here. The wavefunction of a harmonic oscillator is ($\hbar \neq 1$)

$$|\nu\rangle = N_\nu H_\nu(\sqrt{\alpha}x) \exp\left(-\frac{1}{2}\alpha x^2 \right), \tag{A.4}$$

where the normalization factor is given by

$$N_\nu = \left(\frac{\sqrt{\alpha}}{2^\nu \nu! \sqrt{\pi}} \right)^{\frac{1}{2}}, \tag{A.5}$$

$H_\nu(x)$ is the Hermite polynomial, x is the normal coordinate, $\alpha = \omega/\hbar$ and ω is the angular frequency of the oscillator. A second oscillator displaced by an amount d from the first (i.e. $x' = x+d$) likewise is described by the wavefunction

$$|\nu'\rangle = N_{\nu'} H_{\nu'}(\sqrt{\alpha'}x') \exp\left(-\frac{1}{2}\alpha' x'^2 \right). \tag{A.6}$$

Defining $K = (k + k')/2$,

$$S = \frac{\alpha\alpha' d^2}{\alpha + \alpha'}, \tag{A.7}$$

and

$$A = \frac{2\sqrt{\alpha\alpha'}}{\alpha + \alpha'}, \tag{A.8}$$

the overlap of the vibrational states $|\nu\rangle$ and $|\nu'\rangle$ is

$$\begin{aligned} \langle\nu|\nu'\rangle &= \left(\frac{Ae^{-S}}{2^{\nu+\nu'}\nu!\nu'!}\right)^{\frac{1}{2}} \sum_{k=0}^{\nu}\sum_{k'=0}^{\nu'} \left(\begin{array}{c}\nu\\ k\end{array}\right)\left(\begin{array}{c}\nu'\\ k'\end{array}\right) H_{\nu-k}(b)H_{\nu'-k'}(b') \\ &\quad \times(2\sqrt{\alpha})^k(2\sqrt{\alpha'})^{k'} I(K), \end{aligned} \tag{A.9}$$

where $I(K) = 0$ if $k + k'$ is odd, and

$$I(K) = \frac{(2K-1)!!}{(\alpha+\alpha')^K} \tag{A.10}$$

for $k + k'$ even. Note that the following mathematical notation has been used:

$$\left(\begin{array}{c}\nu\\ k\end{array}\right) = \frac{\nu!}{k!(\nu-k)!} \tag{A.11}$$

and

$$(2n-1)!! = 1 \times 3 \times 5 \times \cdots \times (2n-1). \tag{A.12}$$

Bibliography

[1] Łakomy, K., R. Nath, and L. Santos. "Soliton molecules in dipolar bose-einstein condensates". Phys. Rev. A **86**, 1, 013610 (2012).

[2] Gertjerenken, B. and C. Weiss. "Nonlocal quantum superpositions of bright matter-wave solitons and dimers". Journal of Physics B: Atomic, Molecular, and Optical Physics **45**, 16, 165301 (2012).

[3] Reinaudi, G., C. B. Osborn, M. McDonald, S. Kotochigova, and T. Zelevinsky. "Optical Production of Stable Ultracold $^{88}sr_2$ Molecules". Phys. Rev. Lett. **109**, 11, 115303 (2012).

[4] Zhang, Y., W. Ong, I. Arakelyan, and J. E. Thomas. "Polaron-to-Polaron Transitions in the Radio-Frequency Spectrum of a Quasi-Two-Dimensional Fermi Gas". Phys. Rev. Lett. **108**, 23, 235302 (2012).

[5] Salasnich, L. and F. Toigo. "Pair condensation in the BCS-BEC crossover of ultracold atoms loaded onto a two-dimensional square lattice". Phys. Rev. A **86**, 2, 023619 (2012).

[6] Yavari, H., E. Afsaneh, and S. Mirzai. "Josephson effect in superfluid atomic fermi gases at finite temperature". Solid State Sciences **14**, 8, 1244 (2012).

[7] Kasha, M., H. R. Rawls, and A. M. El-Bayoumi. "The exciton model in molecular spectroscopy". Pure and Applied Chemistry **11**, 3–4, 371 (1965).

[8] Kühn, O., T. Renger, and V. May. "Theory of exciton-vibrational dynamics in molecular dimers". Chemical Physics **204**, 99 (1996).

[9] Gelin, M. F., A. V. Pisliakov, and W. Domcke. "Time- and frequency-gated spontaneous emission as a tool for studying vibrational dynamics in the excited state". Phys. Rev. A **65**, 6, 062507 (2002).

[10] Fulton, R. and M. Gouterman. "Vibronic Coupling. II. Spectra of Dimers". The Journal of Chemical Physica **41**, 8, 2280 (1964).

[11] Sadlej, A. "Vibronic absorption spectrum of the ethylene dimer". International Journal of Quantum Chemistry **3**, 5, 569 (1969).

[12] Eisfeld, A., L. Braun, W. Strunz, J. Briggs, J. Beck, and V. Engel. "Vibronic energies and spectra of molecular dimers". The Journal of Chemical Physics **122**, 134103 (2005).

[13] Kjellberg, P., B. Brüggemann, and T. Pullerits. "Two-dimensional electronic spectroscopy of an excitonically coupled dimer". Physical Review B **74**, 2, 24303 (2006).

[14] Förster, T. "Intramolecular energy transference and flourescence". Ann. Physik **2**, 75, 55 (1948).

[15] Dexter, D. L. "A THeory of Sensitized Luminescence in Solids". J. Chem Phys. **21**, 5, 836 (1953).

[16] Blankenship, R. *Molecular Mechanisms of Photosynthesis*. Blackwell Publishing (2002).

[17] Renger, T., V. May, and O. Kühn. "Ultrafast excitation energy transfer dynamics in photosynthetic pigment-protein complexes". Phys. Rep. **343**, 137 (2001).

[18] van Amerongen, H., L. Valkunas, and R. Van Grondelle. *Photosynthetic Excitons*. World Scientific (2000).

[19] McDermott, G., S. M. Prince, A. A. Freer, A. M. Hawthornthwaite-Lawless, M. Z. Papiz, R. J. Cogdll, and N. W. Isaacs. "Crystal-structure of an integral membrane light-harvesting complex from photosynthetic bacteria". Nature **374**, 517 (1995).

[20] Koepke, J., C. Hu, X. und Muenke, K. Schulten, and H. Michel. "The crystal structure of the light-harvesting complex II (B800-850) from Rhodospirillum molischianum". Structure **4**, 581 (1996).

[21] Kühlbrandt, W., D. N. Wang, and Y. Fujiyoshi. "Atomic model of plant light-harvesting complex by electron crystallography". Nature **367**, 614 (1994).

[22] Fenna, R. and B. Matthews. "Chlorophyll arrangement in a bacteriochlorophyll protein from Chlorobium limicola". Nature **258**, 5536, 573 (1975).

[23] Johnson, S. G. and G. J. Small. "Spectral hole burning of a strongly exciton-coupled Bacteriochlorophyll-a antenna complex". Chem. Phys. Lett. **155**, 371 (1989).

[24] Johnson, S. G. and G. J. Small. "Excited-state structure and energy-transfer dynamics of the Bacteriochlorophyll-a antenna complex from Prosthecochloris-aestuarii". J. Phys. Chem. **95**, 471 (1991).

[25] Franken, E. M., S. Neerken, R. J. W. Louwe, J. Amesz, and T. J. Aartsma. "A permanent hole burning study of the FMO antenna complex of the green sulfur bacterium Prosthecochloris aestuarii". Biochemistry **37**, 5046 (1998).

[26] Savikhin, S. and W. S. Struve. "Ultrafast energy-transfer in FMO trimers from the green bacterium Chlorobium-tepidum". Biochemistry **33**, 11200 (1994).

[27] Savikhin, S. and W. S. Struve. "Low-temperature energy transfer in FMO trimers from the green photosynthetic bacterium Chlorobium tepidum". Photosynthesis Res. **48**, 271 (1996).

[28] Gulbinas, V., L. Valkunas, D. Kuciauskas, E. Katilius, V. Liuolia, W. Zhou, and R. E. Blankenship. "Singlet-singlet annihilation and local heating in FMO complexes". J. Phys. Chem. **100**, 17950 (1996).

[29] Freiberg, A., S. Lin, K. Timpmann, and R. E. Blankenship. "Exciton dynamics in FMO bacteriochlorophyll protein at low temperatures". J. Phys. Chem. B **101**, 7211 (1997).

[30] Vulto, S. I. E., A. M. Streltsov, and T. J. Aartsma. "Excited state energy relaxation in the FMO complexes of the green bacterium Prosthecochloris aestuarii at low temperatures". J. Phys. Chem. B **101**, 4845 (1997).

[31] Vulto, S., S. Neerken, R. Louwe, M. de Baat, J. Amesz, and T. Aartsma. "Excited-state structure and dynamics in FMO antenna complexes from photosynthetic green sulfur bacteria". J. Phys. Chem. B **102**, 10630 (1998).

[32] Savikhin, S., D. R. Buck, and W. S. Struve. "Toward level-to-level energy transfers in photosynthesis: The Fenna-Matthews-Olson protein". J. Phys. Chem. B **102**, 5556 (1998).

[33] Louwe, R. J. W. and T. J. Aartsma. "On the nature of energy transfer at low temperatures in the BChl a pigment-protein complex of green sulfur bacteria". J. Phys. Chem. B **101**, 7221 (1997).

[34] Brixner, T., J. Stenger, H. M. Vaswani, M. Cho, and R. E. Blankenship. "Two-dimensional spectroscopy of electronic couplings in photosynthesis". Nature **434**, 625 (2005).

[35] Engel, G. S., T. R. Calhoun, E. L. Read, T. Ahn, T. Mančal, Y. Cheng, R. E. Blankenship, and G. R. Fleming. "Evidence for wavelike energy transfer through quantum coherence in photosynthetic systems". Nature **446**, 782 (2007).

[36] Renger, T. and V. May. "Ultrafast exciton motion in photosynthetic antenna systems: The FMO-complex". J. Phys. Chem. A **102**, 4381 (1998).

[37] Vulto, S., M. de Baat, S. Neerken, F. Nowak, H. van Amerongen, J. Amesz, and T. Aartsma. "Excited state dynamics in FMO antenna complexes from photosynthetic green sulfur bacteria: a kinetic model". J. Phys. Chem. B **103**, 38, 8153 (1999).

[38] Cho, M., H. M. Vaswani, T. Brixner, J. Stenger, and G. R. Fleming. "Exciton analysis in 2d electronic spectroscopy". J. Phys. Chem. B **109**, 10542 (2005).

[39] Cheng, Y.-C., G. S. Engel, and G. R. Fleming. "Elucidation of population and coherence dynamics using cross-peaks in two-dimensional electronic spectroscopy". Chem. Phys. **341**, 285 (2007).

[40] Cheng, Y.-C. and G. R. Fleming. "Coherence quantum beats in two-dimensional electronic spectroscopy". J. Phys. Chem. A **112**, 4254 (2008).

[41] Abramavicius, D., D. V. Voronine, and S. Mukamel. "Unravelling coherent dynamics and energy dissipation in photosynthetic complexes by 2d spectroscopy". Biophys. J. **94**, 3613 (2008).

[42] Voronine, D., D. Abramavicius, and S. Mukamel. "Chirality-based signatures of local protein environments in two-dimensional optical spectroscopy of two species photosynthetic complexes of green sulfur bacteria: Simulation study". Biophys. J. **95**, 4896 (2008).

[43] Gelin, M. F., D. Egorova, and W. Domcke. "Efficient method for the calculation of time- and frequency-resolved four-wave mixing signals and its application to photon-echo spectroscopy". J. Chem. Phys. **123**, 164112 (2005).

[44] Egorova, D., M. F. Gelin, and W. Domcke. "Analysis of cross peaks in two-dimensional electronic photon-echo spectroscopy for simple models with vibrations and dissipation". J. Chem. Phys. **126**, 074314 (2007).

[45] Gelin, M. F., D. Egorova, and W. Domcke. "Efficient calculation of time- and frequency-resolved four-wave-mixing signals". Acc. Chem. Res. **42**, 1290 (2009).

[46] Sharp, L. Z., D. Egorova, and W. Domcke. "Efficient and accurate simulations of two-dimensional electronic photon-echo signals: Illustration for a simple model of the fenna-matthews-olson complex". Journal of Chemical Physics **132**, 014501 (2010).

[47] Ishizaki, A. and G. R. Fleming. "On the adequacy of the redfield equation and related approaches to the study of quantum dynamics in electronic energy transfer". J. Chem. Phys. **130**, 234110 (2009).

[48] May, V. and O. Kühn. *Charge and Energy Transfer Dynamics in Molecular Systems*. Wiley-VCH, Berlin (2000).

[49] Blum, K. *Density Matrix Theory and Applications*. Plenum Press, New York and London (1981).

[50] Vulto, S. I. E., M. A. de Baat, R. J. W. Louwe, H. P. Permentier, T. Neef, M. Miller, H. van Amerongen, and T. J. Aartsma. "Exciton simulations of optical spectra of the FMO complex from the green sulfur bacterium *chlorobium tepidum* at 6 k". J. Phys. Chem. B **102**, 9577 (1998).

[51] Adolphs, J. and T. Renger. "How proteins trigger excitation energy transfer in the FMO complex of green sulfur bacteria". Biophys. J. **91**, 2778 (2006).

[52] Ishizaki, A. and G. R. Fleming. "Unified treatment of quantum coherent and incoherent hopping dynamics in electronic energy transfer: Reduced hierarchy equation approach". J. Chem. Phys. **130**, 234111 (2009).

[53] Weiss, U. *Quantum Dissipative Systems*, vol. 10 of *Series in Modern Condensed Matter Physics*. World Scientific, Singapore (1999).

[54] Redfield, A. G. "The theory of relaxation processes". Adv. Magn. Reson. **1**, 1 (1965).

[55] Gelin, M. F., L. Z. Sharp, D. Egorova, and W. Domcke. "Bath-induced correlations and relaxation of vibronic dimers". J. Chem. Phys. **136**, 034507 (2012).

[56] Lidar, D. A., I. L. Chuang, and K. B. Whaley. "Decoherence-free subspaces for quantum computation". Phys. Rev. Lett. **81**, 2594 (1998).

[57] Gelin, M. F. and D. S. Kosov. "Molecular reorientation in hydrogen-bonding liquids". J. Chem Phys. **124**, 144514 (2006).

[58] Ishizaki, A. and G. R. Fleming. "Quantum superpositions in photosynthetic light harvesting: delocalization and entanglement". New J. Phys. **12**, 055004 (2010).

[59] Pisliakov, A. V., T. Mančal, and G. R. Fleming. "Two-dimensional optical three-pulse photon echo spectroscopy. II. Signatures of coherent electronic motion and exciton population transfer in dimer two-dimensional spectra". J. Chem. Phys. **124**, 234505 (2006).

[60] Yuen-Zhou, J. and A. Aspuru-Guzik. "Quantum process tomography of excitonic dimers from two-dimensional electronic spectroscopy. i. general theory and application to homodimers". J. Chem. Phys. **134**, 134505 (2011).

[61] Mukamel, S. *Principles of nonlinear optical spectroscopy*. Oxford University Press, USA (1995).

[62] Mančal, T., A. Pisliakov, and G. Fleming. "Two-dimensional optical three-pulse photon echo spectroscopy. I. Nonperturbative approach to the calculation of spectra". J. Chem. Phys. **124**, 234504 (2006).

[63] Müh, F., M. E.-A. Madjet, J. Adolphs, A. Abdurahman, B. Rabenstein, H. Ishikita, E.-W. Knapp, and T. Renger. "alpha-Helices direct excitation energy flow in the Fenna-Matthews-Olson protein". Proc. Natl. Acad. Sci. USA **104**, 16862 (2007).

[64] Egorova, D. "Detection of electronic and vibrational coherences in molecular systems by 2D electronic photon echo spectroscopy". Chem. Phys. **347**, 166 (2008).

[65] Panitchayangkoon, G., D. Hayes, K. A. Fransted, J. R. Caram, E. Harel, J. Wen, R. E. Blankenship, and G. S. Engel. *Long-lived quantum coherence in photosynthetic complexes at physiological temperature*, vol. 107. PNAS (2010).

[66] Rebentrost, P., M. Mohseni, and A. Aspuru-Guzik. "Role of quantum coherence and environmental fluctuations in chromophoric energy transport". J. Phys. Chem. B **113**, 9942 (2009).

[67] Abramavicius, D. and S. Mukamel. "Many-body approaches for simulating coherent nonlinear spectrosopies of electronic and vibrational excitons". Chem. Rev. **104**, 4, 2073 (2004).

[68] Renger, T., V. May, and O. Kühn. "Ultrafast excitation energy transfer dynamics in photosynthetic pigment-protein complexes". Physics Reports **343**, 137 (2001).

[69] Garg, A., J. N. Onuchic, and V. Ambegaokar. "Effect of friction on electron transfer in biomolecules". J. Chem. Phys. **83**, 9, 4491 (1985).

[70] Chernyak, V. and S. Mukamel. "Collective coordinates for nuclear spectral densities in energy transfer and femtosecond spectroscopy of molecular aggregates". J. Chem Phys. **105**, 11, 4565 (1996).

[71] Thoss, M., H. Wang, and W. H. Miller. "Self-consistent hybrid approach for complex systems: Application to the spin-boson model with debye spectral density". J. Chem. Phys. **115**, 7, 2991 (1996).

[72] Hughes, K. H., C. D. Christ, and I. Burghardt. "Effective-mode representation of non-markovian dynamics: A hierarchical approximation of the spectral density. i. application to single surface dynamics". J. Chem. Phys. **131**, 2, 024109 (2009).

[73] Smith, E. R., D. A. Farrow, and D. M. Jonas. "Response functions for dimers and square-symmetric molecules in four-wave-mixing experiments with polarized light". J. Chem. Phys. **123**, 4, 044102 (2005).

[74] Tanimura, Y. and S. Mukamel. "Femtosecond pump-probe spectroscopy of intermolecular vibrations in molecular dimers". J. Chem. Phys. **103**, 5, 1981 (1995).

[75] Wagner, M. "Generalised fulton-gouterman transformation for systems of abelian symmetry". J. Phys. A: Math. Gen. **17**, 11, 2319 (1984).

[76] Kimura, A. and T. Kakitani. "Advanced theory of excitation energy transfer in dimers". J. Phys. Chem. A **111**, 47, 12042 (2007).

[77] Hossein-Nejad, H. and G. D. Scholes. "Energy transfer, entanglement and decoherence in a molecular dimer interacting with a phonon bath". New J. Phys. **12**, 065045 (2010).

[78] Nazir, A. "Correlation-dependent coherent to incoherent transitions in resonant energy transfer dynamics". Phys. Rev. Lett. **103**, 14, 146404 (2009).

[79] Matro, A. and J. A. Cina. "Theoretical study of time-resolved fluorescence anisotropy from coupled choromophore pairs". J. Phys. Chem. **99**, 9, 2568 (1995).

[80] Renger, T., J. Voigt, V. May, and O. Kühn. "Dissipative motion in a chlorophyll *a/b* dimer of the light harvesting complex of photosystem II: Simulation of pump-probe spectra". Journal of Physical Chemistry **100**, 15654 (1996).

[81] Kishi, R., M. Nakano, T. Minami, H. Fukui, H. Nagai, K. Yoneda, and H. Takahashi. "Theoretical study on exciton recurrence motion in anthracene dimer using the ab initio mo-ci based quantum master equation approach". J. Phys. Chem. A **113**, 18, 5455 (2009).

[82] Roden, J., W. T. Strunz, and A. Eisfeld. "Non-markovian quantum state diffusion for absorption spectra of molecular aggregates". J. Chem. Phys. **134**, 3, 034902 (2011).

[83] Kilin, D. S., O. V. Prezhdo, and M. Schreiber. "Photoinduced vibrational coherence transfer in molecular dimers". J. Phys. Chem. A **111**, 41, 10212 (2007).

[84] Cina, J. and G. Fleming. "Vibrational Coherence Transfer and Trapping as Sources for Long-Lived Quantum Beats in Polarized Emission from Energy Transfer Complexes". Journal of Physical Chemistry A **108**, 51, 11196 (2004).

[85] Seibt, J., K. Renziehausen, D. V. Voronine, and V. Engel. "Probing the geometry dependence of molecular dimers with two-dimensional vibronic spectroscopy". J. Chem. Phys. **130**, 13, 134318 (2009).

[86] Abramavicius, D., L. Valkunas, and S. Mukamel. "Transport and correlated fluctuations in the nonlinear optical response of excitons". EPL **80**, 1, 17005 (2007).

[87] Cho, M. "Coherent two-dimensional optical spectroscopy". Chem. Rev. **108**, 4, 1131 (2008).

[88] Nemeth, A., V. Lukés, J. Sperling, F. Milota, H. F. Kauffmann, and T. Mančal. "Two-dimensional electronic spectra of an aggregating dye: simultaneous measurement of monomeric and dimeric line-shapes". PCCP **11**, 5986 (2009).

[89] Bittner, T., K.-D. Irrgang, G. Renger, and M. R. Wasielewski. "Ultrafast excitation energy transfer and exciton-exciton annihilation processes in isolated light harvesting complexes of photosystem II (LHC II) from spinach". Journal of Physical Chemistry **98**, 11821 (1994).

[90] Yamazaki, I., N. Aratani, S. Akimoto, T. Yamazaki, and A. Osuka. "Observation of quantum coherence for recurrence motion of exciton in anthracene dimers in solution". Journal of American Chemical Society **125**, 24, 7192 (2003).

[91] Savikhin, S., D. Buck, and W. Struve. "Oscillating anisotropies in a bacteriochlorophyll protein: Evidence for quantum beating between exciton levels". Chemical Physics **223**, 2-3, 303 (1997).

[92] Womick, J. M. and A. M. Moran. "Exciton coherence and energy transport in the light-harvesting dimers of allophycocyanin". Journal of Physical Chemistry B **113**, 15747 (2009).

[93] Lee, H., Y. Cheng, and G. Fleming. "Coherence Dynamics in Photosynthesis: Protein Protection of Excitonic Coherence". Science **316**, 5830, 1462 (2007).

[94] Milota, F., J. Sperling, A. Nemeth, and H. F. Kauffmann. "Two-dimensional electronic photon echoes of a double band j-aggregate: Quantum oscillatory motion versus exciton relaxation". Chemical Physics **357**, 1–3, 45 (2009).

[95] Collini, E. and G. D. Scholes. "Coherent intrachain energy migration in a conjugated polymer at room temperature". Science **323**, 369 (2009).

[96] Panitchayangkoon, G., D. Hayes, K. A. Fransted, J. R. Caram, E. Harel, J. Wen, R. E. Blankenship, and G. S. Engel. "Long-lived quantum coherence in photosynthetic complexes at physiological temperature" .

[97] Collini, E., C. Y. Wong, K. E. Wilk, P. M. G. Curmi, P. Brumer, and G. D. Scholes. "Coherently wired light-harvesting in photosynthetic marine algae at ambient temperature". Nature **463**, 644 (2010).

[98] Stock, G. and W. Domcke. "Model studies on the time-resolved measurement of excited-state vibrational dynamics and vibronic coupling". Chemical physics **124**, 2, 227 (1988).

[99] Egorova, D., M. Thoss, W. Domcke, and H. Wang. "Modeling of ultrafast electron-transfer processes: Validity of multilevel redfield theory". Journal of Chemical Physics **119**, 5 (2003).

[100] Egorova, D., M. F. Gelin, and W. Domcke. "Time- and frequency-resolved fluorescence spectra of nonadiabatic dissipative systems: What photons can tell us". Journal of Chemical Physics **122**, 134504 (2005).

[101] Lutz, M., A. J. Hoff, and L. Brehamet. Biochimica et Biophysica Acta **679**, 331 (1981).

[102] Diers, J. R. and D. F. Bocian. "Qy-excitation resonance raman spectra of bacteriochlorophyll observed under fluorescence-free conditions. implications for cofactor structure in photosynthetic proteins". Journal of American Chemical Society **117**, 6629 (1995).

[103] Zazubovich, V., I. Tibe, and G. J. Small. "Bacteriochlorophyll *a* franck-condon factors for the s0 -¿ s1(qy) transition". Journal of Physical Chemistry B **105**, 12410 (2001).

[104] Rätsep, M. and A. Freiberg. "Electron-phonon and vibronic couplings in the fmo bacteriochlorophyll *a* antenna complex studied by difference fluorescence line narrowing". Journal of Luminesence **127**, 251 (2007).

[105] Nemeth, A., F. Milota, T. Mančal, V. Lukeš, and H. F. Kauffmann. "Vibronic modulation of lineshapes in two-dimensional electronic spectra". Chemical Physics Letters **459**, 94 (2008).

[106] Caruso, F., A. W. Chin, A. Datta, S. F. Huelga, and M. B. Plenio. "Highly efficient energy excitation transfer in light-harvesting complexes: The fundamental role of noise assisted transport". Journal of Chemical Physics **131**, 105106 (2009).

[107] Demirdöven, N., M. Khalil, and A. Tokmakoff. "Correlated Vibrational Dynamics Revealed by Two-Dimensional Infrared Spectroscopy". Physical Review Letters **89**, 23, 237401 (2002).

[108] Wolynes, P. G. "Some quantum weirdness in physiology". PNAS **106**, 41, 17247 (2009).

[109] Renger, T. and R. A. Marcus. "On the relation of protein dynamics and exciton relaxation in pigment-protein complexes: An estimation of the spectral density and a theory for the calculation of optical spectra". Journal of Chemical Physics **116**, 22, 9997 (2002).

[110] Nalbach, P., J. Eckel, and M. Thorwart. "Quantum coherent nioolecular energy transfer with spatially correlated fluctuations". New Journal of Physics **12**, 065043 (2010).

[111] Caruso, F., A. W. Chin, A. Datta, S. F. Huelga, and M. B. Plenio. "Entanglement and entangling power of the dynamics in light-harvesting complexes". Physical Review A **81**, 6, 062346 (2010).

[112] Olbrich, C., J. Strümpfer, K. Schulten, and U. Kleinekathöfer. "Quest for spatially correlated fluctuations in the FMO light-harvesting complex". Journal of Physical Chemistry B **115**, 4, 758 (2011).

[113] Strümpfer, J. and K. Schulten. "The effect of correlated bath fluctuations on exciton transfer". Journal of Chemical Physics **134**, 9, 095102 (2011).

[114] Abramavicius, D. and S. Mukamel. "Quantum oscillatory exciton migration in photosynthetic reaction centers". Journal of Chemical Physics **133**, 6, 064510 (2010).

[115] Ishizaki, A. and Y. Tanimura. "Dynamics of a multimode system coupled to multiple heat baths probed by two-dimensional infrared spectroscopy". Journal of Physical Chemistry A **111**, 38, 9269 (2007).

[116] Perdomo, A., L. Vogt, A. Najmaie, and A. Aspuru-Guzik. "Engineering directed excitonic energy transfer". Applied Physics Letters **96**, 9, 093114 (2010).

[117] Fassioli, F., A. Nazir, and A. Olaya-Castro. "Quantum state tuning of energy transfer in a correlated environment". Journal of Physical Chemistry Letters **1**, 14, 2139 (2010).

[118] Cheng, Y. and K. B. Whaley. "Environmental correlation effects on excitation energy transfer in photosynthetic light harvesting". Physical Review E **83**, 1, 011906 (2011).

[119] Yu, Z. G., M. A. Berding, and H. Wang. "Spatially correlated fluctuations and coherence dynamics in photosynthesis". Physical Review E **78**, 5, 050902(R) (2008).

[120] Venkatramani, R. and S. Mukamel. "Correlated line broadening in multidimensional vibrational spectroscopy". Journal of Chemical Physics **117**, 24, 11089 (2002).

[121] Abramavicius, D. and S. Mukamel. "Exciton dynamics in chromophore aggregates with correlated environment fluctuations". Journal of Chemical Physics **134**, 17, 174504 (2011).

[122] Press, W. A., S. A. Teukolsky, W. T. Vetterling, and B. P. Flannery. *Numerical Recipes in Fortran – The Art of Scientific Computing*. Cambridge University Press, Cambridge, 2nd edn. (1992).

[123] Chang, J. "A new formula to calculate Franck–Condon factors for displaced and distorted harmonic oscillators". Journal of Molecular Spectroscopy **232**, 1, 102 (2005).